`

Catalytic processes for conversion of natural gas engine exhaust and 2,3-butanediol conversion to 1,3-butadiene

by

FAN ZENG

B.S., Wuhan Institute of Technology, 2010
M.S., University of Louisiana at Lafayette, 2011

AN ABSTRACT OF A DISSERTATION

submitted in partial fulfillment of the requirements for the degree

DOCTOR OF PHILOSOPHY

Department of Chemical Engineering
College of Engineering

KANSAS STATE UNIVERSITY
Manhattan, Kansas

2016

`

Abstract

Extensive research has gone into developing and modeling the three-way catalyst (TWC) to reduce the emissions of hydrocarbons, NO_x and CO from gasoline-fueled engines level. However, much less has been done to model the use of the three-way catalyst to treat exhaust from natural gas-fueled engines. Our research address this gap in the literature by developing a detailed surface reaction mechanism for platinum based on elementary-step reactions. A reaction mechanism consisting of 24 species and 115 elementary reactions was constructed from literature values. All reaction parameters were used as found in the literature sources except for steps modified to improve the model fit to the experimental data. The TWC was simulated as a one-dimension, isothermal plug flow reactor (PFR) for the steady state condition and a continuous stirred-tank reactor (CSTR) for the dithering condition. This work describes a method to quantitatively simulate the natural gas engine TWC converter performance, providing a deep understanding of the surface chemistry in the converter.

Due to the depletion of petroleum oil and recent volatility in price, synthesizing value-added chemicals from biomass-derived materials has attracted extensive attention. 1, 3-butadiene (BD), an important intermediate to produce rubber, is conventionally produced from petroleum. Recently, one potential route is to produce BD by dehydration of 2, 3-butanediol (BDO), which is produced at high yield from biomass. This reaction was studied over two commercial forms of alumina. Our results indicate acid/base properties greatly impact the BD selectivity. Trimethylamine can also modify the acid/base properties on alumina surface and affect the BD selectivity. Scandium oxide, acidic oxide or zirconia dual bed systems are also studied and our results show that acidic oxide used as the second bed catalyst can promote the formation of BD, while 2,5-dimethylphenol is found when the zirconia is used as the second bed catalyst which is due to the strong basic sites.

`

Catalytic processes for conversion of natural gas engine exhaust and 2,3-butanediol conversion to 1,3-butadiene

by

FAN ZENG

B.S., Wuhan Institute of Technology, 2010
M.S., University of Louisiana at Lafayette, 2011

A DISSERTATION

submitted in partial fulfillment of the requirements for the degree

DOCTOR OF PHILOSOPHY

Department of Chemical Engineering
College of Engineering

KANSAS STATE UNIVERSITY
Manhattan, Kansas

2016

Approved by:

Major Professor
Keith L. Hohn

`

Copyright

`

Abstract

Extensive research has gone into developing and modeling the three-way catalyst (TWC) to reduce the emissions of hydrocarbons, NO_x and CO from gasoline-fueled engines level. However, much less has been done to model the use of the three-way catalyst to treat exhaust from natural gas-fueled engines. Our research address this gap in the literature by developing a detailed surface reaction mechanism for platinum based on elementary-step reactions. A reaction mechanism consisting of 24 species and 115 elementary reactions was constructed from literature values. All reaction parameters were used as found in the literature sources except for steps modified to improve the model fit to the experimental data. The TWC was simulated as a one-dimension, isothermal plug flow reactor (PFR) for the steady state condition and a continuous stirred-tank reactor (CSTR) for the dithering condition. This work describes a method to quantitatively simulate the natural gas engine TWC converter performance, providing a deep understanding of the surface chemistry in the converter.

Due to the depletion of petroleum oil and recent volatility in price, synthesizing value-added chemicals from biomass-derived materials has attracted extensive attention. 1, 3-butadiene (BD), an important intermediate to produce rubber, is conventionally produced from petroleum. Recently, one potential route is to produce BD by dehydration of 2, 3-butanediol (BDO), which is produced at high yield from biomass. This reaction was studied over two commercial forms of alumina. Our results indicate acid/base properties greatly impact the BD selectivity. Trimethylamine can also modify the acid/base properties on alumina surface and affect the BD selectivity. Scandium oxide, acidic oxide or zirconia dual bed systems are also studied and our results show that acidic oxide used as the second bed catalyst can promote the formation of BD, while 2,5-dimethylphenol is found when the zirconia is used as the second bed catalyst which is due to the strong basic sites.

`

Table of Contents

`

`

`

List of Figures

`

`

`

`

`

List of Tables

`

Acknowledgements

Many people have given me tremendous help and guidance in the work present in this dissertation. First and foremost, I would like to thank my advisor Dr. Keith Hohn who give me this opportunity to pursue my PhD in K-State, I always have easy-going discussions with him and his knowledge, patience and great attitude continuously inspire and motivate me to work out the problems in the research.

I would also like to give a special thanks to all my committee members, Dr. Praveen Vadlani, Dr. James Edgar and Dr. Placidus Amama. I also like to thank Dr. Paul Smith for serving as my outside chair. Thank you all for serving on my committee and for your contributions to the thesis.

I would also like to thank Michael Heidlage for helping me with BET and XRD, John Stanford for the help with the GC-MASS, Balaji Padavala for the instructive discussion of the XRD results. Meanwhile I would like to thank my labmates Xaiojiao Sun, Myles Ikenberry, Quanxing Zheng and Jingxi Xie for their help in the lab. Meanwhile, I would thank undergraduate researcher Damon Guyett, Megan Midkiff and Angelica White for their help in my research. In addition, I would thank Yixing Zhang and Kyle Probst in grain science and industry department for their help in HPLC and GC-MASS.

I also would like to thank Jiayi Xu and Dr. Bin Liu for their tremendous work in DFT calculation to support the BDO reaction mechanism. In addition, I want to thank Dr. William Tenn and Dr. Sudhir Aki for their continuous support in the project of BDO dehydration over alumina. Also, I want to thank Dr. Steffan Bossmann for his help in the discussion of 2,5-dimethylphenol formation mechanism. Meanwhile, I want to thank John Finke and Dr. Daniel Olsen from Colorado State University for sharing the experimental data and their helpful discussions to model the TWC performance with exhaust mixture from natural gas engine.

Finally, I want to thank all my family, thanks for their endless support and care.

`

Dedication

To all the people I have worked with.

`

Chapter 1 - Introduction

Catalysis plays a critical role in a wide variety of industrial processes. By one estimate, catalysis plays a role in the manufacture of 90% of all commercially produced chemical products [1]. Catalysis is important to society both because it can be used to remove harmful pollutants that can adversely affect people's health, but also because it can be used to produce important products that improve people's lives.

This thesis addresses two disparate topics that both fall under the broader field of heterogeneous catalysis. The first topic is the modeling of three-way catalytic converter performance with exhaust mixture from natural gas-fueled engines and the second topic is the dehydration of BDO over various metal oxides and the impact of acid/base properties on product distribution.

1.1. Conversion of natural gas engine exhaust

Air quality is a worldwide issue that has triggered more and more stringent regulation since the first air emissions regulation Clean Air Act (CAA) promulgated in 1970. The exhaust emission from the internal combustion engine is a major air pollution source and the current regulations, such as EPA 10 and EURO VI, increase the need to understand the aftertreatment system.

Natural gas is an important energy source and it is expected to see demand growth of about 65 percent, rising into second place only to oil by 2040 [2]. In the US natural gas transmission industry, stationary internal combustion engine fueled with natural gas is responsible to drive the compressor to pump the natural gas from the producing area to the consumers. In 2007, more than 1200 compressor stations located along the natural gas pipeline to maintain natural gas continuous flow [3]. The exhaust emission control of these natural gas-fueled engine is necessary to meet the EPA 10 regulation.

The exhaust emission from a natural gas engine mainly consists of unburnt hydrocarbons (HC), CO, CO_2, NOx, NH_3, formaldehyde. The exhaust gas reduction process is carried out in the three-way catalytic converter (TWC), named after its ability to simultaneously convert HC, CO and NOx into less harmful gases such as CO_2, H_2O and N_2:

`

$$C_xH_y + \left(x + \frac{y}{4}\right) O_2 \rightarrow xCO_2 + \frac{y}{2} H_2O \quad (1)$$

$$CO + \frac{1}{2} O_2 \rightarrow CO_2 \quad (2)$$

$$2NO_x \rightarrow N_2 + xO_2 \quad (3)$$

A simple engine aftertreatment system is shown in Figure 1-1. Fuel flows into the engine through the fuel injector and fuel combustion occurs in the engine. The exhaust emission out of the engine is converted into less harmful gas in the catalytic converter before being released to the atmosphere. There are two oxygen sensors placed both upstream and downstream of the converter, measuring the oxygen concentration in the exhaust mixture. These sensors send signals to the engine control module (ECM), which will control the fuel injector to keep the fuel combustion near the stoichiometric point in order to reduce the emission of pollutants.

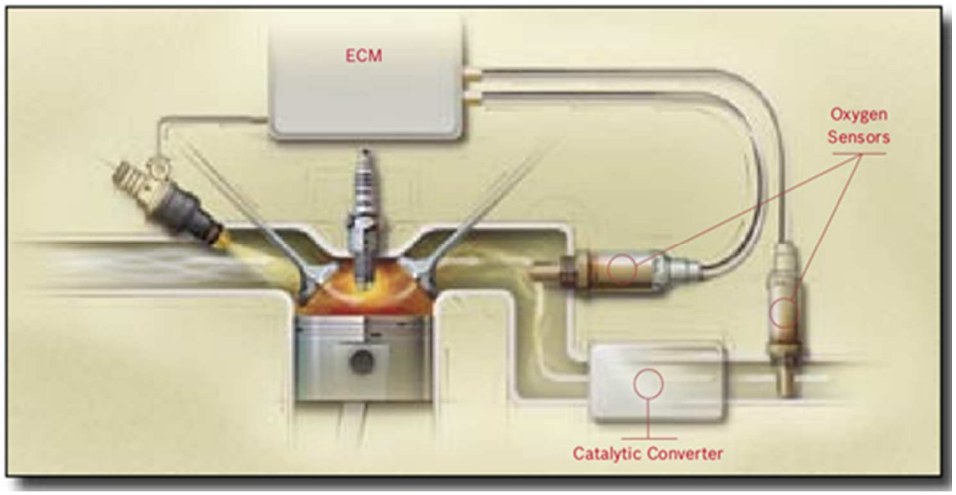

Figure 1-1. Engine aftertreatment system [4].

The common structure of TWC is shown in Figure 1-2. The TWC is widely used for both gasoline and natural gas engines. It typically consists of a metallic or ceramic monolithic substrate with a honeycomb structure that provides a high geometric surface area with a low pressure drop. The monolithic substrate is coated with a high surface-area carrier material such as aluminum oxide (Al_2O_3) called a “washcoat” or “support”, doped with cerium (Ce) as an oxygen storage material. The catalytically active sites are the noble metals, such as platinum, palladium and rhodium, which are doped on the washcoat. Additionally, some stabilizers are used to prevent the thermal ageing process. The exhaust emission gas out of the engine will flow into the monolith channels. Firstly,

`

the gas species adsorb on the catalyst surface, catalytic reactions take place on the surface and then the products desorb from the surface. External and internal mass transfer limitations are also important and will affect the exhaust removal efficiency. Homogeneous reaction in the gas phase are not generally considered to be important.

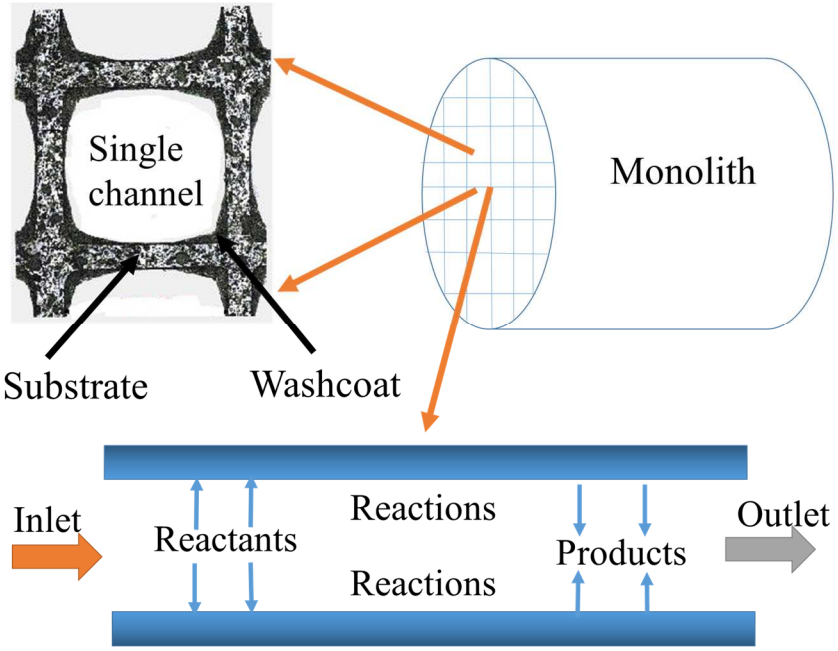

Figure 1-2. Monolith and washcoat in TWC.

The exhaust emission condition is quantized using the normalized air to fuel ratio as

$$\lambda = \frac{AF_{\text{realistic}}}{AF_{\text{stoichiometric}}}$$

Therefore, $\lambda>1$ corresponds to fuel lean conditions (excess O_2 and NOx) while $\lambda<1$ corresponds to fuel rich conditions (excess CO and HC). It is widely accepted that the air fuel ratio has a great impact on the TWC ability to efficiently remove HC, NOx and CO from the exhaust. Fuel lean conditions promote the oxidation of HC and CO, but the NOx reduction is greatly inhibited by the excessive O_2. In the fuel rich condition, NOx conversion is high due to excessive reductant such as HC, CO and H_2, but the HC and CO conversion is inhibited by a lack of oxygen. It is necessary to operate the engine around the stoichiometric condition ($\lambda=1$) to achieve exhaust gas conversions for all three species. Figure 1-3 shows the CH_4, NO and CO conversion as a function of λ in the three

`

way catalyst [5]. It is seen that only within a very narrow λ range 0.985±0.002 can all three components can be reduced significantly.

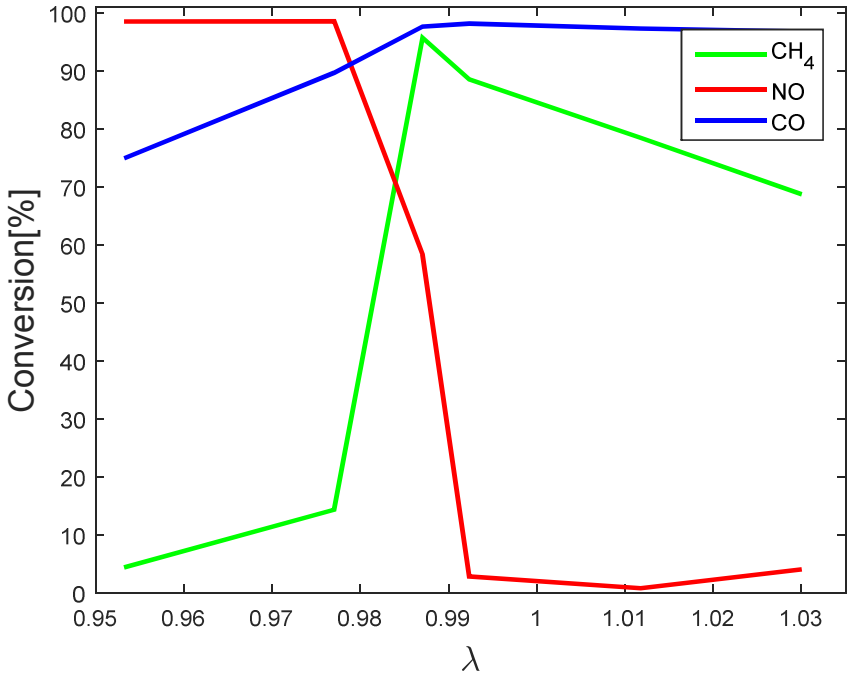

Figure 1-3. Experimental result of CH_4, NO and CO conversion as a function of λ [5].

To control exhaust emissions from natural gas engines, one method is to operate the engine near the stoichiometric point (λ=1) to achieve high conversion of all species. Another method is to operate the engine in a dithering condition, where the air fuel ratio (AFR) is cycled between fuel-rich and fuel-lean conditions. Defoort and coworkers studied the AFR dithering effect on the performance of TWC operating on natural gas-fueled engine and found that the operation window was widened in the dithering condition compared to AFR without dithering [5]. Shi and coworker studied the natural gas engine exhaust gas conversion efficiency in TWC under steady state and dithering conditions. They found an optimal midpoint λ, frequency and amplitude to minimize the exhaust emission, but the reaction chemistry was not well understood [6].

The primary goal of this project is to numerically simulate the TWC performance with the exhaust mixture from a natural gas engine using a comprehensive and thermodynamically consistent elementary-step reaction mechanism. The reaction

`

mechanism consisting of 24 species and 115 elementary reactions and was constructed from literature values. All reaction parameters were used as found in the literature sources except for steps modified to improve the model fit to the experimental data. Plug flow reactor model and tanks-in-series model are used for steady state and dithering modes for operating the natural gas engine. It will be shown that simulations can approximate experimental results reasonably well for a variety of conditions, while providing molecular level information on catalytic chemistry.

1.2. 2,3-butanediol conversion to 1,3-butadiene

1, 3-butadiene (BD) is a colorless gas at room temperature with a characteristic hydrocarbon odor. It is sparingly soluble in water (1 g/L, 20 ^{0}C); soluble in benzene, carbon tetrachloride and diethyl ether. It is a hazardous gas due to its flammability, reactivity and carcinogenicity [7]. It has been widely used in manufacturing polymer products. In the past years, 2, 3-butanediol (BDO) was used as feedstock to make BD for synthetic rubber [8]. However, since the development of petroleum industry, BD is produced directly from heavy oil, such as naphtha. Recently, with the depletion and price volatility of fossil fuel [9], interest has shifted to the synthesis of BD from biomass. Researchers are developing a cost-competitive biological route to BD to ensure ample supply and reduce price volatility of the chemical. Fermentation of biomass-based xylose [10] and glucose by Klebsiella pneumodae yields BDO which can then be converted to BD by catalytic dehydration. However, the BD selectivity is not impressive and undesired methyl ethyl ketone (MEK) is the dominant product due to the keto-enol tautomerization and pinacol rearrangement. Since both acid sites and basic sites can be involved in alcohol dehydration and affect the dehydration orientation, such as the Sayzeff orientation and Hofmann orientation, the objective of this study is to understand how bi-functional catalysts impact in the dehydration of BDO and selectivity of BD, in particular how the acid and base sites on the catalyst can be tuned to increase BD selectivity.

`

1.2.1. Application of 1,3-butadiene

Most BD is used in the production of polymers and chemical intermediates for manufacturing polymer products. These polymers are crucial components of automobile, construction materials appliance parts, computers, telecommunications equipment, clothing protective and clothing. The major end uses for BD are listed in Table 1-1. The largest consumption of BD is in the production of synthetic rubber, such as styrene-butadiene rubber, polybutadiene rubber and other polymers. BD is also used for manufacturing of adiponitrile, which is an intermediate chemical used in the manufacture of nylon 6, 6.

Table 1-1. 1,3-butadiene end uses [11].

BD end use	Percent of world BD demand(9.1 million metric tons in 2004) (%)	Downstream use	Secondary downstream use
Styrene-butadiene-rubber (SBR)	28	Tires	
		Tire products	
		Adhesives	
		Sealants	
		Rubber articles	Shoe soles
Polybutadiene (PB)	26	Tires	
		ABS resins	Computers, printers
		Impact modifiers	Plastics
Styrene-butadiene latex (SBL)	12	Foam rubber	Carpet backing, cushions, pads
		Adhesives	Flooring, tiles, roofing
		Sealants	
Other uses	34		

1.2.2. Production of BD in the petroleum industry

BD is commonly produced through three processes [11]:

1. Steam cracking of paraffinic hydrocarbons
2. Catalytic dehydrogenation of n-butane and n-butene
3. Oxidative dehydrogenation of n-butene

The most important process of the three is steam cracking, since over 95% percent of BD is produced as a by-product of ethylene production via steam cracking. In this process, the feedstocks (ethane, propane, butane, naphtha, condensate or gas oil) are fed

`

to a pyrolysis furnace combined with steam and they react at temperatures between 790 and 830 ^{0}C. Steam cracking produces a wide range of pyrolysis products, like hydrogen, ethylene, propylene, BD and other olefins. The pyrolysate is quenched to separate the heavy components; compressed to remove the C5 and higher components as a raw pyrolysis gasoline, and then dried. The resulting components (C1-C4) are taken through a series of distillation steps to get rid of the hydrogen, methane, ethylene and other light products and leaving the crude BD.

The amounts of crude BD produced in steam cracking are dependent on the composition of feed. Heavier feeds, such as naphtha, yield higher amounts of BD than lighter feeds. A cracker using ethane produces about 2 lb of BD per 100 lb of ethylene, while a naphtha cracker will produce about 16 lb per 100 lb of ethylene. Depending on plant operation and feedstock used, the BD concentration in crude BD varies from 40 to 50%, maximum 75% [11].

The crude BD is purified by an extractive distillation process since the boiling points of the component of crude BD are so close. The typical process involves one or two extractive distillation steps, followed by one or two conventional distillation steps. In the extractive distillation process, the crude BD is fed into a column where it is washed by an extraction solvent. The less soluble components (butane and butene) go out the overhead of the column. The bottom products contain the solvent, BD and other more soluble components. The bottom stream is fed into a solvent stripper to recycle the solvent back to the extraction column. The BD-rich overhead is sent to further distillation to remove the acetylene and other components. The final purified BD is typically>99.5% BD. The BD is then sent to light hydrocarbon storage spheres. Usually a tertiary-butyl catechol (TBC) is added to BD as a stabilizer to prevent undesirable polymerization of BD.

1.2.3. Production of BD from 2, 3-butanediol

Back in 1945, Winfield studied the catalytic dehydration of BDO to BD over thoria [8]. He found that thoria catalyzed the dehydration of the BDO to 3-buten-2-ol (3B2OL) and further to BD under reduced pressure at 350 ^{0}C. With thoria as catalyst, single pass conversions of 60% to BD and 80% to 3B2OL plus BD have been obtained.

`

The rate of dehydration to 3B2OL and BD was inversely proportional to the pressure. It was decided to work at low pressure, not entirely because reduced pressure would favor a reaction in which the number of molecules increases, but because the possibility of poisoning of catalyst by reaction products. The author also mentioned that the difficulty in dehydrating the BDO to BD is readily understood when its structure is considered. The two hydroxyl groups on adjacent carbon atoms, facilitating dehydration to enol form MEK. Two additional reactions in which a molecule of water is removed from the 2- and 3- position may occur, one yield 2-buten oxide and another proceeding to MEK by pinacol rearrangement. In general, the author considered all the possible reaction mechanism and different product distribution as the reason why 3B2OL and BD are successfully produced, but do not predominant except under special conditions.

Extensive studies of BDO dehydration have been reported that focus on producing MEK as an industrial solvent. Liquid phase dehydration of BDO was carried out to produce MEK using a sulfuric acid catalyst [12]. The kinetics of dehydration was first order with respect to BDO and formation of MEK could be described by a pinacol rearrangement. Zhang et al [13] modified HZSM-5 zeolites with boric acid to dehydrate BDO to produce MEK. The results showed that high Si/Al ratio was beneficial to low-temperature activation of BDO and methyl migration to 2-methyl propanal (MPA), leading to a high yield of MEK and high selectivity of MPA. Slight modification with boric acid enhanced the performance of HZSM-5(360). According to the characterization results, the excellent performance over HZSM-5(360) was due to the highest amount of strong acidic sites attributed to H-bonded hydroxyl groups, normally silanols. B-OH and retained silanols were responsible for the promotion of catalytic performance over 1%B/HZSM-5(360). BD selectivity value in this research was about 1% with varying Si/Al ratio, but since the analysis is carried out off-line by a gas chromatograph, the selectivity value is only the amount of BD dissolved in the analyte, not the entire BD produced in the catalytic reaction.

Bourns et al [14] studied the effect of temperature, feed rate and water dilution on the dehydration of BDO over activated bentonite. The finely powdered bentonite was treated with 20% aqueous sulfuric acid of such a volume that the weight of acid was 50% of the weight of the catalyst being activated. The mixture was boiled, diluted, filtered,

`

washed, dried and screened to four to eight mesh before use. This research showed that increasing water content in BDO, increasing temperature and decreasing feed rate help increase BD selectivity. The main liquid produces are MPA, MEK and cyclic acetal.

Shlechter[15, 16] studied the esterification of BDO with acetic acid followed by pyrolysis of the diacetate to BD. The cracking of the diacetate to the unsaturated acetate is a rapid and normal reaction below 500 ^{0}C where no BD is formed, while BD decomposition occurred above 600 ^{0}C. The optimum conditions of operation obtained from laboratory are 585 ^{0}C and contact time of 7.1 seconds.

Recently, BDO dehydration over rare earth metal oxides has been studied. ZrO_2 and Sc_2O_3 can give a relative high 3B2OL selectivity. Basic sites generated by introducing CaO into ZrO_2 can enhance the 3B2OL selectivity [17-19]. The maximum BD selectivity was 94 % with 100 % BDO conversion on a two-bed catalyst system (Sc_2O_3 +Al_2O_3) [20].

The primary goal of this project is to understand how the acid/base properties impact on BD selectivity. BDO dehydration over two forms of alumina are extensively studied and the product distribution are compared. Meanwhile, we used the basic triethylamine to titrate the alumina surface acidic sites to study the modified acid/base properties impact on the BD selectivity. In addition, we are seeking the possible routes to produce value-added chemicals from BDO by tuning the catalyst properties in a dual-bed system. We find that 2,5-dimethylphenol is produced in the dual bed system with the Sc_2O_3 and ZrO_2 as the first and second bed catalyst respectively.

`

Chapter 2 - Modeling of three-way catalytic converter performance with exhaust mixture from natural gas-fueled engines[1]

Abstract

The ability of a three-way catalytic converter (TWC) to treat the exhaust from a natural-gas fueled engine was evaluated by numerical simulation. A comprehensive and thermodynamically consistent surface reaction mechanism describing the surface reactions in the TWC was built by compiling elementary-step reaction kinetics involving CH_4, CO, formaldehyde, NO, NH_3 and N_2O from literature sources. The reaction parameters are taken from literatures and fitting calculations. The mechanism was implemented in a one-dimensional PFR model describing a single channel of the catalyst. The simulation results were evaluated by comparison with field data collected from a TWC operated isothermally at steady-state. The model predicted the major trends in conversion/formation of all species in the TWC over a wide range of air to fuel ratios. Sensitivity analysis was utilized to study the key reaction steps that impact the exhaust emission mole fraction. It was found that methane, NO, CO and formaldehyde are most sensitive to the corresponding adsorption steps, while NH_3 and N_2O are sensitive to the reactions that relate to their formations, such as reactions involving surface hydrogen atoms for NH_3 and NO for N_2O.

2.1. Introduction

In response to stringent environmental regulations, the automotive industry has conducted a substantial amount of research into three-way catalytic converter (TWC) systems to simultaneously remove unburned hydrocarbon (HC), NO_x and CO from the exhaust from gasoline-fueled engines [21]. This includes the development of TWC converter microkinetic models that comprehensively describe the catalytic chemistry on a

[1] Chapter 1 is published Applied Catalysis B: Environmental. F. Zeng, K.L. Hohn, Appl. Catal. B 182 (2016) 570.

`

molecular level [22, 23]. Recently, there is an interest in using TWC for treating the exhaust from natural gas engines due to the New Source Performance Standards promulgated by EPA in January, 2008. In addition, natural gas is the world's fastest growing major energy source and is projected to rise into second place among energy sources by 2040 [2]. For this reason it will be increasingly important to explore catalytic processes to reduce emissions from natural gas-powered engines. The models developed for gasoline engines are insufficient for modeling a TWC for treating emissions from natural gas engines, since they lack detailed chemistry for methane.

The core of the TWC is a multi-channeled ceramic or metallic monolith. A washcoat (catalyst carrier) containing finely dispersed noble metals (Pt, Pd, Rh) and ceria is coated on the wall of the channel, through which exhaust gases flows. The noble metals are the active sites, catalyzing both oxidation and reduction [24]. Ceria is added because of its structural properties, its reversibility of sulfur poisoning and its rapid kinetics of oxygen storage and release [25], however this effect is not considered in the current steady state model. The exhaust emission condition is quantized using the normalized air to fuel ratio as

$$\lambda = \frac{AF_{\text{realistic}}}{AF_{\text{stoichiometric}}}$$

Therefore, $\lambda>1$ corresponds to fuel lean conditions while $\lambda<1$ corresponds to fuel rich conditions. It is widely accepted that the air to fuel ratio has a great impact on the TWC ability to efficiently remove CO and NOx from the exhaust. The efficiency reaches a maximum around the stoichiometric condition ($\lambda=1$) [26]. Research on gasoline [27] and natural gas engines [5] both indicate that there is a trade-off between NO and CO conversion. Fuel-rich conditions produce high NO conversion but low CO conversion, while the opposite trend is noted at fuel-lean condition. Only at air to fuel ratios very close to the stoichiometric point can both components be reduced significantly.

Methane oxidation chemistry over noble metals, particularly platinum and palladium, has been extensively studied. Activation of the C-H bond is generally considered as the rate limiting step for methane combustion and two activation mechanism were proposed on these two metals. Burch and coworker [28] proposed that Pt activates the C-H bond of methane by dissociative adsorption of methane at vacant metal sites, fully covered with

`

oxygen species cannot activate C-H bond. By contrast, Pd is much more effective than Pt at lean conditions, $Pd^{2+}O^{2-}$ ions on PdO surface can more easily activate the C-H bond and PdO is considered as the active phase [29]. The reversible transformation between PdO and metallic Pd is well observed and a correlation has been found between this transformation and methane oxidation activity [30]. Miller and Malatpure [31] indicated that methane total oxidation is correlated to the density of PdO-Pd$*$($*$ is an O-vacancy) site pairs: if the PdO is overstabilized by the support (CeO_2), then it cannot be partially reduced to Pd$*$ to form the site pairs required by the reaction, and activity is decreased. Even though Pd exhibited better methane oxidation performance at lean condition, the complex transformation between metallic palladium and the metal oxide complicates the kinetic modeling of methane oxidation which should include the PdO formation [32].

Methane chemistry over platinum has been investigated for autothermal reforming [33], catalytic partial oxidation [34] and complete oxidation [35]. Burch and Loader compared the methane combustion over Pt/Al_2O_3 and Pd/Al_2O_3, and showed that at higher methane conversions with stoichiometric or rich mixtures Pt/Al_2O_3 is a more active catalyst. They also concluded that platinum can be a more effective catalyst than palladium for methane combustion under real conditions [36].

Lyubovsky and coworkers studied the methane catalytic combustion over Pt-group catalyst both in fuel lean and fuel rich conditions [37]. They showed that the surface is covered with oxygen when reacting with a fuel-lean mixture, while it is covered with CO and H when reacting with a fuel-rich mixture. They suggested that the catalyst had a different state under fuel lean and fuel rich conditions, which resulted in different mechanisms for the interaction of methane with the catalyst. Buyevskaya [38] investigated the role of surface coverage on methane partial oxidation by flowing CH_4 over an initial O_2-treated catalyst. The initial CO_2 selectivity was 100% but the major product produced shifted from CO_2 to CO as the surface oxygen was consumed, indicating that an oxygen-rich catalyst surface promoted the CO_2 formation, while an oxygen-lean surface leads to CO formation.

Due to platinum's high activity for methane oxidation and NOx reduction, detailed elementary-step mechanisms for methane catalytic partial oxidation and NO reduction have been reported on platinum. Hickman and coworker [39] proposed a 19-

`

elementary-step model for methane oxidation under methane-rich conditions on Pt and Rh surfaces. The dissociative adsorption of methane was grouped into a single step and was not reversible. The mechanism indicated that the H_2 and CO are primary products. Deutschmann and coworkers have developed microkinetic models for methane oxidation on rhodium that can be used to simulate steady-state partial oxidation [40] and transient behavior of catalytic monoliths [41]. Vlachos [42] used a hybrid parameter estimation methodology, based on experimental data, semi-empirical methods and first principle density function theory to estimate reaction rate constants for various steps in methane oxidation. The activation energy was both temperature and coverage dependent via the UBI-QEP method. A comprehensive reaction mechanism including methane, CO, formaldehyde and methanol was proposed. The methane dissociative adsorption was separated into four reversible, elementary steps.

NO reduction over platinum had been extensively studied with reducing agents such as H_2, CO, CH_4, propane and propene [43, 44]; H_2 was the most efficient while CH_4 was the least efficient. When hydrogen was used as the reducing agent, NO was reduced to NH_3 [45, 46] , N_2 [46], and slight amounts of N_2O [45]. N_2O formation is favored when NO is reduced by CO [45] and NH_3 [47]. The primary role of hydrogen is to keep the catalyst surface clean by reacting with surface oxygen [48], exposing more vacant sites for the adsorption of NO. Meanwhile, a mechanism [49] suggested that adsorbed NO dissociated to surface nitrogen N_* and surface oxygen O_* with the promotion of vacant Pt sites.

In this paper, we describe a microkinetic model for the TWC applied to natural gas engine exhaust. Due to the lack of microkinetic models of methane oxidation over palladium, notably a lack of a comprehensive mechanism including carbon monoxide, methanol, formaldehyde, we chose to build our TWC model on a platinum reaction mechanism. To create our model, published methane oxidation and NO reduction mechanisms on platinum were combined and modified to fit experimental data while maintaining thermodynamic consistency. The resulting mechanism was used to simulate a commercial TWC [5] applied to reducing the emissions from a natural gas engine over a wide range of air to fuel ratios.

`

2.2. Mathematical Model

The mass balance for the adsorbed species on the solid phase are obtained by assuming competitive adsorption of all species. The adsorption of each species on the catalyst, represented here as a change in species surface coverage (θ_i), at steady state can be calculated as follows:

$$\frac{\partial \theta_i}{\partial t} = 0 \quad (1)$$

$$\frac{\partial \theta_i}{\partial \mathrm{t}} = \Re_{\mathrm{adsorption},i} - \Re_{\mathrm{desorption},i} + \sum_j \Re_{\mathrm{reaction},j} \quad (2)$$

The surface coverage of vacant sites is defined as θ_v:

$$\theta_v = 1 - \sum \theta_i \quad (3)$$

The adsorption rate could be calculated as:

$$\Re_{\mathrm{adsorption},i} = \frac{s_i}{\Gamma}\sqrt{\frac{RT}{2\pi M_i}}\left(\frac{T}{T_0}\right)^{\beta}\exp\left(-\frac{E_{adsorption}}{RT}\right)C_i\theta_v \quad (4)$$

where s is the sticking coefficient, Γ is the site density of the catalyst, R is the gas constant, T is the absolute temperature,T_0=300 K, β is the temperature component and M is the molecular weight.

The desorption rate is formulated as follows:

$$\Re_{\mathrm{desorption},i} = A_{desorption,i}\left(\frac{T}{T_0}\right)^{\beta}\exp\left(\frac{-E_{desorption,i}}{RT}\right)\theta_i \quad (5)$$

The Langmuir-Hinshelwood type rate expressions are used to describe reaction rate:

$$\Re_{reaction,j} = A_{reaction,j}\left(\frac{T}{T_0}\right)^{\beta}\exp\left(\frac{-E_{reaction,j}}{RT}\right)\prod\theta_i \quad (6)$$

Assuming that flow in the channel can be represented as plug flow, we can write the flowrate for each species as:

$$\frac{dF_i}{dz} = \sum_j \Re_{\mathrm{reaction},j}\,\Gamma\;\mathrm{S_m}\,\mathrm{S_{cross}} \quad (7)$$

Where: S_m=catalyst surface area, m^2/m^3, S_{cross}= channel cross section area, m^2.

According to the definition above, at steady state condition, the PFR model equation can be formulated as:

$$\frac{\mathrm{d}F_i}{\mathrm{dz}} = (\Re_{\mathrm{desorption},i} - \Re_{\mathrm{adsorption},i})\,\Gamma\;\mathrm{S_m}\,\mathrm{S_{cross}} \quad (8)$$

This plug-flow reactor (PFR) model was used to model a single channel in the TWC. The effects of mass transfer limitations in the transport of species to the monolith

`

wall and through the washcoat layer were not considered in our model. To evaluate the validity of ignoring external mass transfer, the transverse Peclet number in a single channel was calculated according to [50]:

$$P_t = \frac{R_{\Omega 1}^2 <u>}{LD_f} \quad (9)$$

$R_{\Omega 1}$ is the effective transverse diffusion length for fluid phase and the value is taken as half the width of the monolith channel, <u> is the average fluid velocity, L is the monolith length, D_f is the molecular diffusivity of the reactant in the fluid phase. The diffusivity at 400 ^{0}C were calculate from the equation developed by Fuller [51]. The diffusivity of CH_4, CO, CH_2O, NO, NH_3 and N_2O are: 8.771×10^{-5}, 8.135×10^{-5}, 7.183×10^{-5}, 7.578×10^{-5}, 10.937×10^{-5} and 7.623×10^{-5} m^2/s respectively. The corresponding calculated Peclet number are 0.7829, 0.8441, 0.9560, 0.9061, 0.6278 and 0.9008. We note that Joshi and coworkers argued that external mass transport could be ignored when they studied H_2 oxidation on a Pt/Al_2O_3 monolithic catalyst with a Peclet number close to unity [52]. Since our calculated Peclet number is close to one, we assume that the exhaust concentration profile is uniform in the transverse direction in each channel. The assumption of no internal mass transport limitations in the washcoat layer was tested by calculating the Thiele modulus ϕ as defined by [50]:

$$\phi^2 = \frac{kR_{\Omega 2}^2}{D_e} \quad (10)$$

where k is the reaction rate constant, $R_{\Omega 2}$=25 μm (assumed washcoat thickness), and D_e is the effective diffusivity of gas in the washcoat as defined below [53]:

$$D_e = \frac{\varepsilon}{\tau} 97a\left(\frac{T}{M_i}\right)^{0.5} \quad (11)$$

Where ε is the porosity, τ is the tortuosity and a is the pore radius. The values are defined below: ε=0.41, τ=8, $a=10^{-8}$ m [53]. In this work, we used the corresponding adsorption step reaction rate constant to calculate the six gas species Thiele moduli in the washcoat and the value are listed below: $\phi_{CH_4} = 0.31, \phi_{NO} = 0.62, \phi_{CO} = 0.68, \phi_{CH_2O} = 0.59, \phi_{NH_3} = 0.68, \phi_{N_2O} = 0.0087$. Because the Thiele moduli are far less than one, internal mass transfer limitation can safely be ignored.

Since experimental data showed that the TWC reactor operated at 400 ^{0}C, with only 5-10 ^{0}C temperature drop measured along the converter [5], we have assumed

`

isothermal conditions in the TWC was operated at a temperature of 400 ^{0}C. Each surface species is expressed in equation (2) and each gas species is expressed by equation (8). Equations (2) and (8) are coupled together to form the differential-algebraic equations and solved using Matlab solver ode15s. The definitions of all variables are listed in Table 2-1.

Table 2-1. Notation.

A	Pre-exponential factor
C	Exhaust gas concentration [mol/m^3]
D_e	Effective diffusivity of gas in the washcoat [m^2/s]
D_f	Molecular diffusivity of the reactant in the fluid phase [m^2/s]
E	Activation energy [kJ/mol]
F	Exhaust flow rate [mol/s]
L	Monolith reactor length [m]
M	Molecular weight [g/mol]
P_t	Transverse Peclet number
R	Gas constant [J/mol/K]
$\Re$	Reaction rate [s^{-1}]
$R_{\Omega 1}$	Effective transverse diffusion length for fluid phase [m]
$R_{\Omega 2}$	Washcoat thickness [m]
s	Sticking coefficient
$S_{i,j}$	Sensitivity coefficient matrix
S_m	Catalyst surface area [m^2/m^3]
S_{cross}	Channel cross section area [m^2]
t	Time [s]
T	Catalyst temperature [K]
<u>	Average fluid velocity [m/s]
y	Mole fraction
z	Axis coordinate
ε	Porosity
τ	Tortuosity

`

Γ	Catalyst site density [mol/m^2]
θ	Surface coverage
ϕ	Thiele modulus
λ	Normalized air to fuel ratio
β	Temperature component
Subscripts	
i	Species
j	Reaction number
v	Vacant sites

2.3. Model Validation

Reaction parameters for the equations above were obtained from literature sources. However, since these values were typically derived for a system other than the TWC treating natural-gas engine exhaust, it is necessary to test and modify the model so that it can represent this system. To accomplish this, the model results were compared to experimental data from Defoort et al [5]. Their data were obtained by using a commercial TWC consisting of a stainless steel substrate with an alumina (Al_2O_3) and ceria (CeO_2) washcoat with platinum, palladium and rhodium precious metals. The cell density was approximately 75 cells per square centimeter. Four catalyst units were installed, the dimensions of each were 30 cm×40 cm×7.5 cm. The nominal temperature was 400 ^{0}C with a 5-10 ^{0}C temperature decrease across the catalyst. This catalyst was placed downstream of a Superior 6G-825 four-stroke natural gas engine with six cylinders with a bore and stroke of 25.4 cm. During steady state test, the engine speed and load were held constant and the air to fuel ratio was varied between 0.953 and 1.03. Exhaust flowrate is about 7.4 m^3/s. Oxygen was measured by a Rosemount five-gas analyzer, other compounds of interest were measured using a Nicolet FTIR. H_2 concentrations are assumed to equal one third of the CO concentration [3, 54]. Exhaust gas mixture composition are given in Table 2-2.

Table 2-2. Exhaust gas mixture composition entering TWC, balanced with N_2.

λ	1.030	1.012	0.992	0.987	0.977	0.953
O_2 (%)	0.84	0.57	0.41	0.29	0.24	0.29

`

CO (ppm)	232.39	289.73	858.47	1281.92	2608.51	7960.65
CO_2 (ppm)	94444	96771	95673	94843	94755	92772
H_2 (ppm)	77.46	96.58	286.16	427.31	869.50	2653.55
H_2O (%)	18.30	17.75	19.13	20.18	19.88	18.66
CH_4 (ppm)	110.67	171.79	239.89	249.69	300.45	317.01
CH_2O (ppm)	9.13	9.62	7.87	6.30	4.55	2.52
NO (ppm)	2817.42	2518.59	2189.19	2068.51	1893.25	1399.16
NH_3 (ppm)	0.49	0.89	0.59	2.51	4.95	1.87
N_2O (ppm)	3.35	2.47	1.84	1.60	1.05	0.29

2.4. Results and discussion

2.4.1. Surface reaction mechanism

The fundamental requirement for the surface reaction mechanism is that it should include both methane oxidation and NO reduction; however a comprehensive and validated mechanism involved these two chemistries is not available in the literature. In this work, we combined the NO reduction mechanism from different researchers [23, 55, 56] with a validated methane oxidation model [42]. The surface reaction mechanism for C1 and NO reactions are shown in Table 2-3 and Table 2-4 respectively. In our surface mechanism for NO reduction, we considered the following products: NH_3, N_2, and N_2O. Defoort et al. showed that NO_2 concentration was zero both pre and post of the TWC [5], so reaction steps involving NO_2 were not considered.

Table 2-3. Surface reaction mechanism for C1 reactions on platinum [42]. Underlined parameters indicate values that were change in this work from the literature values to improve the model fit to experimental data (six reaction parameters had been changed).

NO.	Reaction	s/A ($1/s^{-1}$)	β	Ea (kcal/mol)
Adsorption				
1	$O_2 + 2* \rightarrow 2O*$	5.42E-2	0.766	0
2	$O+*\rightarrow O*$	4.91E-2	0.25	0
3	$CO+*\rightarrow CO*$	1E0	0	0

`

4	$CO_2+*\rightarrow CO_{2*}$	1.95E-1	0.25	0
5	$H_2+2*\rightarrow 2H*$	1.29E-1	0.858	0
6	$OH+*\rightarrow OH*$	9.99E-1	2	0
7	$H_2O+*\rightarrow H_2O*$	1.08E-1	1.162	0
8	$H+*\rightarrow H*$	3.84E-1	1.832	0
9	$COOH+*\rightarrow COOH*$	6.34E-2	-0.089	0
10	$HCOO+2*\rightarrow HCOO**$	1.46E-1	0.201	0
11	$C+*\rightarrow C*$	1.64E-2	0.156	0
12	$CH+*\rightarrow CH*$	1.35E-2	0.051	0
13	$CH_2+*\rightarrow CH_{2*}$	4.5E-2	0.118	0
14	$CH_3+*\rightarrow CH_{3*}$	1.6E-1	-0.099	0
15	$CH_4+2*\rightarrow CH_{3*}+H*$	0.58	0.154	$1.56+w\times\theta_{CO}^{a}$
16	$CH_3OH+*\rightarrow CH_3OH*$	3.34E-1	0.258	0
17	$CH_3O+*\rightarrow CH_3O*$	1.49E-1	0.054	0
18	$CH_2O+*\rightarrow CH_2O*$	0.7016	0.098	0
19	$CHO+*\rightarrow CHO*$	1.14E-2	0.096	0
20	$CH_2OH+*\rightarrow CH_2OH*$	5.26E-2	0.233	0
Reaction				
21	$CO_{2*}+*\rightarrow CO*+O*$	4.18E10	0.177	26.3
22	$CO*+O*\rightarrow CO_{2*}+*$	2.39E11	-0.177	20.6
23	$OH*+*\rightarrow O*+H*$	1.95E12	1.872	27.1
24	$O*+H*\rightarrow OH*+*$	6.33E12	0.624	8.8
25	$H_2O*+*\rightarrow H*+OH*$	9.36E12	-0.118	17.8
26	$H*+OH*\rightarrow H_2O*+*$	9.99E12	-1.049	13.5
27	$H_2O*+O*\rightarrow 2OH*$	4.32E10	0.082	8.8
28	$2OH*\rightarrow H_2O*+O*$	1.7E10	0.325	22.7
29	$CO_{2*}+H*\rightarrow CO*+OH*$	8.03E8	-0.531	6.0
30	$COOH*+*\rightarrow CO*+OH*$	8.43E8	0.024	5.3
31	$CO*+OH*\rightarrow COOH*+*$	1.19E9	-0.024	19.1
32	$COOH*+*\rightarrow CO_{2*}+H*$	1.06E11	0.549	1
33	$CO_{2*}+H*\rightarrow COOH*+*$	9.45E10	-0.549	2.4

`

34	$CO_*+H_2O_*\rightarrow COOH_*+H_*$	1.01E11	0.492	23.7
35	$COOH_*+H_*\rightarrow CO_*+H_2O_*$	9.07E10	-0.492	5.6
36	$CO_{2*}+OH_*\rightarrow COOH_*+O_*$	5.35E10	0.097	26.6
37	$COOH_*+O_*\rightarrow CO_{2*}+OH_*$	1.87E11	-0.097	6.9
38	$CO_{2*}+H_2O_*\rightarrow COOH_*+OH_*$	8.64E10	-0.031	17.5
39	$COOH_*+OH_*\rightarrow CO_{2*}+H_2O_*$	1.16E11	0.031	11.9
40	$CO_*+OH_*\rightarrow CO_{2*}+H_*$	1.25E9	0.531	18.5
41	$CO_{2*}+H_*\rightarrow HCOO_{**}$	1.12E11	-0.422	18.5
42	$HCOO_{**}\rightarrow CO_{2*}+H_*$	8.96E10	0.422	0
43	$CO_{2*}+OH_*+*\rightarrow HCOO_{**}+O_*$	6.17E10	0.236	36.8
44	$HCOO_{**}+O_*\rightarrow CO_{2*}+OH_*+*$	1.62E11	-0.236	0
45	$CO_{2*}+H_2O_*+*\rightarrow HCOO_{**}+OH_*$	1.02E11	0.095	25.8
46	$HCOO_{**}+OH_*\rightarrow CO_{2*}+H_2O_*+*$	9.78E10	-0.095	3
47	$CH_{3*}+H_*\rightarrow CH_4+2*$	<u>3.012E11</u>	-0.154	<u>3.86</u>
48	$CH_{3*}+ *\rightarrow CH_{2*}+H_*$	1.11E11	0.419	19.7
49	$CH_{2*}+H_* \rightarrow CH_{3*}+ *$	8.99E10	-0.419	17.3
50	$CH_{2*}+ *\rightarrow CH_*+H_*$	5.22E10	0.222	9
51	$CH_*+H_* \rightarrow CH_{2*}+ *$	1.92E11	-0.222	35.4
52	$CH_*+ *\rightarrow C_*+H_*$	9.11E10	0.398	31.3
53	$C_*+H_* \rightarrow CH_*+ *$	1.1E11	-0.398	13.2
54	$CH_{3*}+O_*\rightarrow CH_{2*}+OH_*$	1.97E11	-0.23	10.8
55	$CH_{2*}+OH_* \rightarrow CH_{3*}+O_*$	5.08E10	0.23	26.6
56	$CH_*+OH_* \rightarrow CH_{2*}+O_*$	1.1E11	0.414	44.7
57	$CH_{2*}+O_* \rightarrow CH_*+OH_*$	9.1E10	-0.414	0
58	$C_*+OH_*\rightarrow CH_*+O_*$	6.37E10	0.225	27.7
59	$CH_*+O_* \rightarrow C_*+OH_*$	1.57E11	-0.225	27.5
60	$CH_{2*}+H_2O_* \rightarrow CH_{3*}+OH_*$	8.19E10	0.099	14.1
61	$CH_{3*}+OH_* \rightarrow CH_{2*}+H_2O_*$	1.22E11	-0.099	12.3
62	$CH_*+H_2O_* \rightarrow CH_{2*}+OH_*$	1.81E11	0.269	34
63	$CH_{2*}+OH_* \rightarrow CH_*+H_2O_*$	5.53E10	-0.269	3.3

`

64	$C_*+H_2O_* \rightarrow CH_*+OH_*$	1.04E11	0.09	15.6
65	$CH_*+OH_* \rightarrow C_*+H_2O_*$	9.61E10	-0.09	29.3
66	$CO_*+*\rightarrow C_*+O_*$	2.85E11	0.468	54.9
67	$C_*+O_*\rightarrow CO_*+*$	3.51E10	-0.468	0.3
68	$CO_*+H_* \rightarrow CH_*+O_*$	3.12E11	0.073	45.8
69	$CH_*+O_* \rightarrow CO_*+H_*$	3.21E10	-0.073	9.3
70	$CO_*+H_*\rightarrow C_*+OH_*$	4.97E11	-0.168	40.7
71	$C_*+OH_* \rightarrow CO_*+H_*$	2.01E10	0.168	4.4
72	$2CO_*\rightarrow C_*+CO_{2*}$	5.94E11	0.393	48.8
73	$C_*+CO_{2*}\rightarrow 2CO_*$	1.68E10	-0.393	0
74	$CH_3OH_*+*\rightarrow CH_3O_*+H_*$	7.82E10	0.102	18.8
75	$CH_3O_*+H_* \rightarrow CH_3OH_*+ *$	1.28E11	-0.102	4.3
76	$CH_3O_*+*\rightarrow CH_2O_*+H_*$	1.25E11	0.192	0
77	$CH_2O_*+H_* \rightarrow CH_3O_*+*$	8.03E10	-0.192	14.7
78	$CH_2O_*+*\rightarrow CHO_*+H_*$	2.85E13	0.27	3.6
79	$CHO_*+H_* \rightarrow CH_2O_*+*$	5.60E13	-0.27	21
80	$CHO_*+* \rightarrow CO_*+H_*$	7.11E10	0.33	0
81	$CO_*+H_* \rightarrow CHO_*+*$	1.41E11	-0.33	30.8
82	$CH_3OH_*+*\rightarrow CH_2OH_*+H_*$	8.48E10	0.403	8.7
83	$CH_2OH_*+H_*\rightarrow CH_3OH_*+*$	1.18E11	-0.403	14.6
84	$CH_2OH_*+*\rightarrow CH_2O_*+H_*$	1.14E11	-0.104	7.9
85	$CH_2O_*+H_*\rightarrow CH_2OH_*+*$	8.77E10	0.104	2.2
Desorption				
86	$2O_*\rightarrow O_2+2*$	8.41E12	-0.796	$51-32\theta_O$
87	$O_*\rightarrow O+*$	1.44E13	-0.25	$85-16\theta_O$
88	$CO_*\rightarrow CO+*$	5.66E15	-0.5	$40-15\theta_{CO}$
89	$CO_{2*}\rightarrow CO_2+*$	3.63E12	-0.25	3.6
90	$2H_*\rightarrow H_2+2*$	7.95E12	-0.001	$19.8-6\theta_H$
91	$OH_*\rightarrow OH+*$	1.44E14	2	$63-33\theta_O+25\theta_{H2O}$
92	$H_2O_* \rightarrow H_2O+*$	2.03E12	1.372	$10-2.5\theta_{H2O}+25\theta_{OH}$
93	$H_*\rightarrow H+*$	4.37E13	1.890	$62-3\theta_H$

`

94	$COOH_* \rightarrow COOH + *$	1.12E13	0.089	55.3
95	$HCOO_{**} \rightarrow HCOO + 2*$	4.83E12	-0.201	53.0
96	$C_* \rightarrow C + *$	4.3E13	-0.156	157.7
97	$CH_* \rightarrow CH + *$	5.22E13	-0.051	157.1
98	$CH_{2*} \rightarrow CH_2 + *$	1.57E13	-0.118	91.6
99	$CH_{3*} \rightarrow CH_3 + *$	4.42E12	0.099	45.3
100	$CH_3OH_* \rightarrow CH_3OH + *$	2.11E12	-0.258	9.5
101	$CH_3O_* \rightarrow CH_3O + *$	4.73E12	-0.054	37
102	$CH_2O_* \rightarrow CH_2O + *$	<u>6.448E13</u>	-0.098	12
103	$CHO_* \rightarrow CHO + *$	6.21E13	-0.096	55.5
104	$CH_2OH_* \rightarrow CH_2OH + *$	1.35E13	-0.233	50

[a] w=0.89 for fuel lean conditions and 30.31 for fuel rich conditions.

Table 2-4. Surface reaction mechanism for NO reactions on platinum proposed in this work. Underlined parameters indicate values that were adjusted to improve the model fit to experimental data.

NO.	Reaction	s/A (1/s-1)	β	E(kJ/mol)
Adsorption				
105	$NO + * \rightarrow NO_*$	0.85 [23]	0	0
106	$NH_3 + * \rightarrow NH_{3*}$	1 [56]	0	0
107	$N_2O + 2* \rightarrow NO_* + N_*$	0.01 [55]	0	<u>23</u>
Reaction				
108	$NO_* + * \rightarrow N_* + O_*$	<u>9E14</u>	0	107.8 [55]
109	$N_* + O_* \rightarrow NO_* + *$	1.005E13[55]	0	<u>168</u>
110	$N_* + N_* \rightarrow N_2 + 2*$	1.005E13[55]	0	<u>81.9</u>
111	$N_* + 3H_* \rightarrow NH_{3*}$	<u>2.005E16</u>	0	<u>69</u>
112	$NH_{3*} + 3* \rightarrow N_* + 3H_*$	<u>1.005E12</u>	0	<u>110.2</u>
Desorption				
113	$NO_* \rightarrow NO + *$	<u>1.005E14</u>	0	<u>100</u>
114	$NH_{3*} \rightarrow NH_3 + *$	<u>1.06E16</u>	0	<u>88.4</u>
115	$NO_* + N_* \rightarrow N_2O + 2*$	<u>1.005E11</u>	0	<u>75.8</u>

`

One significant challenge for the model developed in this work was the fact that it is being used to simulate both fuel lean and fuel rich conditions. At fuel rich conditions, the surface is covered by partial oxidation species, CO and H in particular, while at fuel lean conditions, the surface is covered by oxygen, differences in surface coverages will result in differences in how methane interacts with the catalyst [37]. Meanwhile, Chatterjee and coworkers modeled the CO, C_3H_6 and NO conversion at fuel rich, near stoichiometric and fuel lean condition and pointed out the C_3H_6 conversion was largely over estimate in the fuel rich condition compared to the experimental data. The deviation was explained by the fact that in the rich condition a wide variety of surface species, such as partial oxidation product of C_3H_6, resides on catalyst surface, which can reduce the oxygen surface coverage and lead to different reaction pathway [23]. To account for this, the activation energy for methane adsorption was written as a function of CO surface coverage differently in the fuel rich and fuel lean condition. The activation energy was represented by: $1.56+0.89\times\theta_{CO}$ for fuel lean and $1.56+30.31\times\theta_{CO}$ for fuel rich (θ_{CO} is the initial surface coverage of carbon monoxide). The higher weight factor indicates that the high CO surface coverage at fuel rich condition increases the dissociative adsorption activation energy and will greatly inhibit the adsorption of methane, which leads to a low conversion of methane at fuel rich conditions. Meanwhile, the methane sticking coefficient was increased from 0.116 to 0.58, which is close to 0.68 proposed by Aghalayam and coworkers [57]. Similar parameters tuning procedure had been done by Maestri and coworkers to increasing the methane sticking coefficient on Rh from 0.229 to 0.572 to better predict experimental results [58].

Model predictions as a function of λ are shown in Figure 2-1. These results are compared to experimental data obtained by Defoort et al [5]. As seen in Figure 2-1, the simulation can capture all the important trends except that ammonia is under-estimated at one fuel rich condition (λ =0.953); however the NH_3 formation trend is predicted, with little ammonia formation at fuel lean conditions and increased amounts as λ shifts from fuel lean to fuel rich conditions. Methane conversion increases as λ decreases to the stoichiometric point from the lean condition and conversion suddenly decreases to about 10% at fuel rich conditions. The cause of the lower methane conversion at fuel rich

`

conditions is not due to insufficient oxygen in the exhaust since there is still a large amount of oxygen downstream of the converter. Instead, we propose that the higher surface coverage of CO in fuel rich conditions impacts methane conversion. For this reason, we have modeled the methane dissociative adsorption activation energy differently at fuel rich conditions than fuel lean conditions. This approach acknowledges the literature that shows that the methane interaction mechanism is different at fuel rich conditions due to high CO surface coverage [37]. The NO conversion is low at fuel lean conditions due to excessive oxygen and a limited amount of reducing agents, while as λ decreases, NO conversion gradually increases until the stoichiometric point, at which point there is a step change in NO conversion to 100%. The formaldehyde conversion is consistently high at all conditions while CO conversion decreases to 63.07% at fuel rich condition (λ =0.953) with the CO mole fraction (7960 ppm) tripling compared to the next data point (λ =0.977). N_2O mole fraction did not exhibit a noticeable change after flowing through the converter. The mole fraction is several ppm except one point that is over 10 ppm.

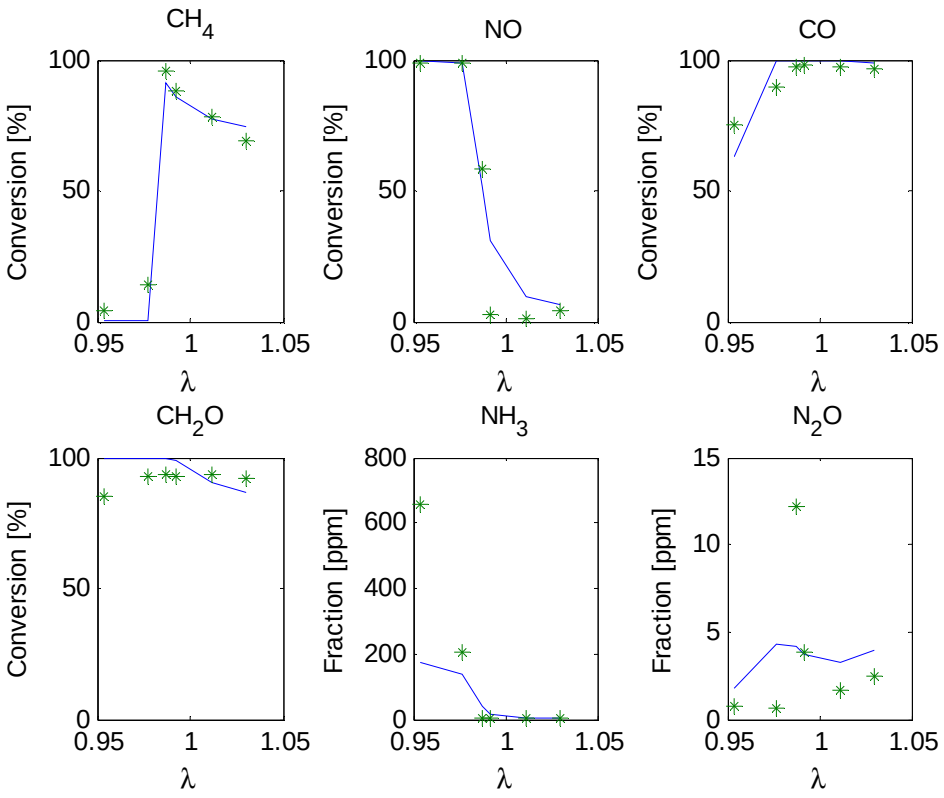

`

Figure 2-1. Simulation of exhaust gas conversion and formation in TWC. Lines are the simulation and symbols are the experimental data.

Figure 2-2 compares the simulated oxygen concentrations as a function of position in the catalytic converter for different λ's. This figure shows that when λ=0.953, the oxygen concentration gradually decreases and reaches zero at about 0.05 m. It is notable that conversion of oxygen is much higher than that in the experimental data (20.68%). Meanwhile, the corresponding CO conversion is 63.07% which is slightly under predicted. We can make two conclusions based on the simulation results. First, the CO conversion at fuel rich conditions is not as high as that at fuel lean conditions since there is insufficient oxygen for complete oxidation of CO. Second, CO conversion is slightly under predicted because the consumption of oxygen is overestimated. When λ=0.977, oxygen concentration decreases initially and then remains at a high concentration through the rest of the converter. The remaining oxygen was sufficient to cause the CO conversion to be higher than that found experimentally.

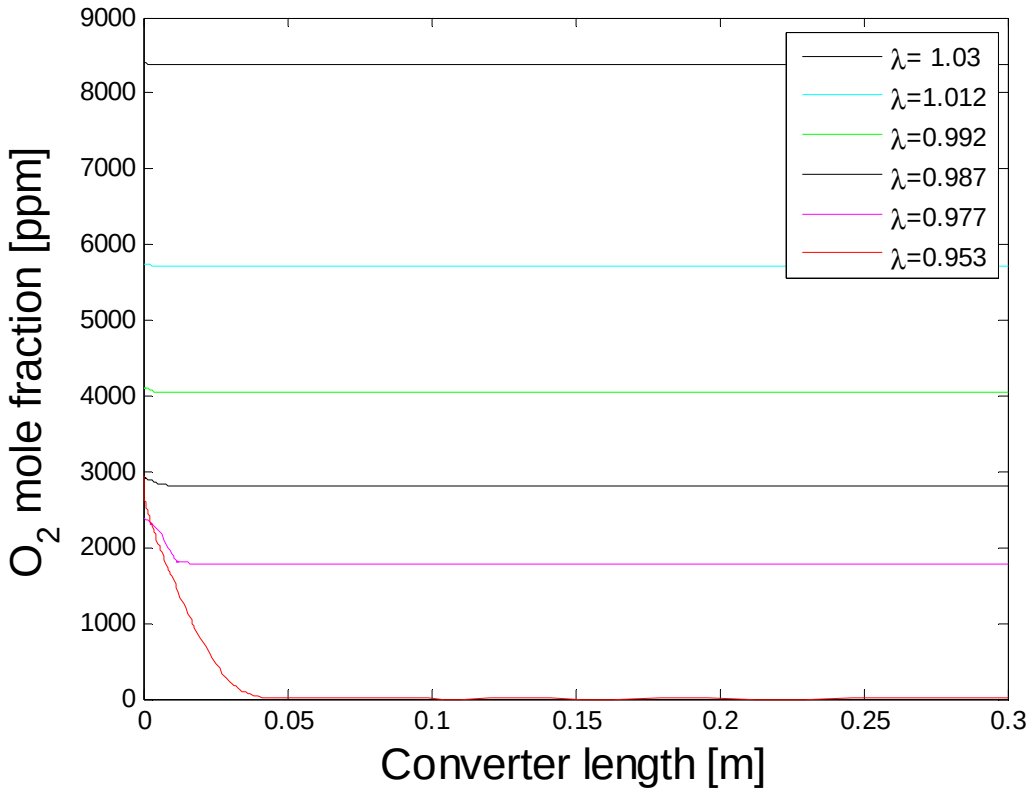

`

Figure 2-2. Oxygen mole fraction in exhaust mixture as a function of converter length at various air to fuel ratio.

2.4.2. Simulated exhaust compositions

Figure 2-3 and Figure 2-4 depict the exhaust composition along the catalyst converter at fuel lean (λ=1.03) and fuel rich (λ=0.977) compositions, respectively. As seen in these figures, O_2, CH_4, CO, CH_2O and NO concentration decrease along the converter, while the CO_2, NH_3, N_2O, N_2 concentration increase along the converter. This trend is consistent with experimental observations and represent the general chemistry happening in the catalytic converter. Even though the N_2 concentration is not available in the experimental data, based on the nitrogen mass balance, we can determine that N_2 was produced in the NO reduction process. For both compositions, all reaction chemistry is essentially complete by 0.1 m: only minor changes in gas phase compositions are noted past that point.

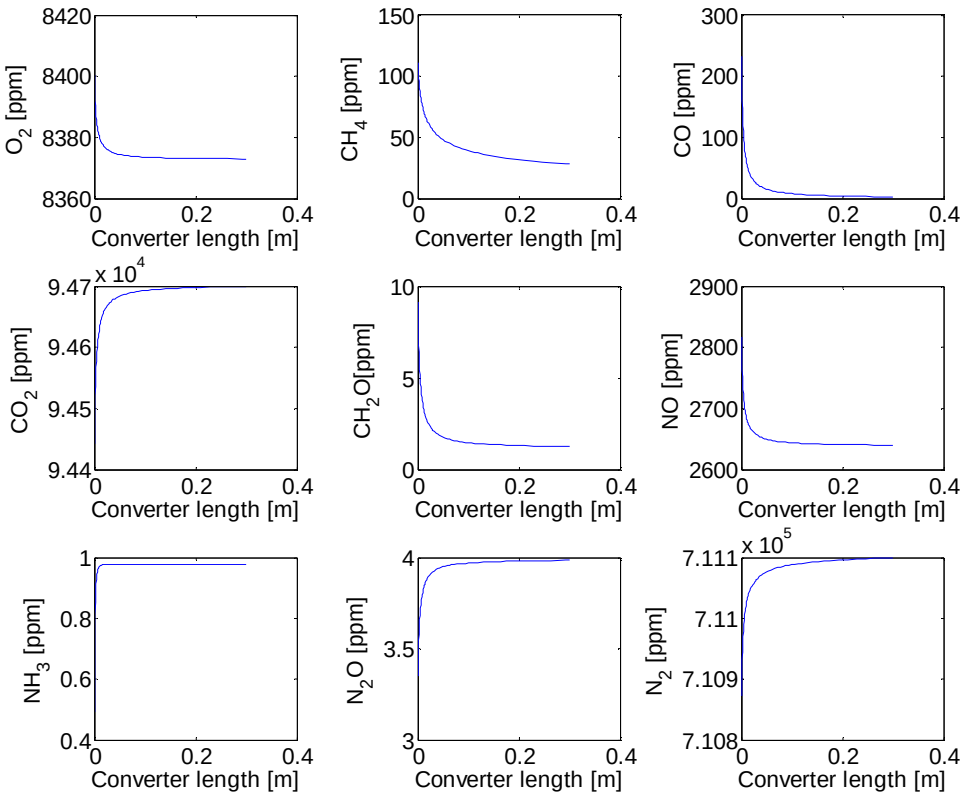

`

Figure 2-3. Exhaust composition as a function of position in the catalytic converter with a fuel lean inlet mixture (λ=1.03).

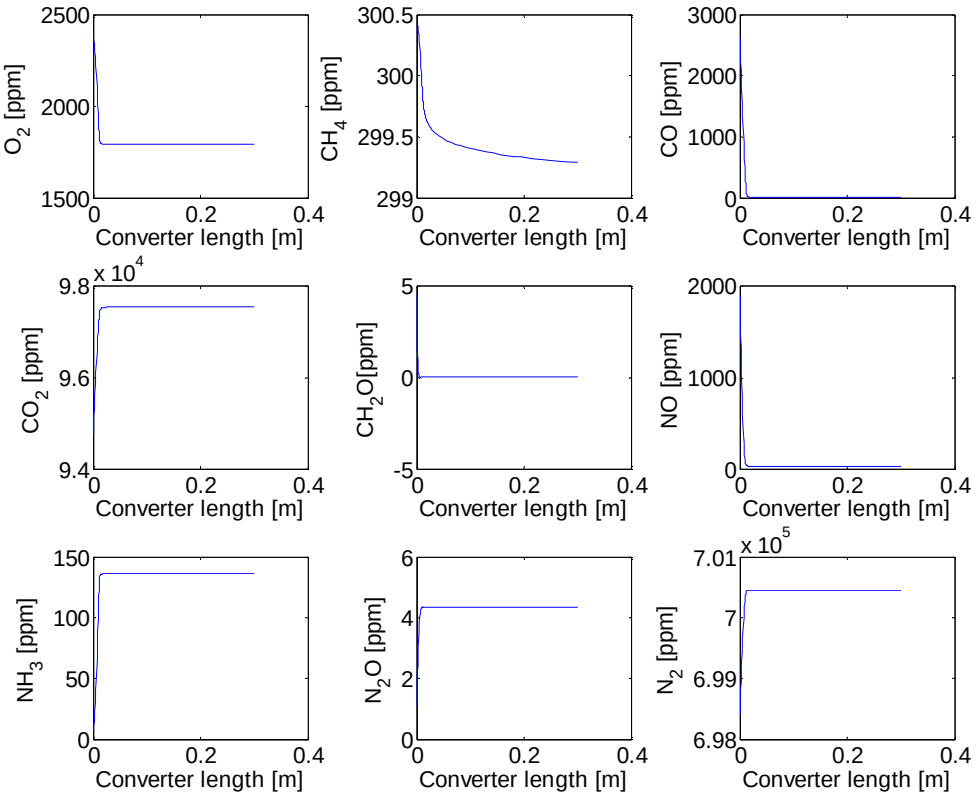

Figure 2-4. Exhaust composition as a function of position in the catalytic converter with a fuel rich inlet mixture (λ=0.977).

2.4.3. Simulated surface coverages

The calculated surface coverage of all species in both fuel lean (λ=1.03) and rich (λ=0.977) conditions are shown in Figure 2-5. OH$_*$ and H$_2$O$_*$ are the dominant species on the Pt surface for both conditions because the H$_2$O concentration is about 19% in the exhaust. NO surface coverage exhibits a steeper decrease at the entrance of TWC at the fuel rich condition than that at fuel lean condition indicated that NO$_*$ was converted along the converter which is consistent with the observation that NO conversion is higher at fuel rich conditions. The N$_*$ surface coverage is higher in the fuel rich condition, which results from higher conversion of NO through decomposition into N$_*$ and O$_*$. Meanwhile,

`

it can be seen that H_* surface coverage increases as λ shifts from lean to rich. The high N and H surface coverage in the fuel rich condition lead to the higher NH_3 surface coverage at fuel rich condition, and ultimately higher amounts of NH_3 in the exhaust under fuel rich condition. For the fuel rich condition, it can be seen that the coverage of vacant sites initially increases at the entrance of the converter then decreases, while for the fuel lean condition, vacant sites coverage continuously decrease along the converter. The trend for fuel rich conditions can be attributed to the removal of adsorbed CO near entrance of the convertor, followed by adsorption of H_2O later in the convertor after the major reactions are complete. The vacant sites surface coverage is consistently higher in the fuel rich condition than that in the fuel lean condition. More vacant sites would promote the adsorption of NO, leading to higher NO conversion under fuel rich conditions, but this does not help explain why the experimentally measured methane conversion is low at fuel rich conditions. CO coverage decreases as the reactants progress through the reactor for both conditions, while the initial CO surface coverage at fuel rich condition is much higher than that in the fuel lean condition due to the 10 times higher gas concentration than that in the fuel lean condition. The higher CO surface coverage under fuel rich conditions was taken as the factor that increased the methane dissociative adsorption activation energy to explain the low conversion at fuel rich conditions. High CO surface coverage under fuel rich condition would promote NO_* decomposition by removing O_*.

`

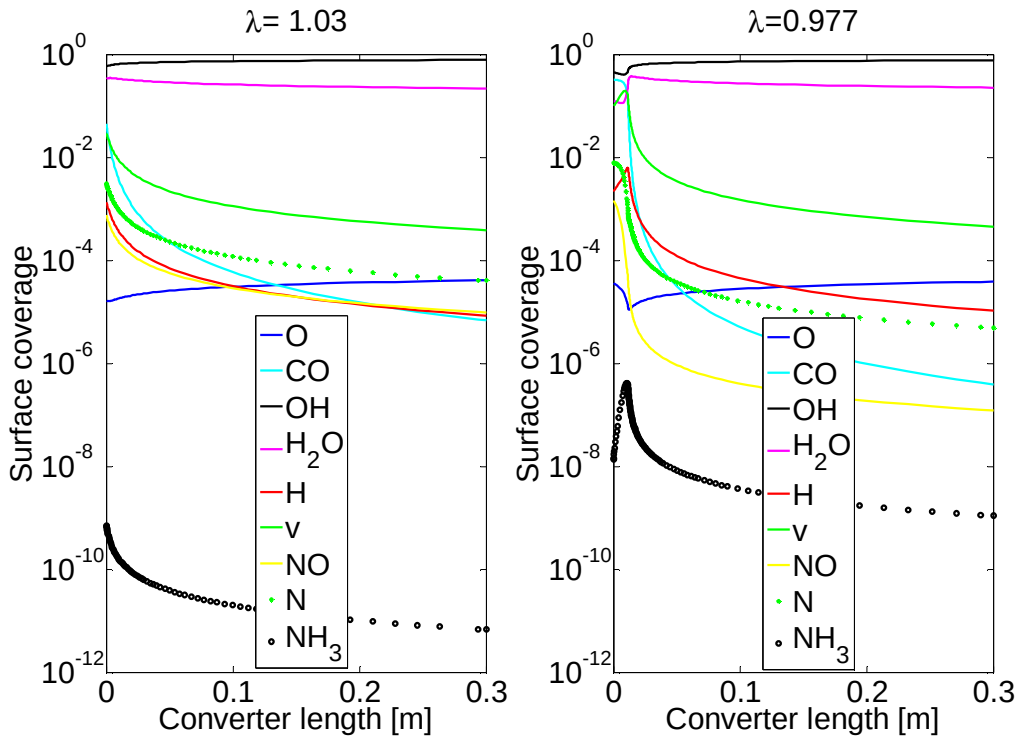

Figure 2-5. Simulated surface coverage on catalyst surface as a function of converter length at various air to fuel ratio, v represents the vacant sites. Fuel lean condition (left, λ=1.03) and fuel rich condition (right, λ=0.977).

NO conversion exhibited an opposite trend compared to methane: the NO conversion is relatively high at fuel rich conditions, but it rapidly decreases in the transition from fuel rich to lean conditions, finally reaching a low value (<10%) for λ=1.03. Methane, CO and H_2 are all potential reducing agents to convert NO to N_2 and NH_3. However, R108 ($NO_* + * \rightarrow N_* + O_*$) indicated that the adsorbed NO further decomposes to N_* and O_*, and then reducing agents CO_* and H_* can react with the O_* (R22 and R24), leaving vacant sites which also explained why the vacant sites initially increased in the fuel rich conditions.

To investigate NO chemistry, simulations were performed by omitting surface O_* generation from R108 in eq. (2). These simulations showed that NO conversion and vacant sites surface coverage increased, which indicated that oxygen inhibited the NO reduction by taking the vacant sites for NO adsorption and further decomposition. A similar conclusion was reached by Koop and Deutschmann, who found that CO and C_3H_6 inhibited the oxidation of NO by blocking the adsorption sites for the dissociative adsorption of oxygen [22]. As the NO

`

conversion decreased, NH_3 formation decreased correspondingly, which indicated that NH_3 formed from the precursor NO and this reaction occurred in the TWC, not during fuel combustion in the engine [59].

2.4.4. Thermodynamic consistency

To check the thermodynamic consistency of the kinetic parameters of the whole mechanism, the reaction enthalpy and entropy of elementary reaction were related to activation energy and pre-exponential factor of a given forward and backward reaction [60]

$$\Delta H_j = E_j^f - E_j^b \qquad (12)$$

$$A_j^f / A_j^b = e^{\Delta S_j / R} \qquad (13)$$

For adsorption, sticking coefficients s_i were used. The pre-exponential factor for the adsorption reaction is given as [61]:

$$A_{i,sticking} = s_i \left(\frac{RT}{2\pi M_i}\right)^{1/2} \qquad (14)$$

The original C1 mechanism used to develop our microkinetic model is thermodynamically consistent [42]. In order to simulate TWC performance, the pre-exponential factor of both forward and backward reactions were perturbed by the same order to maintain thermodynamic consistency. For example, the reaction pair consisting of formaldehyde adsorption (R18) and desorption (R102) were changed in Table 2-3. The methane dissociation adsorption activation energy was reduced from original value 9 kcal/mol to 1.56 kcal/mol, meanwhile the corresponding methane formation reaction R47 ($CH_{3*}+H_* \rightarrow CH_4+2_*$) activation energy was decreased by the same amount to maintain thermodynamic consistency.

To ensure thermodynamic consistency for the NO reduction portion of our model, we have calculated enthalpy and entropy changes using a thermodynamic database and compare those values to the values obtained from the activation energies and pre-exponentials in the microkinetic model. For example, for the overall reaction $NO+2.5H_2=NH_3+H_2O$, enthalpy and entropy changes were calculated from the GRI-Mech thermochemical database, giving values of ΔH of -90.58 kcal/mol and ΔS of -37.25 cal/(mol K) at 300 K. By summing the activation energies and pre-exponentials of the individual surface reaction steps and using equations (10) and (11),values for ΔH and ΔS were found to be -89.13 kcal/mol and -37.23 cal/(mol K) respectively. For the second gas phase reaction $N_2O+0.5O_2=2NO$, the same calculations was carried out. In the gas phase, ΔH and ΔS are 24.12 kcal/mol and 23.64 cal/(mol K) respectively;

`

based on the model, they are 24.12 kcal/mol and 22.79 cal/(mol K). Thus, we proposed a thermodynamically consistent surface reaction for the natural gas engine exhaust in TWC.

2.4.5. Sensitivity analysis

Since the reaction mechanism is large, it is difficult to identify the important reaction steps influencing a response without a systematical method [62]. In this work, we examine sensitivity coefficients when determining the important reactions. The pre-exponential factor (A) was chosen as the parameter and the exit emission mole fraction (y) as the response. The sensitivity coefficient is defined as:

$$S_{i,j} = \frac{\partial(lny_i)}{\partial(lnA_j)} = \frac{lny_i^0 - lny_i}{lnA_j^0 - lnA_j} \qquad (15)$$

Here, A_j^0 and A_j denote the initial pre-exponential factor and perturbed pre-exponential factor, respectively. The pre-exponential factor of each elementary reaction was perturbed by a same factor. y_i^0 and y_i are the species mole fraction using A_j^0 and A_j, respectively. In this calculation, exit exhaust mole fraction was chosen as the response for sensitivity coefficient calculations [63].

Figure 2-6 shows the reactions that are important to the six key exhaust species. The sensitivity analysis was performed for each exhaust by decreasing the pre-exponential factor of each elementary reaction by a factor of 1.2. The sensitivity coefficient are further normalized to the largest absolute value in each data set (NSC), so the maximum NSC value in each set is 1.0. With a threshold value of 0.16 for the absolute value, as shown in the figure, methane, NO and CO are all most sensitive to the adsorption steps (R15, R105 and R3, respectively). Aghalayam and coworkers modelled the methane oxidation on platinum and sensitivity analysis also showed that methane conversion is most sensitive to the methane dissociative adsorption step [57]. These species are converted in the TWC, so it makes sense that their adsorption plays the biggest role in their chemistry. However, Figure 2-6 also shows how these three species are impacted by reaction steps involving each other. For example, reaction steps R105 (NO $+* \rightarrow$ NO$*$), R113 (NO$* \rightarrow$ NO $+ *$) and R108 (NO$* + * \rightarrow$ N$*$ + O$*$) have noticeable NSC values for methane, NO, and CO. These three steps are for NO adsorption, NO desorption, and decomposition to N$*$ and O$*$, clearly indicating how NO can occupy surface sites that can otherwise be used for methane and CO conversion. In a similar way, CO adsorption has a large impact on methane conversion. Finally, oxygen adsorption (R1) had a noticeable negative impact on NO conversion since the

`

sign is opposite to the NO adsorption (R105). This can be explained by considering that oxygen inhibits NO_* decomposition (R108) on the surface. Formaldehyde conversion is primarily sensitive to the formaldehyde adsorption step R18 ($CH_2O+*\rightarrow CH_2O_*$), the formaldehyde desorption step R102 ($CH_2O_* \rightarrow CH_2O+*$) and surface reaction R78 ($CH_2O_*+*\rightarrow CHO_*+H_*$); however, it has some dependence on NO chemistry due to competitive adsorption. The ammonia and N_2O are most sensitivity to reactions that related to the formation of these two species since both NH_3 and N_2O are produced within the TWC. R25 ($H_2O_*+*\rightarrow H_*+OH_*$) and R26 ($H_*+OH_*\rightarrow H_2O_*+*$) both had a noticeable impact on the NH_3, which indicates that ammonia formation competes with other reactions involving H_*. Surface reactions R105 ($NO +*\rightarrow NO_*$), R108 ($NO_* + * \rightarrow N_* + O_*$) and R113 ($NO_* \rightarrow NO + *$), which are all related to the NO surface concentration, are shown in the ammonia and N_2O sensitivity analysis, since NO is the nitrogen source for their formation. R111 ($N_* + 3H_* \rightarrow NH_{3*}$) is the surface reaction that leads to ammonia formation on the surface.

The sensitivity analysis provides information not only on which reactions are important, but also suggest which reactions should be modified to better capture the experimental results. The reaction parameters reported in Table 2-3 and Table 2-4 were found using sensitivity analysis to decide which reaction parameters should be modified.

`

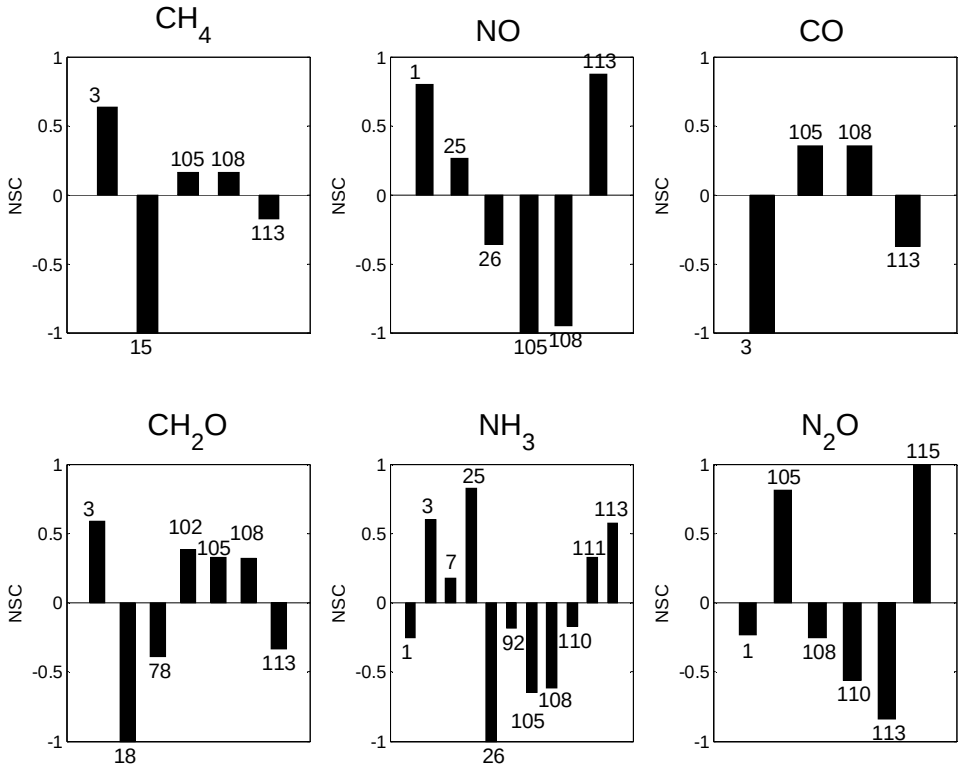

Figure 2-6. Sensitivity analysis of CH_4, NO, CO, CH_2O, NH_3 and N_2O mole fraction with respect to pre-exponential factors at reaction conditions, λ=1.03. The numbers are referring to the reactions listed Table 2-3 and Table 2-4.

2.5. Conclusion

A detailed and thermodynamically consistent surface reaction mechanism capable of modelling all the key reactions in the TWC applied to treat exhaust from a natural-gas engine was developed by selecting the elementary-step reactions from the literature. By adjusting six of the 104 reaction steps in C1 mechanism and proposing a NO reduction mechanism, the model was able to predict the major trends in CH_4, NO, and CO conversion and NH_3 and N_2O production over a wide range of fuel to air ratios. A comprehensive reaction mechanism and sensitivity analysis to determine the important reaction steps are essential for the modeling process and predicting the experiment results. With a fuel rich feed (λ=0.953), CO conversion is a little underpredicted due to the high conversion of O_2 which leads to insufficient oxygen for further CO oxidation. Conversion of NO is high at fuel rich conditions because reducing agents

`

such as CO and H_2 can remove the O_* and promote the decomposition of NO_* into N_* and O_*, which accelerates the conversion of NO. In fuel lean conditions, CO was almost completely converted, and excessive oxygen further decreased the surface CO concentration. Because of this, dissociative adsorption of methane is less inhibited by the surface CO. NO conversion is low at fuel lean conditions because NO decomposition on the surface was inhibited by the high concentration of oxygen and also by less reducing agent to remove O_*. A small variation of the air-fuel ratio had a great impact on the simulated converter performance, showing the importance of maintaining the air to fuel ratio in a narrow stoichiometric window to obtain a high emission removal efficiency. Sensitivity analysis indicated that adsorption steps have the largest impact on removing methane, NO, CO and formaldehyde. Ammonia and N_2O, which are produced in the TWC, are sensitive to the reactions that relate to their formation, such as R25, R26, R108 and R111 for NH_3 and R1, R108 and R115 for N_2O. In addition, the R105 and R108 have large NSC value means that NO adsorption and decomposition steps affect production/conversion of all six important species.

`

Chapter 3 - Modeling of three-way catalytic converter performance with exhaust mixtures from dithering natural gas-fueled engines

Abstract

The behavior of a three-way catalytic converter (TWC) to treat the exhaust from a natural-gas fueled engine in fuel dithering conditions was evaluated by numerical simulation. A validated comprehensive and thermodynamically consistent surface reaction mechanism was utilized to model the natural gas engine exhaust conversion in the TWC at dithering conditions. The mechanism was implemented in a tank-in-series model to study the TWC behavior while air to fuel ratio was cyclically varied (dithering conditions). The simulation results were evaluated by comparison with data collected from a TWC operated at dithering conditions. The microkinetic reaction model predicted the post catalyst THC, NO and CO concentrations well when 5 reaction steps out of 115 elementary steps were modified. The inlet O_2 concentration fluctuation affected the THC, NO and CO conversion. Oxygen promoted the THC and CO oxidation but inhibited the NO reduction. Simulations indicated that the dithering frequency did not noticeably impact the exhaust conversion simply because the transition time is relative short. Larger dithering amplitude decreased the THC conversion because the air fuel ratio shifted to the fuel rich side. Both simulations and experiments showed that dithering yielded improved NO conversion as compared to steady state operation at higher air to fuel ratios. Simulations showed that this was due to a higher number of vacancies with dithering that improved NO adsorption and surface reaction.

3.1. Introduction

Air quality is a worldwide concern that has accelerated stricter emission control requirements on vehicles, such as EPA 10 and EURO VI. In response to these stringent environmental regulations, natural gas fueled engines have attracted extensive attention and have been studied as a promising candidate to meet the emission regulations. It is well known that lean burn natural gas-fueled vehicles produced less CO_2 emission [64] and engine-out emission

`

levels of THC, NO and CO from the natural-gas engine were substantially lower than those of a gasoline engine [65]. In addition, recent forecasts for natural gas resources in the United States suggest that this fuel will be abundant and low cost for many decades [66]. In this way, natural gas engines will have a huge development and it will be increasingly important to investigate the catalytic processes to emissions abatement from natural gas fuel engines.

To control exhaust emissions from natural gas engines, a three-way catalyst (TWC) can be employed that simultaneously converts unburned hydrocarbons, NO_x and CO. The TWC must be operated near the stoichiometric point (λ=1, where $\lambda=AFR_{actual}/AFR_{stoichiometric}$ and AFR refers to the air to fuel ratio) to achieve high conversion of all three species. Another possible method for improving emissions control is to operate the engine in a cyclical fashion, where the AFR is cycled between fuel-rich and fuel-lean conditions. This process is often referred to as dithering. Cho and coworkers studied the AFR oscillatory effect on the performance of a Pt/Al_2O_3 catalyst in gasoline engine exhaust and found that a feed composition oscillation at 0.1 Hz around a time-average stoichiometric point yielded a higher hydrocarbon, NO and CO conversion than steady state conditions below the reaction lightoff temperature [67]. Defoort and coworkers studied the AFR dithering effect on the performance of TWC operating on natural gas-fueled engine and found that the TWC window was widened in the dithering condition (period is 2.5s lean excursion followed by 2.5s rich excursion, amplitude change corresponds to a change in ϕ (ϕ =1/ λ) of about ±0.01) compared to AFR without dithering [5]. Shi and coworker studied the natural gas engine exhaust gas conversion efficiency in TWC under steady state and dithering conditions. They found an optimal midpoint λ, frequency and amplitude to minimize the exhaust emission, but the reaction chemistry was not well understood [6]. It is interesting to notice that both Defoort and Shi's work indicated that the methane conversion efficiency declined on the fuel lean side in the steady state condition, causing the favorable TWC window shift to rich side. Ishii and co-workers found that the H_2O concentration measured in the natural gas engine was higher than that in the base gasoline engine and the methane conversion was reduced in the fuel lean region. They examined the H_2O effect on the methane conversion efficiency and found that a high methane conversion was obtained when the water concentration was zero in the fuel lean region, while as the water concentration increased, the methane conversion sharply decreased in the fuel lean region, which indicated that high water concentration was the main reason that methane conversion was low in the fuel lean region [65].

`

Transient effects are often attributed to oxygen storage, where excess oxygen in air-rich conditions are stored for subsequent use in air-lean conditions. Usually, ceria is proposed as the species responsible for oxygen storage and typically added to TWC because of its structural properties, its reversibility of sulfur poisoning and its rapid kinetics of oxygen storage and release [25].

In our previous work, we have proposed a 115-step elementary microkinetic reaction mechanism to model the steady-state behavior of the TWC in the conversion of exhaust mixture from a natural gas engine [68]. This mechanism was based on microkinetics for platinum. Our simulation predicted the CH_4, NO, CO, CH_2O, NH_3 and N_2O compositions reasonably well over a wide AFR using a plug-flow reactor (PFR) model. In this paper, we utilize the same surface reaction mechanism with minor modifications to model the catalytic conversion of exhaust mixture from natural gas engine while the air to fuel ratio is cycled between different values (dithering). Simulations are compared to experimental results in order to verify the accuracy of the model. Although we recognize the importance of other components besides platinum in the TWC (particularly ceria, which affects transient operation), this first attempt to apply a detailed microkinetic model to treatment of the exhaust from a dithering natural gas engine relies on the previous model that considered platinum as the active catalyst.

3.2. Experimental

All of the experimental results were obtained from a Cummins Onan Generator-Set, a heavy duty Ford 4-stroke cycle (Model LSG-875), 8 cylinder, turbo-charged, spark ignited natural gas engine. The engine was loaded to produce 60 KW at 60 Hz. It utilizes a cast iron block and heads in a 90 degree V-8 configuration. Engine specifications are shown in Table 3-1.

Table 3-1. Engine Specifications

Base Engine	LSG-875, Turbocharged
Displacement in^3 (L)	460.0 (7.5)
Engine Power Output bhp (kW)	173.0 (129.1)
BMEP, psi (kPa)	150.0 (1034.2)
Bore, in. (mm)	4.36 (110.7)
Stroke, in. (mm)	3.85 (97.8)
Piston speed ft/min (m/s)	1155.0 (5.9)

`

Compression Ratio	8.6:1
Lube Oil Capacity, qt. (L)	10.0 (9.5)
Exhaust Gas Flow (Full Load), cfm (m^3/min)	760.0 (21.5)

The engine was operated by a Continental Controls Corporation (CCC) Electronic Gas Carburetor (EGC-2), which utilizes variable pressure control, a patented advanced mixing venturi for natural gas, and a wide band lambda sensor installed upstream of the NSCR catalyst to provide AFR feedback. The EGC-2 can be configured to operate at different AFR values. It can operate in either steady state mode, where PID gains can be optimized to maintain a stable, fixed AFR, or in a dithering mode, where AFR undergoes a sinusoidal variation about a fixed AFR. The AFR set point and dithering conditions (i.e. frequency=0.5 Hz, amplitude=0.005) can be adjusted through input parameters in CCC's Valve Viewer software.

Emissions were treated by a NSCR catalyst manufactured by DCL International Inc., model number A7AL-DQ-1Y07-22, which contains a combination of Pt, Pd and Rh. The catalyst is comprised of two spools, each containing the same substrate configuration and material. The assembled unit was approximately 6 inches in diameter and 17 inches long. Each spool's cylindrical substrate was 5.9 inches in diameter and 3.8 inches long. Emissions were monitored by a Rosemount 5-gas analyzer and a Nicolet 6700 Fourier Transform Infra-Red (FTIR) spectrometer. The 5-gas analyzer measured THC, NO_x, O_2, CO_2, and CO concentrations. Water concentration was measured by FTIR.

Most of the sensors used in this system were too slow to show the time transients required for the modeling work. For this reason, an alternate procedure was used to estimate the concentrations of all gases over time. In this procedure, the data provided by the output voltage from the Woodward narrow band O_2 sensor was used to estimate the concentrations of all species since it provided the highest time resolution. Voltage, equivalence ratio, and 5 gas concentrations were averaged for each five minute data point taken, and then correlated with each other. These discrete averaged points were connected by linear interpolation and the real time voltage signal was used with each relationship to provide real time concentration data for 5 gas species.

`

3.3. Mathematical Model

The TWC is modeled as a series of continuously stirred tank reactors (CSTR). This model can be used to describe a variety of mixing patterns based on the number of tanks used in the model [69]. For a large number of tanks, the CSTRs in series model gives results similar to a plug flow model, which is what is expected for the channels in the TWC. In this model, we used 10 tanks to simulate the exhaust conversion in a commercial TWC. Decreasing the number of tanks to five changed the results by about 2% for all the dithering conditions, and further increasing the number of tanks will not change the conversion significantly, but will increase the computation time. The advantage of using a CSTRs in series model is that algebraic equations can be used to represent the mass balance in each CSTR, so the only differential equation that has to be solved is the time transient that results from dithering. This differs from a non-steady state plug flow reactor which involves solving derivatives in both time and position.

The mass accumulation for the adsorbed species on the solid phase are obtained by assuming competitive adsorption of all species. For the adsorption of each species on the catalyst, represented here as a change in species surface coverage (θ_i), the accumulation on the surface at transient state can be calculated as follows:

$$\frac{\partial \theta_{i,k}}{\partial t} = \Re_{\text{adsorption},i,k} - \Re_{\text{desorption},i,k} + \sum_j \Re_{\text{reaction},j,k} \quad (1)$$

The surface coverage of vacant sites in tank k is defined as $\theta_{v,k}$:

$$\theta_{v,k} = 1 - \sum \theta_{i,k} \quad (2)$$

The adsorption rate could be calculated as:

$$\Re_{\text{adsorption},i,k} = \frac{s_i}{\Gamma}\sqrt{\frac{RT}{2\pi M_i}}\left(\frac{T}{T_0}\right)^{\beta}\exp\left(-\frac{E_{adsorption,i}}{RT}\right)C_{i,k}\theta_{v,k} \quad (3)$$

where s is the sticking coefficient, Γ is the site density of the catalyst, R is the gas constant, T is the absolute temperature,T_0=300 K, β is the temperature component and M is the molecular weight.

The desorption rate is formulated as follows:

$$\Re_{\text{desorption},i,k} = A_{desorption,i}\left(\frac{T}{T_0}\right)^{\beta}\exp\left(\frac{-E_{desorption,i}}{RT}\right)\theta_{i,k} \quad (4)$$

Langmuir-Hinshelwood type rate expressions are used to describe reaction rate:

$$\Re_{reaction,j,k} = A_{reaction,j}\left(\frac{T}{T_0}\right)^{\beta}\exp\left(\frac{-E_{reaction,j}}{RT}\right)\prod \theta_{i,k} \quad (5)$$

`

With the CSTRs-in-series model, the mass balance for each species is:

$$0 = F_{i,k-1} - F_{i,k} - \sum_j (\Re_{\text{adsorption},i,k} - \Re_{\text{desorption},i,k})\, \Gamma S_m \quad (6)$$

where: S_m=active catalyst surface area, m^2/m^3

The geometric surface area per unit reactor volume (GSA) is calculated as:

$$\frac{GSA}{d} = 4 \times (celldensity) \quad (7)$$

where d is the channel diameter, cell density is 197 cells per square inch, and the GSA is calculated using Eq. (7) is 2211 m^2/m^3.

The assumption of no internal mass transport limitations in the washcoat layer was tested by calculating the Thiele modulus ϕ as defined by [50]:

$$\phi^2 = \frac{kR_\Omega^2}{D_e} \quad (8)$$

where k is the reaction rate constant, R_Ω=25 μm (assumed washcoat thickness), and D_e is the effective diffusivity of gas in the washcoat as defined below [53]:

$$D_e = \frac{\varepsilon}{\tau} 97a \left(\frac{T}{M_i}\right)^{0.5} \quad (9)$$

where ε is the porosity, τ is the tortuosity and a is the pore radius. The values are defined below: ε=0.41, τ=8, $a=10^{-8}$ m [53]. In this work, we used the corresponding adsorption step reaction rate constant to calculate the six gas species Thiele moduli in the washcoat. The calculated values are: $\phi_{CH_4} = 0.025, \phi_{NO} = 0.62, \phi_{CO} = 0.68$, because the Thiele moduli are less than one, internal mass transfer limitation can safely be ignored. External mass transfer limitations were not considered in this model.

Table 3-2. Notation.

A	Pre-exponential factor
C	Exhaust gas concentration [mol/m^3]
d	Channel diameter [m]
D_e	Effective diffusivity of gas in the washcoat [m^2/s]
E	Activation energy [kJ/mol]
F	Exhaust flow rate [mol/s]
GSA	Geometric surface area per unit reactor volume [m^2/m^3]
M	Molecular weight [g/mol]
R	Gas constant [J/mol/K]

`

$\Re$	Reaction rate [s^{-1}]
R_Ω	Washcoat thickness [m]
s	Sticking coefficient
t	Time [s]
T	Catalyst temperature [K]
ε	Porosity
τ	Tortuosity
Γ	Catalyst site density [mol/m^2]
θ	Surface coverage
ϕ	Thiele modulus
λ	Normalized air to fuel ratio
β	Temperature component
Subscripts	
i	Species
j	Reaction number
k	Tank number
v	Vacant sites

To simplify the exhaust gas concentration profile for input into our model as the inlet concentration profiled to the TWC, we use a piecewise trapezoid function to describe the pre catalyst emission concentration profile. The real time data and trapezoid function are compared in Figure 3-1 for THC for one of the dithering trials. It can be seen that the trapezoid function can catch the trend quite well except for the extremely sharp peaks. With this procedure, the five gas concentrations can be expressed as functions of time for input to our MATLAB program.

`

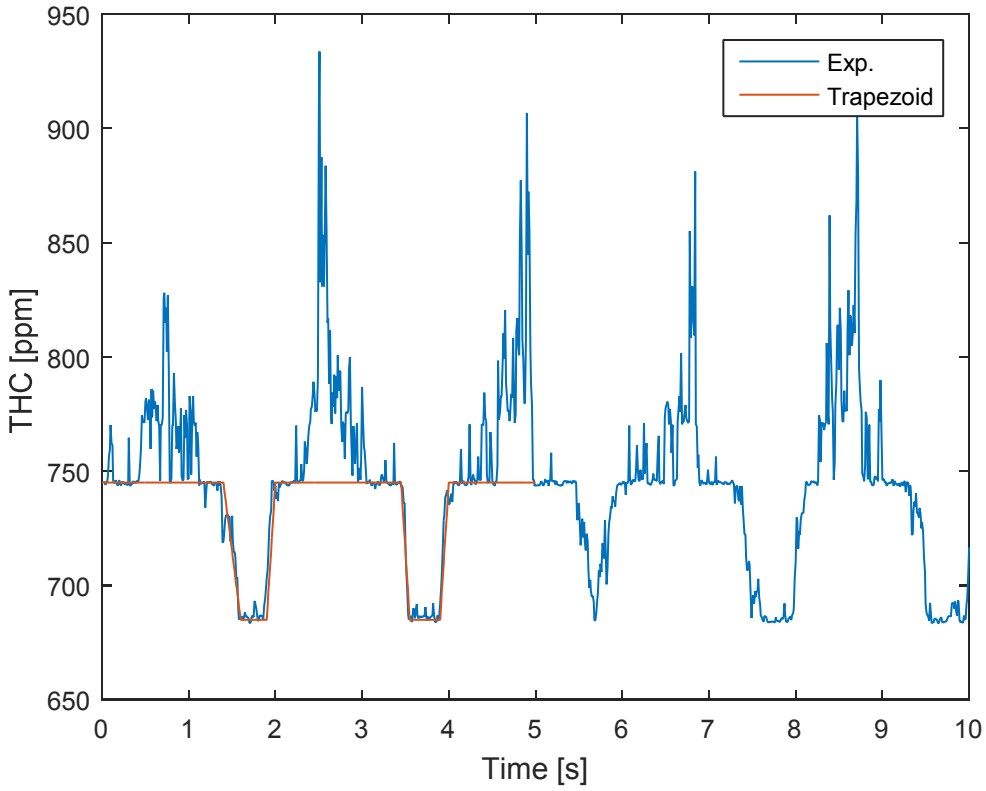

Figure 3-1. Comparison between the measured and simulated pre catalyst THC concentration for dithering at a frequency of 0.5 Hz at an AFR of 17.0.

`

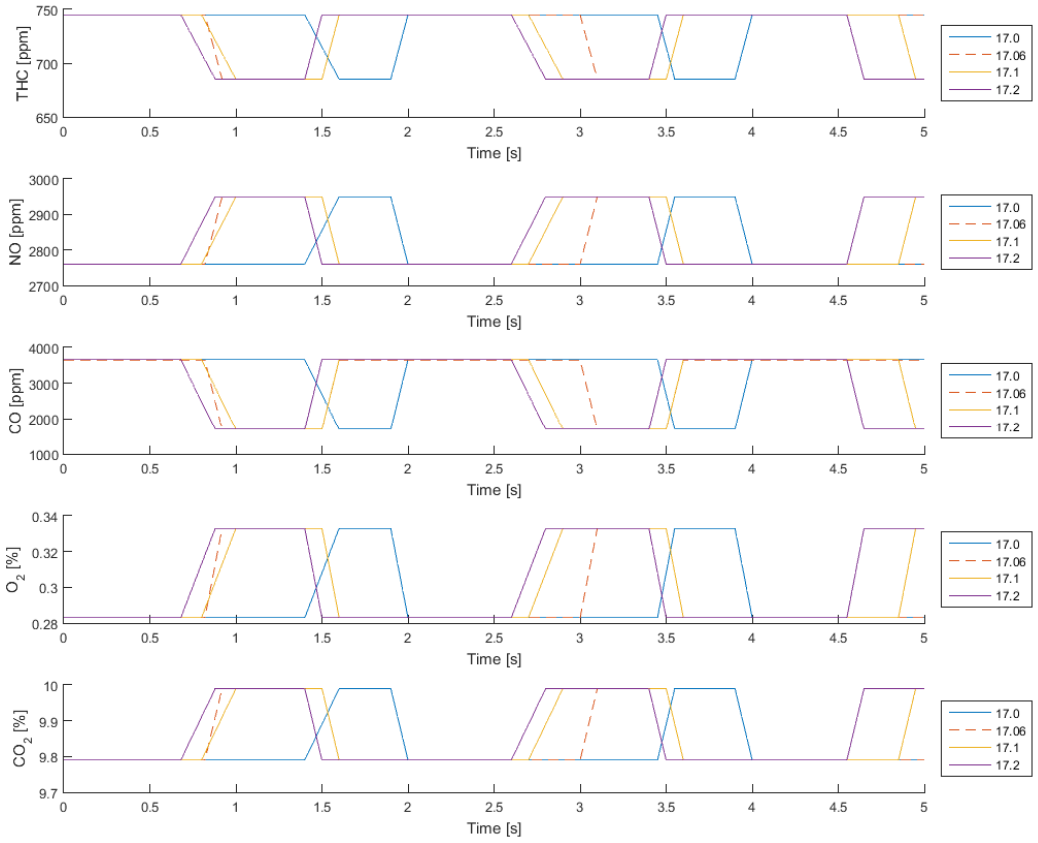

Figure 3-2. THC, NO, CO, O_2 and CO_2 inlet concentration as a function of time for dithering at a frequency of 0.5 Hz at AFR of 17.0, 17.06, 17.1 and 17.2.

Figure 3-2 shows the THC, NO, CO, O_2 and CO_2 simulated inlet concentrations as functions of time at AFR 17.0, 17.06, 17.1 and 17.2. Each of these gave a similar fit to their respective experimental profiles as shown in Figure 3-1. What is surprising about Figure 3-2 is that the maximum and minimum concentrations of all species are identical, even as the nominal AFR is changing. Instead of changing the limits of species concentrations exiting the engine, changing the AFR is changing the period of time over which the engine produces those maximum and minimum times. For example, in the first cycle of AFR 17.0, the THC concentration stays at 745 ppm for 1.4 seconds, while it stays at 685 ppm for only 0.3 seconds. The CO concentration profile had a similar pattern as the THC where more time is spent at high concentration (3660 ppm) than low concentration (1700 ppm). The O_2 concentration profile had a pattern opposite to THC and CO: for the first cycle: 1.4 seconds was spent at an O_2

`

concentration of 0.283 % and 0.3 seconds at 0.333 %. This is consistent with the fact the oxygen concentration is higher in the fuel lean condition than in the fuel rich condition.

Figure 3-3 displays more clearly how changing the AFR set point during dithering impacts the ratio of time spent at the rich and lean conditions by plotting the ratio of these times for different AFR ratios. It is easy to see that as the AFR increase, the ratio of rich to lean time decreases which means that the exhaust compositions are relatively fuel lean at higher AFR.

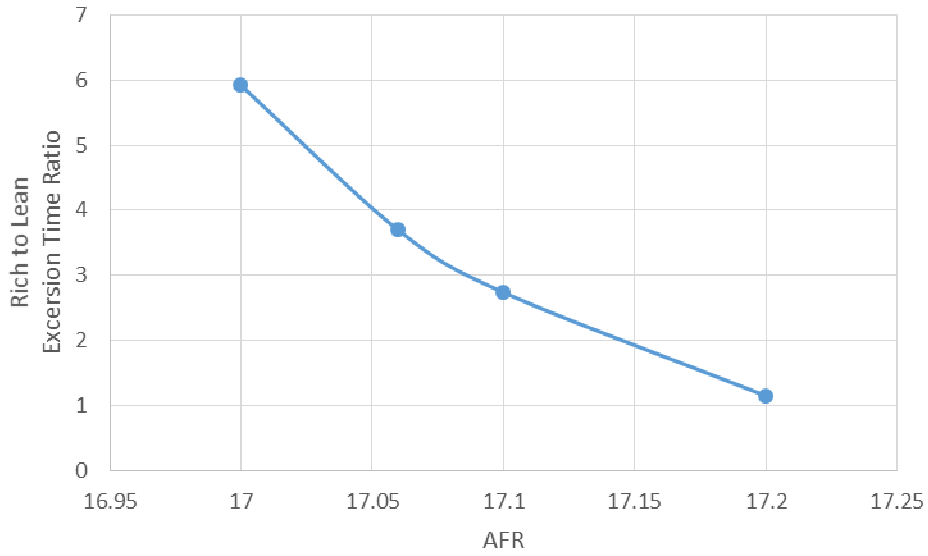

Figure 3-3. Fuel rich to fuel lean excursion time ratio as a function of AFR.

The experimental values for fuel volumetric flowrate, exhaust inlet temperature, catalyst temperature (T1 and T2 are the first and second catalyst spool temperatures), are listed in Table 3-3. The H_2 concentration were assumed to equal one third of the CO concentration [3, 54]. The pre-catalyst water concentration was calculated based on a hydrogen balance for the engine:

$$water\ concentraion\ \% = \frac{4\times(F_{CH4,in}-F_{CH4,out})-2\times F_{H2,out}}{2\times F_{total,out}} \times\ 100 \quad (10)$$

where $F_{CH4,in}$, $F_{CH4,out}$, $F_{H2,out}$ and $F_{total,out}$ are the methane molar flowrate into the engine, methane molar flowrate out of the engine, hydrogen molar flowrate out of the engine and the total exhaust gas molar flowrate out of the engine, respectively.

The experimental data showed that the TWC reactor operated at ~660 ^{0}C, though the inlet gas temperature was about 50 ^{0}C lower. The average temperature variation measured along the converter (between T1 and T2) is less than 10 ^{0}C and the experimentally measured temperatures

`

in the TWC shows a maximum 23 ^{0}C deviation with time, so we have assumed an isothermal reactor. Each surface species is expressed in equation (1) and each gas species is expressed by equation (6). Equations (1) and (6) are coupled together to form the differential-algebraic equations and solved using Matlab ode15s. The definitions of all variables are listed in Table 3-2.

Table 3-3. Dithering operation parameters.

AFR	Fuel flowrate (m^3/min)	Inlet gas temperature T_{in} (^{0}C)	T1 (^{0}F C)	T2 (^{0} C)	H_2O (%)
17	0.399	592.59	659.08	662.61	19.72
17.06	0.399	593.89	661.11	664.44	19.71
17.1	0.399	593.31	659.94	664.17	19.70
17.2	0.399	593.57	657.52	663.72	19.67

3.4. Results and discussion

3.4.1. Surface reaction mechanism

In the experiments, the total hydrocarbons were measured and lumped into one term, THC. THC includes methane, ethane, propane, butane and other hydrocarbons. Since methane is the dominant hydrocarbon in the exhaust, we only consider the methane chemistry in the microkinetic mechanism and methane concentration entering the TWC is taken as the same as the THC.

In our previous work, we proposed a microkinetic surface reaction mechanism to describe the methane oxidation and NO reduction of the natural gas engine exhaust reduction in TWC [68]. In developing this model, we combined the NO reduction mechanism from different researchers [23, 55, 56] with a validated methane oxidation model [42]. In this work, we utilize the same mechanism from our previous work but with a few modifications in the reaction parameters in order to fit the experimental results well. The thermodynamic consistency of the new mechanism is still maintained. The surface reaction mechanism for C1 and NO reactions are shown in Table 3-4 and Table 3-5 respectively. Since the concentration of NO_2 was measured by FTIR to be less than 0.4% of the total NOx composition, with the vast majority of NOx

`

comprised of NO, the reaction steps involving NO oxidation were not considered. The microkinetic mechanism sensitivity analysis was examined in our previous work which indicated that the CH_4 conversion are most sensitive to the adsorption steps [68]. In this work, we modified the CH_4 adsorption steps to better fit the experimental results. The modified reaction parameters are underlined in Table 3-4 and Table 3-5.

Table 3-4. Surface reaction mechanism for C1 reactions. Underlined parameters indicate values that were change in this work from the previous work to improve the model fit to experimental data.

NO.	Reaction	s/A ($1/s^{-1}$)	β	Ea (kcal/mol)
Adsorption				
1	$O_2 + 2* \rightarrow 2O*$	5.42E-2	0.766	0
2	$O+*\rightarrow O*$	4.91E-2	0.25	0
3	$CO+*\rightarrow CO*$	1E0	0	0
4	$CO_2+*\rightarrow CO_{2}*$	1.95E-1	0.25	0
5	$H_2+2*\rightarrow 2H*$	1.29E-1	0.858	0
6	$OH+*\rightarrow OH*$	9.99E-1	2	0
7	$H_2O+*\rightarrow H_2O*$	1.08E-1	1.162	0
8	$H+*\rightarrow H*$	3.84E-1	1.832	0
9	$COOH+*\rightarrow COOH*$	6.34E-2	-0.089	0
10	$HCOO+2*\rightarrow HCOO**$	1.46E-1	0.201	0
11	$C+*\rightarrow C*$	1.64E-2	0.156	0
12	$CH+*\rightarrow CH*$	1.35E-2	0.051	0
13	$CH_2+*\rightarrow CH_{2}*$	4.5E-2	0.118	0
14	$CH_3+*\rightarrow CH_{3}*$	1.6E-1	-0.099	0
15	$CH_4+2*\rightarrow CH_{3}*+H*$	<u>0.116</u>	0.154	<u>$8.5+57\theta_{H2O}-13\theta_{OH}$</u>
16	$CH_3OH+*\rightarrow CH_3OH*$	3.34E-1	0.258	0
17	$CH_3O+*\rightarrow CH_3O*$	1.49E-1	0.054	0
18	$CH_2O+*\rightarrow CH_2O*$	0.7016	0.098	0
19	$CHO+*\rightarrow CHO*$	1.14E-2	0.096	0
20	$CH_2OH+*\rightarrow CH_2OH*$	5.26E-2	0.233	0

`

Reaction				
21	$CO_{2*} + * \rightarrow CO* + O*$	4.18E10	0.177	26.3
22	$CO* + O* \rightarrow CO_{2*} + *$	2.39E11	-0.177	20.6
23	$OH* + * \rightarrow O* + H*$	1.95E12	1.872	27.1
24	$O* + H* \rightarrow OH* + *$	6.33E12	0.624	8.8
25	$H_2O* + * \rightarrow H* + OH*$	9.36E12	-0.118	17.8
26	$H* + OH* \rightarrow H_2O* + *$	9.99E12	-1.049	13.5
27	$H_2O* + O* \rightarrow 2OH*$	4.32E10	0.082	8.8
28	$2OH* \rightarrow H_2O* + O*$	1.7E10	0.325	22.7
29	$CO_{2*} + H* \rightarrow CO* + OH*$	8.03E8	-0.531	6.0
30	$COOH* + * \rightarrow CO* + OH*$	8.43E8	0.024	5.3
31	$CO* + OH* \rightarrow COOH* + *$	1.19E9	-0.024	19.1
32	$COOH* + * \rightarrow CO_{2*} + H*$	1.06E11	0.549	1
33	$CO_{2*} + H* \rightarrow COOH* + *$	9.45E10	-0.549	2.4
34	$CO* + H_2O* \rightarrow COOH* + H*$	1.01E11	0.492	23.7
35	$COOH* + H* \rightarrow CO* + H_2O*$	9.07E10	-0.492	5.6
36	$CO_{2*} + OH* \rightarrow COOH* + O*$	5.35E10	0.097	26.6
37	$COOH* + O* \rightarrow CO_{2*} + OH*$	1.87E11	-0.097	6.9
38	$CO_{2*} + H_2O* \rightarrow COOH* + OH*$	8.64E10	-0.031	17.5
39	$COOH* + OH* \rightarrow CO_{2*} + H_2O*$	1.16E11	0.031	11.9
40	$CO* + OH* \rightarrow CO_{2*} + H*$	1.25E9	0.531	18.5
41	$CO_{2*} + H* \rightarrow HCOO**$	1.12E11	-0.422	18.5
42	$HCOO** \rightarrow CO_{2*} + H*$	8.96E10	0.422	0
43	$CO_{2*} + OH* + * \rightarrow HCOO** + O*$	6.17E10	0.236	36.8
44	$HCOO** + O* \rightarrow CO_{2*} + OH* + *$	1.62E11	-0.236	0
45	$CO_{2*} + H_2O* + * \rightarrow HCOO** + OH*$	1.02E11	0.095	25.8
46	$HCOO** + OH* \rightarrow CO_{2*} + H_2O* + *$	9.78E10	-0.095	3
47	$CH_{3*} + H* \rightarrow CH_4 + 2*$	6.12E10	-0.154	$10.8+57\theta_{H2O}-13\theta_{OH}$
48	$CH_{3*} + * \rightarrow CH_{2*} + H*$	1.11E11	0.419	19.7

`

49	$CH_{2*}+H_* \rightarrow CH_{3*}+*$	8.99E10	-0.419	17.3
50	$CH_{2*}+* \rightarrow CH_*+H_*$	5.22E10	0.222	9
51	$CH_*+H_* \rightarrow CH_{2*}+*$	1.92E11	-0.222	35.4
52	$CH_*+* \rightarrow C_*+H_*$	9.11E10	0.398	31.3
53	$C_*+H_* \rightarrow CH_*+*$	1.1E11	-0.398	13.2
54	$CH_{3*}+O_* \rightarrow CH_{2*}+OH_*$	1.97E11	-0.23	10.8
55	$CH_{2*}+OH_* \rightarrow CH_{3*}+O_*$	5.08E10	0.23	26.6
56	$CH_*+OH_* \rightarrow CH_{2*}+O_*$	1.1E11	0.414	44.7
57	$CH_{2*}+O_* \rightarrow CH_*+OH_*$	9.1E10	-0.414	0
58	$C_*+OH_* \rightarrow CH_*+O_*$	6.37E10	0.225	27.7
59	$CH_*+O_* \rightarrow C_*+OH_*$	1.57E11	-0.225	27.5
60	$CH_{2*}+H_2O_* \rightarrow CH_{3*}+OH_*$	8.19E10	0.099	14.1
61	$CH_{3*}+OH_* \rightarrow CH_{2*}+H_2O_*$	1.22E11	-0.099	12.3
62	$CH_*+H_2O_* \rightarrow CH_{2*}+OH_*$	1.81E11	0.269	34
63	$CH_{2*}+OH_* \rightarrow CH_*+H_2O_*$	5.53E10	-0.269	3.3
64	$C_*+H_2O_* \rightarrow CH_*+OH_*$	1.04E11	0.09	15.6
65	$CH_*+OH_* \rightarrow C_*+H_2O_*$	9.61E10	-0.09	29.3
66	$CO_*+* \rightarrow C_*+O_*$	2.85E11	0.468	54.9
67	$C_*+O_* \rightarrow CO_*+*$	3.51E10	-0.468	0.3
68	$CO_*+H_* \rightarrow CH_*+O_*$	3.12E11	0.073	45.8
69	$CH_*+O_* \rightarrow CO_*+H_*$	3.21E10	-0.073	9.3
70	$CO_*+H_* \rightarrow C_*+OH_*$	4.97E11	-0.168	40.7
71	$C_*+OH_* \rightarrow CO_*+H_*$	2.01E10	0.168	4.4
72	$2CO_* \rightarrow C_*+CO_{2*}$	5.94E11	0.393	48.8
73	$C_*+CO_{2*} \rightarrow 2CO_*$	1.68E10	-0.393	0
74	$CH_3OH_*+* \rightarrow CH_3O_*+H_*$	7.82E10	0.102	18.8
75	$CH_3O_*+H_* \rightarrow CH_3OH_*+*$	1.28E11	-0.102	4.3
76	$CH_3O_*+* \rightarrow CH_2O_*+H_*$	1.25E11	0.192	0
77	$CH_2O_*+H_* \rightarrow CH_3O_*+*$	8.03E10	-0.192	14.7

`

78	$CH_2O*+*\rightarrow CHO*+H*$	2.85E13	0.27	3.6
79	$CHO*+H* \rightarrow CH_2O*+*$	5.60E13	-0.27	21
80	$CHO*+* \rightarrow CO*+H*$	7.11E10	0.33	0
81	$CO*+H* \rightarrow CHO*+*$	1.41E11	-0.33	30.8
82	$CH_3OH*+*\rightarrow CH_2OH*+H*$	8.48E10	0.403	8.7
83	$CH_2OH*+H*\rightarrow CH_3OH*+*$	1.18E11	-0.403	14.6
84	$CH_2OH*+*\rightarrow CH_2O*+H*$	1.14E11	-0.104	7.9
85	$CH_2O*+H*\rightarrow CH_2OH*+*$	8.77E10	0.104	2.2
Desorption				
86	$2O*\rightarrow O_2+2*$	8.41E12	-0.796	$51\text{-}32\theta_O$
87	$O*\rightarrow O+*$	1.44E13	-0.25	$85\text{-}16\theta_O$
88	$CO*\rightarrow CO+*$	5.66E15	-0.5	$\underline{40\text{-}15\theta_{CO}\text{-}62\theta_{H2O}+8\theta_{OH}}$
89	$CO_{2*}\rightarrow CO_2+*$	3.63E12	-0.25	3.6
90	$2H*\rightarrow H_2+2*$	7.95E12	-0.001	$19.8\text{-}6\theta_H$
91	$OH*\rightarrow OH+*$	1.44E14	2	$63\text{-}33\theta_O+25\theta_{H2O}$
92	$H_2O* \rightarrow H_2O+*$	2.03E12	1.372	$10\text{-}2.5\theta_{H2O}+25\theta_{OH}$
93	$H*\rightarrow H+*$	4.37E13	1.890	$62\text{-}3\theta_H$
94	$COOH*\rightarrow COOH+*$	1.12E13	0.089	55.3
95	$HCOO**\rightarrow HCOO+2*$	4.83E12	-0.201	53.0
96	$C*\rightarrow C+*$	4.3E13	-0.156	157.7
97	$CH*\rightarrow CH+*$	5.22E13	-0.051	157.1
98	$CH_{2*}\rightarrow CH_2+*$	1.57E13	-0.118	91.6
99	$CH_{3*}\rightarrow CH_3+*$	4.42E12	0.099	45.3
100	$CH_3OH*\rightarrow CH_3OH+*$	2.11E12	-0.258	9.5
101	$CH_3O* \rightarrow CH_3O+*$	4.73E12	-0.054	37
102	$CH_2O* \rightarrow CH_2O+*$	6.448E13	-0.098	12
103	$CHO* \rightarrow CHO+*$	6.21E13	-0.096	55.5
104	$CH_2OH* \rightarrow CH_2OH+*$	1.35E13	-0.233	50

Table 3-5. Surface reaction mechanism for NO reactions [68].

`

NO.	Reaction	s/A (1/s-1)	β	E(kJ/mol)
Adsorption				
105	$NO + * \rightarrow NO*$	0.85	0	0
106	$NH_3 + * \rightarrow NH_3*$	1	0	0
107	$N_2O + 2* \rightarrow NO* + N*$	0.01	0	23
Reaction				
108	$NO* + * \rightarrow N* + O*$	9E15	0	107.8
109	$N* + O* \rightarrow NO* + *$	1.005E14	0	168
110	$N* + N* \rightarrow N_2 + 2*$	1.005E13	0	81.9
111	$N* + 3H* \rightarrow NH_3*$	2.005E16	0	69
112	$NH_3* + 3* \rightarrow N* + 3H*$	1.005E12	0	110.2
Desorption				
113	$NO* \rightarrow NO + *$	1.005E14	0	100
114	$NH_3* \rightarrow NH_3 + *$	1.06E16	0	88.4
115	$NO* + N* \rightarrow N_2O + 2*$	1.005E11	0	75.8

In Figure 3-4, Figure 3-5, Figure 3-6 and Figure 3-7, we compare the dithering (frequency of 0.5 Hz) experimental and simulation results at AFR 17.0, 17.06, 17.1 and 17.2, respectively. Because the inlet composition to the TWC are varied cyclically, we'd expected the outlet compositions to also demonstrate cyclic behavior. However, it is difficult to discern such a trend in the experimental results. The simulation results predict outlet concentrations that mirror the assumed trapezoidal shape of the inlet compositions. Other than the difference in shape, the THC, NO, CO and CO_2 post catalyst concentration are well predicted by the model on average, while the O_2 concentration are overestimated. The oxygen sensor is not optimized for the concentrations seen in this work, so there may be considerable error in the measured oxygen concentrations.

`

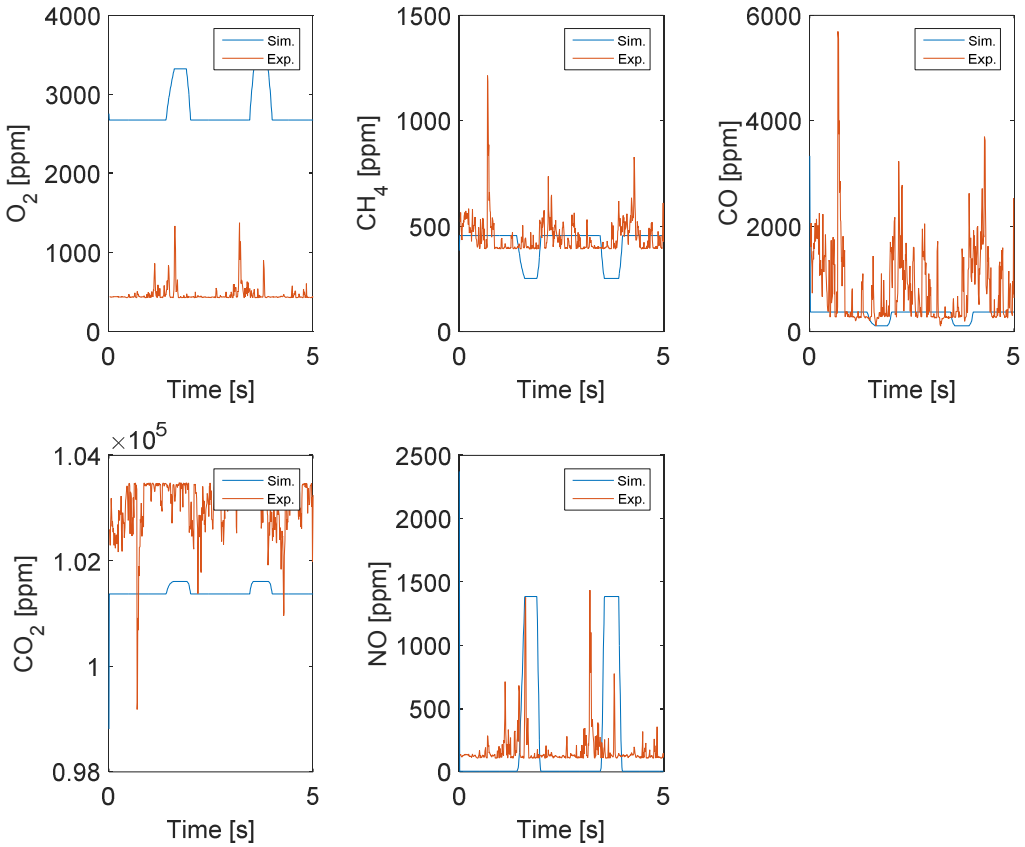

Figure 3-4. AFR 17.0 dithering experimental and simulation results.

`

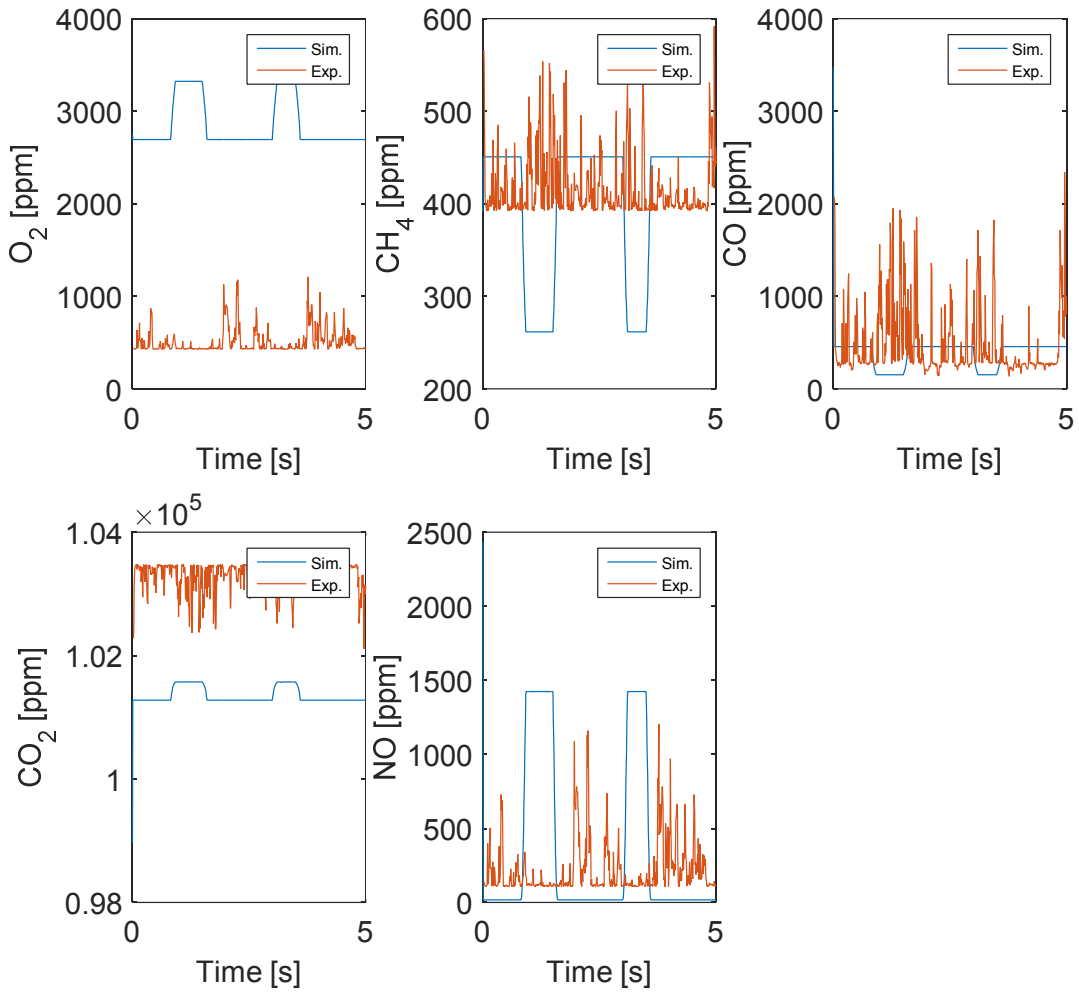

Figure 3-5. AFR 17.06 dithering experimental and simulation results.

`

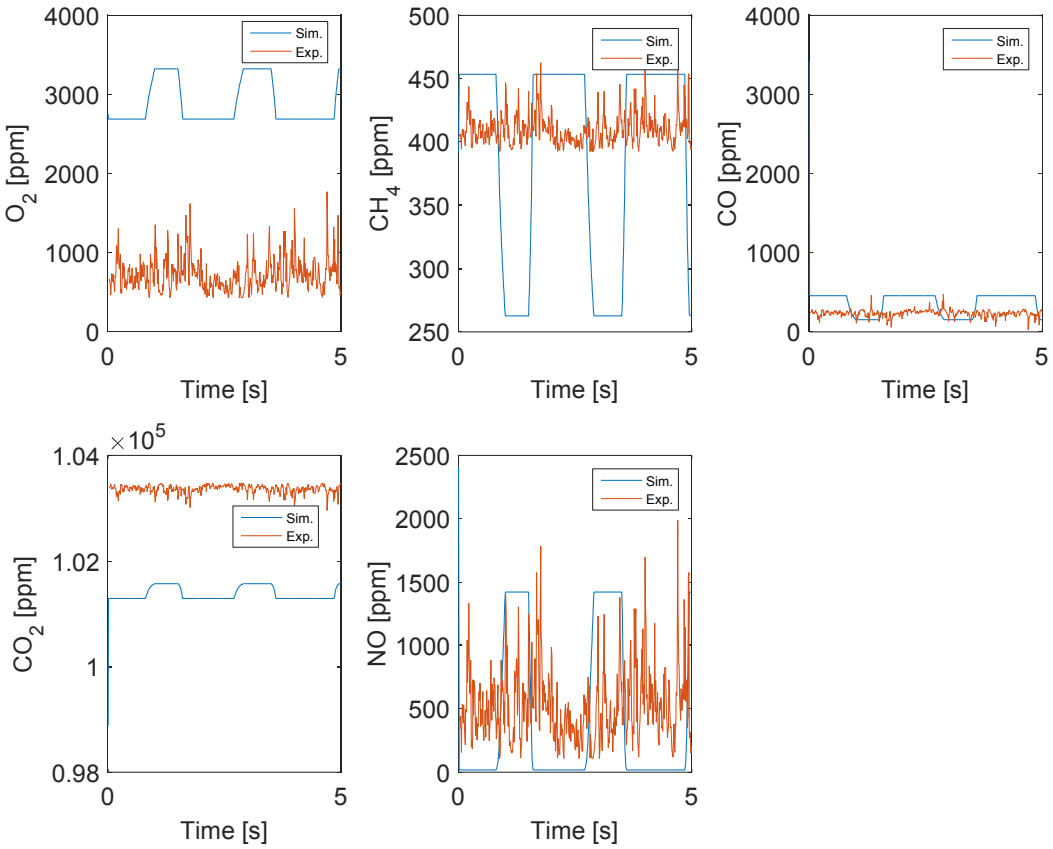

Figure 3-6. AFR 17.1 dithering experimental and simulation results.

`

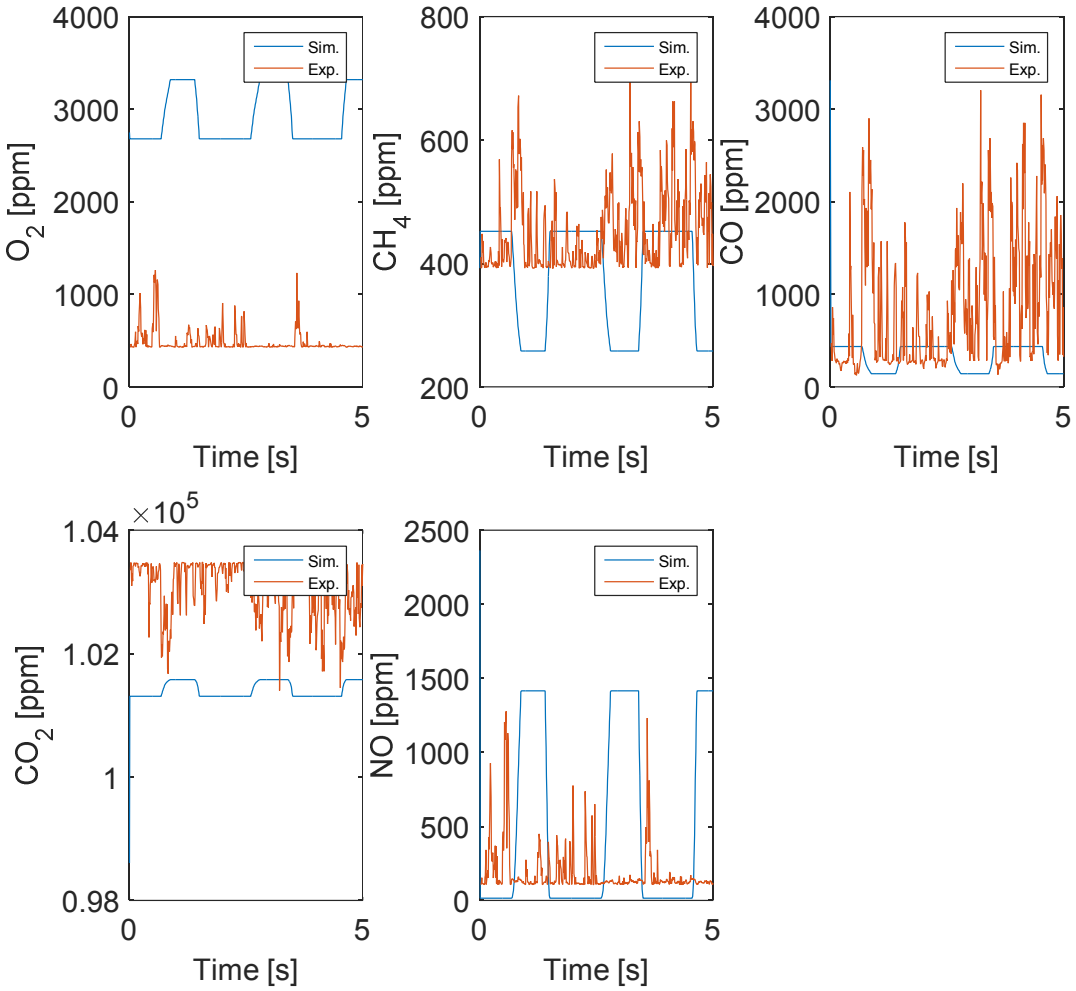

Figure 3-7. AFR 17.2 dithering experimental and simulation results.

`

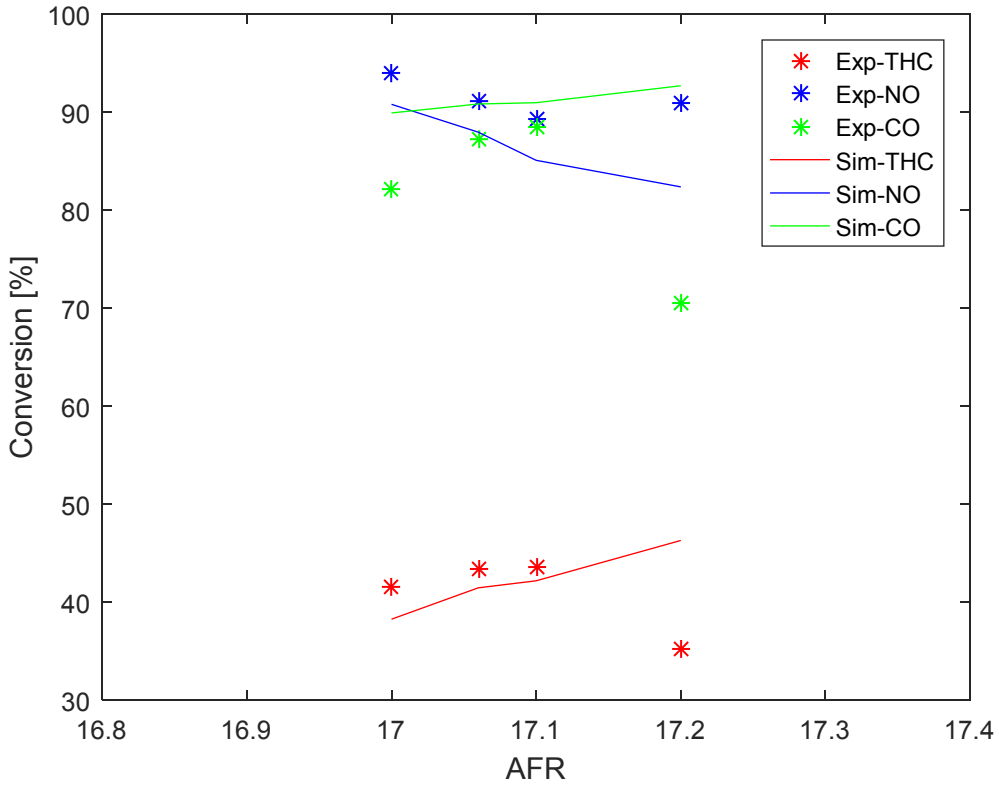

Figure 3-8. Comparison of THC, NO and CO average conversion in dithering condition between experimental and simulation results (frequency=0.5 Hz, amplitude=0.005).

Figure 3-8 compares the simulated THC, NO and CO average conversion with the experimental results at AFR 17.0, 17.06, 17.1 and 17.2. The model generally fits the experimental results, except that experimentally the THC and CO conversions suddenly decrease at AFR 17.2. The simulation results indicated that the THC and CO conversion increase while the NO conversion decrease as the AFR increase, which is consistent with the our previous simulation results of emission conversion in the TWC [68].

`

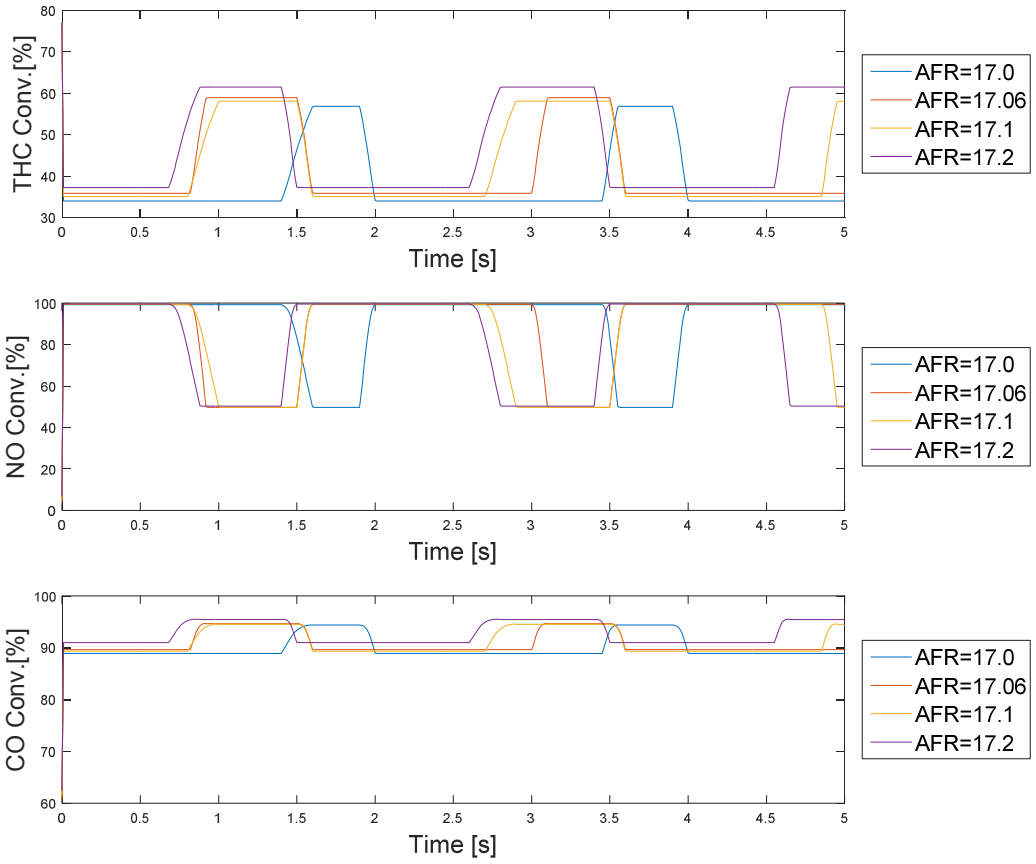

Figure 3-9. Simulated THC, NO and CO conversion in dithering condition as a function of time.

Figure 3-9 shows the simulated THC, NO and CO conversion at four AFRs (17.0, 17.06, 17.1 and 17.2) as a function of time. As seen in this figure, the species conversions for all AFR vary between essentially the same high and low conversion but spend different amounts of time at those conversions. This mirrors the trend noted for the inlet compositions, where increasing AFR led to longer times spent at fuel-lean conditions relative to fuel-rich conditions. In Figure 3-2, it is easy to find that when O_2 concentration increases, the NO concentration increases at the same time while the THC and CO concentrations decrease. In Figure 3-9, the NO conversion decreases as the O_2 concentration increases. This is likely due to inhibition of NO* dissociation (R108 $NO_* + * \rightarrow N_* + O_*$) due to competitive adsorption of oxygen. In contrast, the CO and THC conversion both increase as the O_2 inlet concentration increases because O_2 can promote the oxidation of THC and CO.

`

3.4.2. Simulated surface coverages

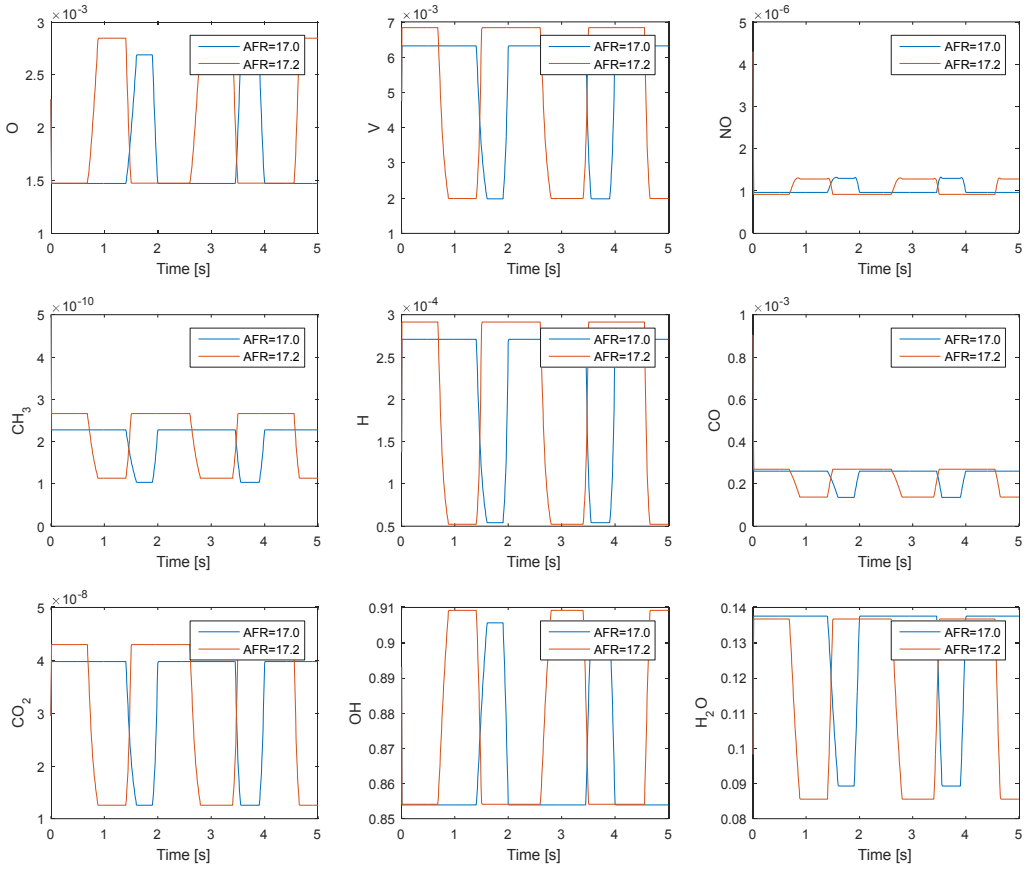

Figure 3-10. Comparison of calculated average surface coverage on catalyst surface as a function of time between AFR 17.0 and AFR 17.2.

The calculated surface coverage in each tank are averaged and compared between AFR 17.0 and AFR 17.2 in Figure 3-10. $OH*$ and H_2O* are the dominant species on the catalyst surface for both conditions because the H_2O concentration is about 19 % in the exhaust mixture. It is also interesting to notice that even though the water inlet concentrations do not fluctuate with time, the OH and H_2O surface coverages show a fluctuating pattern. A simple explanation is that the fluctuations of the other inlet species change the surface species coverage, such as $O*$, $CO*$, $NO*$, $H*$ and vacant sites, which finally impacts the OH and H_2O surface coverages. For oxygen, the surface coverage fluctuation is consistent with the inlet O_2 concentration profile shown in Figure 3-2: a higher O_2 concentration in the gas phase corresponds to a higher oxygen surface coverage at the same time, which explains why the oxygen surface coverage is higher in the fuel lean conditions. Similar trends can be found in NO surface coverage.

`

3.4.3. Simulated dithering with different frequency

To study how the dithering frequency impacts the exhaust conversion in TWC, the exhaust gas composition at AFR 17.1 was chosen for study. The frequency of the exhaust gas flow into the TWC was increased, while all concentrations were kept the same as for the previous simulations. Figure 3-11 compares the gas conversions for two dithering cycles. The gas conversion did not show a noticeable change as the frequency increases. The possible reason is amplitude of the gas concentration were not changed in this calculation, so the conversion are the same except for the transition section. Since the transition time is a small portion in the two cycles, it is not surprising to see that conversions did not change as the frequency increases. Our results differ from Shi and coworkers who studied the natural gas engine emission conversion from frequency 0.02 to 0.5 Hz with λ value 0.99 and amplitude 0.01 and found the THC, NO and CO conversion maximized at frequency 0.1 Hz.

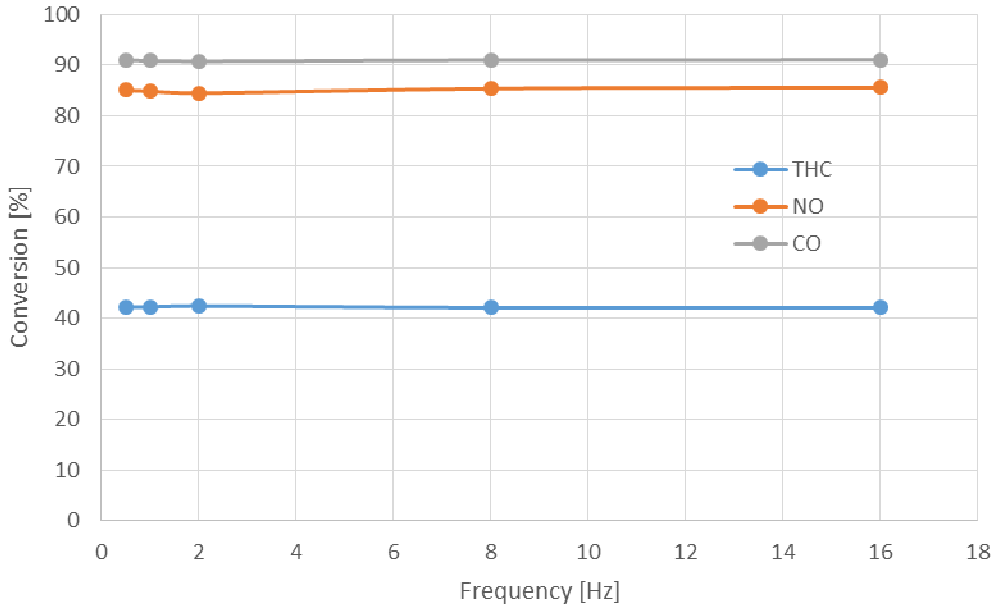

Figure 3-11. Gas conversion in dithering condition with varying dithering frequency.

3.4.4. Simulated dithering with different amplitude

To study how the dithering amplitude impacts the exhaust conversion in TWC, the exhaust gas composition at AFR 17.1 was chosen for study. Our approach was to simply increase or decrease the exhaust gas concentration by some factor for each time point. The excursion time for fuel-lean and fuel-rich conditions was kept constant at the values measured for a frequency of

`

0.5 Hz. For example, the THC and CO concentration are increased in the 0-0.8 s (Figure 3-2) section while the NO, O_2 and CO_2 concentration are decreased; in the next excursion time (1.0-1.5 s), the THC and CO concentration are decreased while NO, O_2 and CO_2 concentration are increased. The same modifications are applied to each subsequent cycle.

Widening the range of AFR ratio during dithering will substantially change the composition going into the TWC. As shown in Figure 3-3, the main effect of changing the nominal AFR ratio during dithering was to change the relative amounts of time spent at high and low AFR. For example, changing to higher nominal AFR ratios resulted in higher amounts of time spent at higher AFR. For this reason, increasing the amplitude will change the effective λ entering the TWC. The inlet gas λ was calculated using the time-averaged mole fraction of each exhaust gas constituent [70] and is shown in Figure 3-12. As seen in this figure, the average λ decreases as the amplitude increases.

$$\lambda = \frac{2x_{CO_2} + x_{CO} + 2x_{O_2} + x_{NO} + x_{H_2O}}{2x_{CO_2} + 2x_{CO} + x_{H_2} + \left(2\alpha + \frac{\beta}{2}\right)x_{C_\alpha H_\beta} + x_{H_2O}} \qquad (11)$$

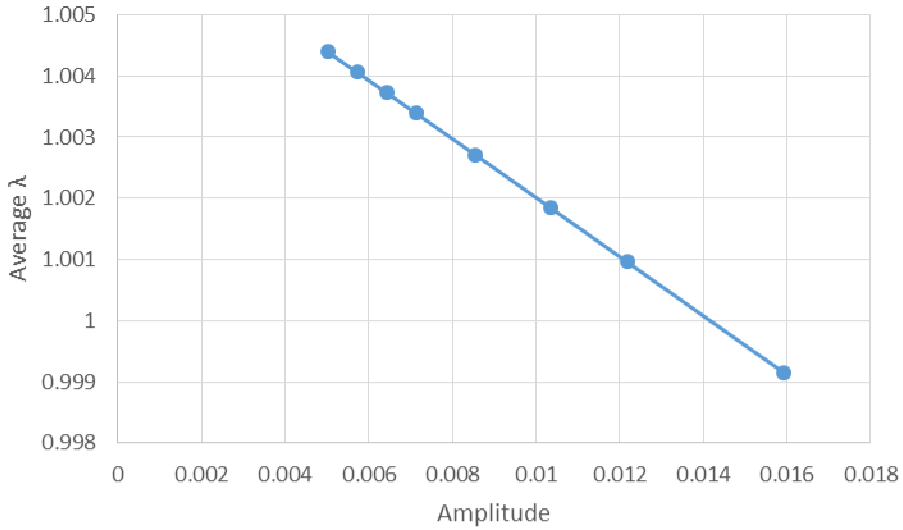

Figure 3-12. Calculated inlet gas average λ as a function of dithering amplitude.

Figure 3-13 shows the simulated gas conversions of THC, CO, and NO with varying dithering amplitude and also the simulated results of steady state at AFR 17.1. Conversions of all species increased as dithering was implemented, but increasing the dithering amplitude decreases

`

those conversions. As the amplitude increases, the THC conversion decreases from 42% to 36 % and the CO conversion decreases since the exhaust gas AFR shifts to the fuel rich side as the dithering amplitude increases. This is consistent with the fact that THC and CO had a lower conversion under fuel rich conditions. The NO conversion slightly decreases as amplitude increases. The possible reason is that even though the NO conversion was high at fuel rich conditions and the fuel rich excursion time is longer, the inlet NO concentration was reduced, so the contribution to the overall NO conversion is not prominent. At the fuel lean condition, the NO conversion was lower plus the inlet concentration increased. Combining the trends in fuel rich and lean conditions, the overall NO conversion slightly decreases. Shi and coworker also studied the dithering amplitude impact on the emission conversion and found 0.01 amplitude is the optimal dithering amplitude. When the amplitude is further increased, the THC and CO conversion decreased while the NO conversion was still high, the possible reason was the higher amplitude resulted in an emission level similar to the steady state at fuel rich [6]. The results in Figure 3-12 is consistent with their hypothesis.

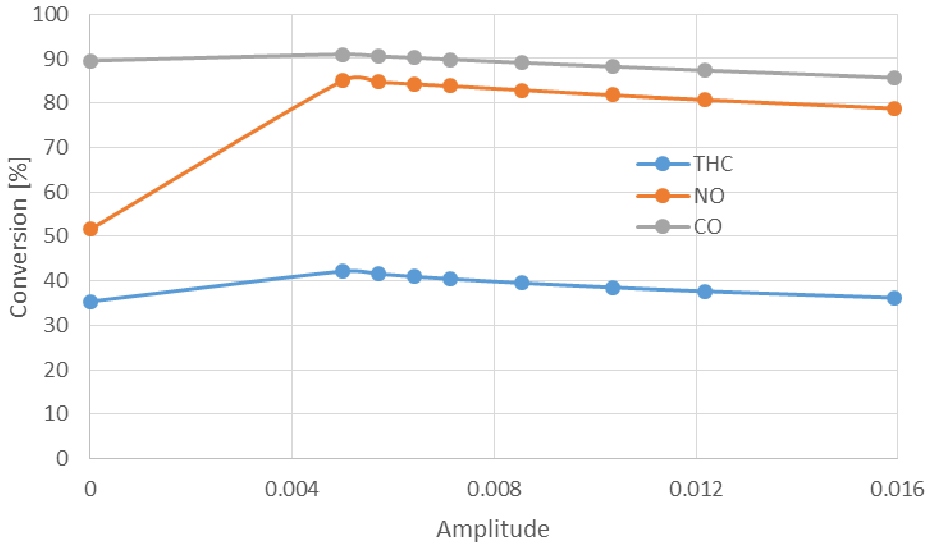

Figure 3-13. Simulated gas conversion in dithering condition with varying dithering amplitude.

3.4.5. Dithering and steady state comparison

Calculations were done to predict the steady state performance of the TWC. In the steady state simulations, the same mathematical model applied to dithering is utilized with a 5 seconds

`

calculation time to reach steady state (time when gas concentration is not changing). Figure 3-14 compares the simulations and experimental results at steady state. The figure shows that simulation can generally capture the experimental trends. In the lower AFR region, the simulation fits well with the experimental results of THC and NO. As the AFR increases, the conversion of THC and NO are underestimated. CO conversion fits reasonably well with a maximum conversion at AFR 17.02, while it is overestimated at AFR 16.8. It is interesting to note that in the plots of THC conversion in Figure 3-14, the experimental and simulation conversions both display a maximum at a specific AFR (although which AFR gives that maximum is different: 17.1 for the experiments and 17.0 for the simulations). The possible reason was that the methane conversion was low at fuel rich condition due to insufficient oxygen, while the methane conversion was low in fuel lean conditions due to water inhibition. This inhibition was not seen in the fuel rich conditions [65].

To examine why there is a maximum in THC conversion around 17.0, the average net THC consumption rate in the 1st tank in steady state conditions is plotted in Figure 3-15. This plot shows that the THC consumption rate is a maximum at AFR 17.0 and has a relatively high value at AFR 17.02.

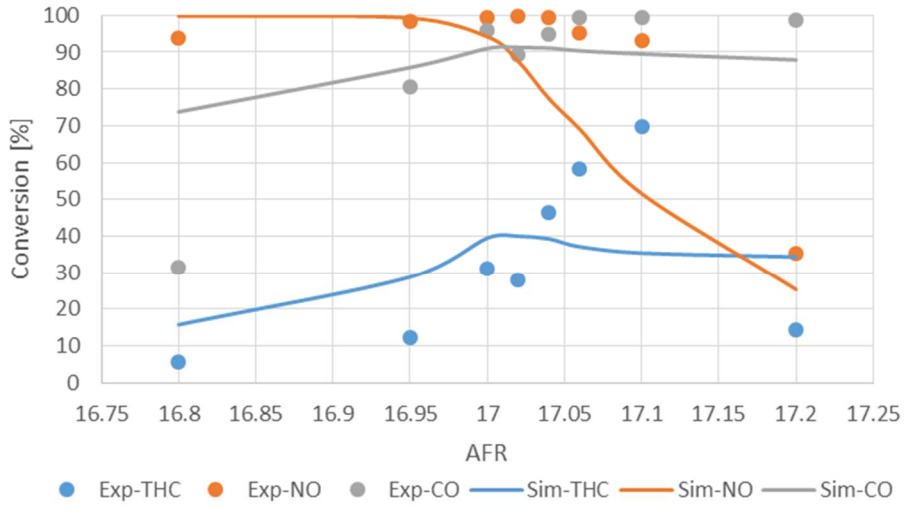

Figure 3-14. Simulation of exhaust conversion in the TWC in steady state conditions. Symbols are the experimental data and lines are the simulation.

`

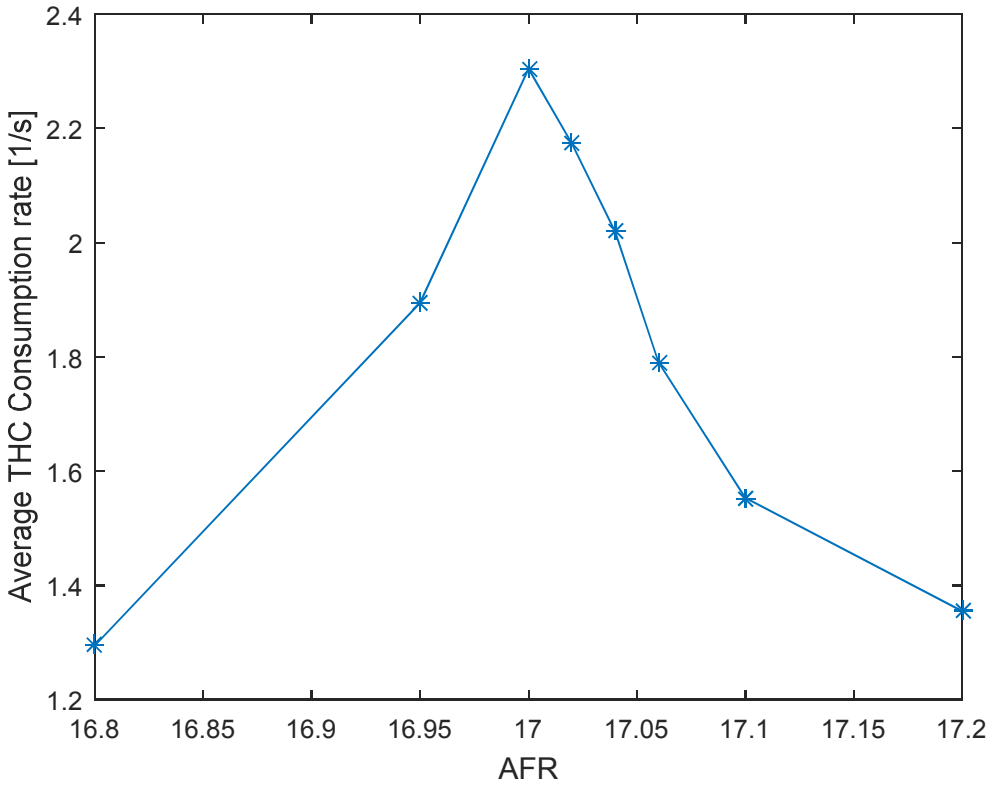

Figure 3-15. Average THC consumption rate in the 1st tank.

Figure 3-16 compares the experimental results for operation under steady state and dithering conditions. The THC maximum conversion shifts to a higher AFR in the dithering conditions, while the general trends are similar. The CO conversions are close for both operation conditions, while dithering shows a higher NO conversion at fuel lean conditions.

`

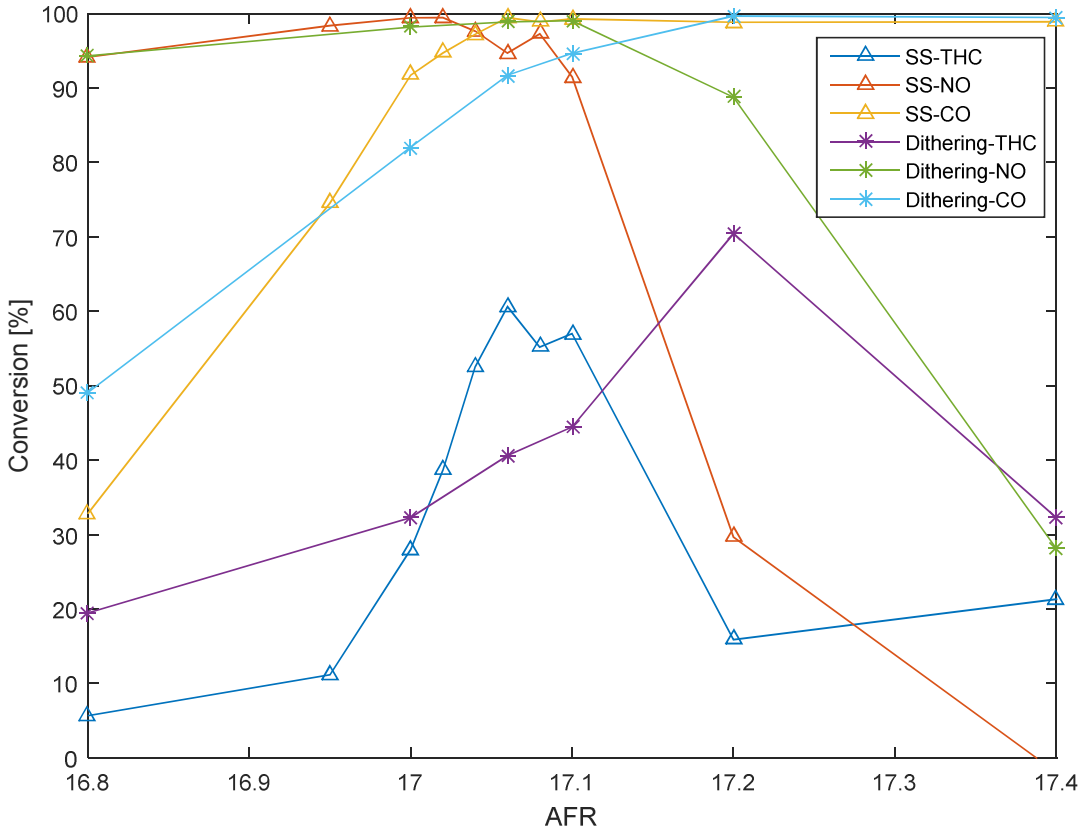

Figure 3-16. Comparison experimental results of TWC window between the steady state (SS) and dithering conditions.

Figure 3-17 shows the calculated results for steady state and dithering conditions. For all three species, the dithering has a higher gas conversion compared to the steady state at the same AFR. It is also interesting to note that the NO conversion remains above 80% in dithering while for the steady state simulations it decreases quickly as the AFR increases. The difference in NO conversion between the steady state and dithering conditions are consistent with the experimental results shown in Figure 3-16. Figure 3-18 shows the NO net consumption rate in the first tank and indicates that NO consumption rate in dithering condition is higher than that in the steady state, especially at higher AFR, which explains that in the AFR 17.0-17.2, the NO conversion is higher than that in the steady state.

`

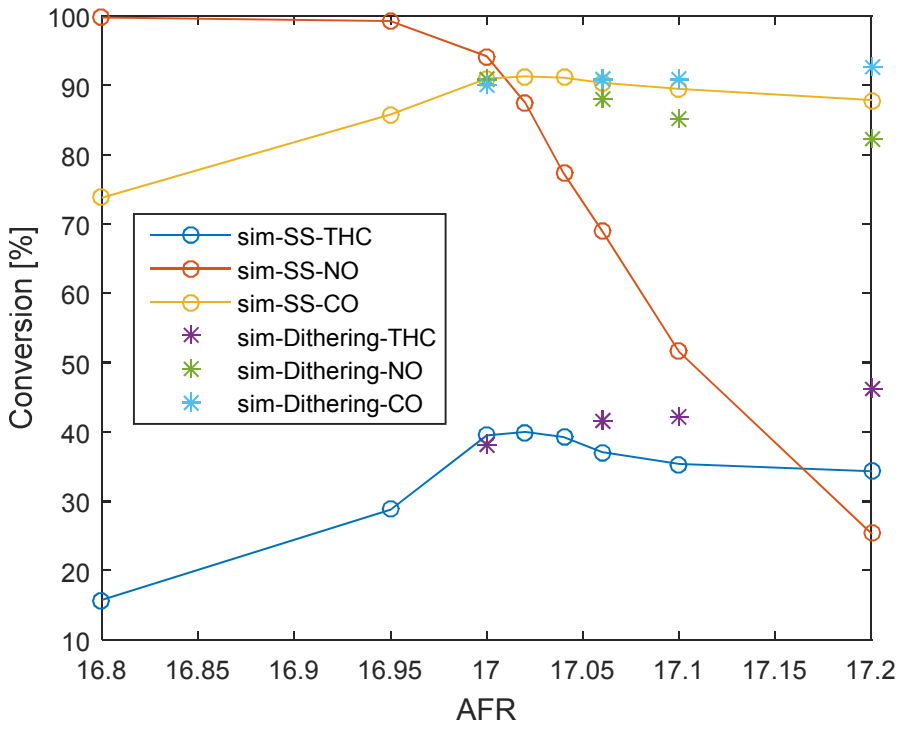

Figure 3-17. Comparison calculated TWC window between the steady state and dithering conditions (SS=steady state condition).

`

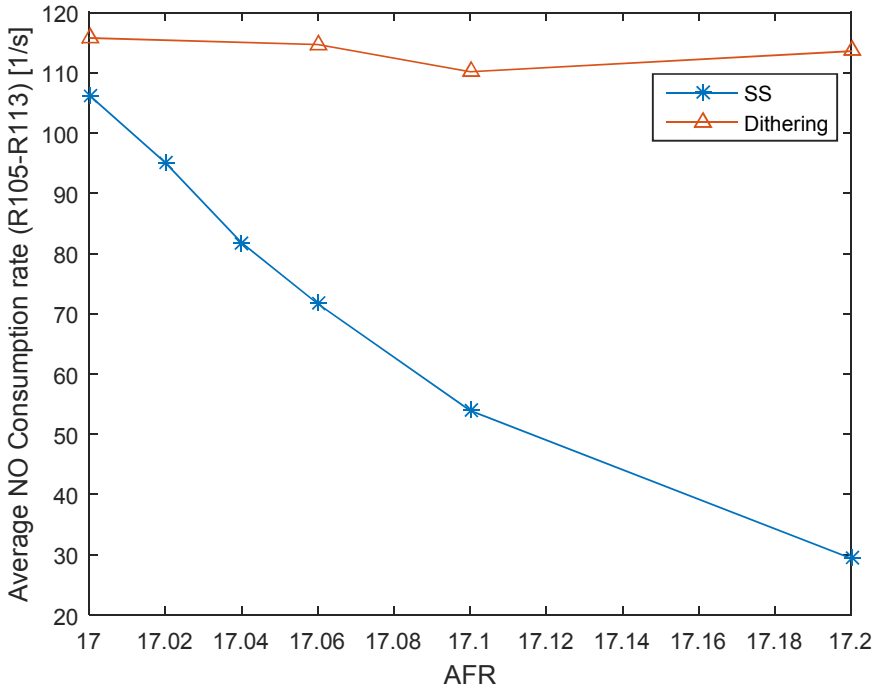

Figure 3-18. Average NO consumption rate in the 1st tank.

`

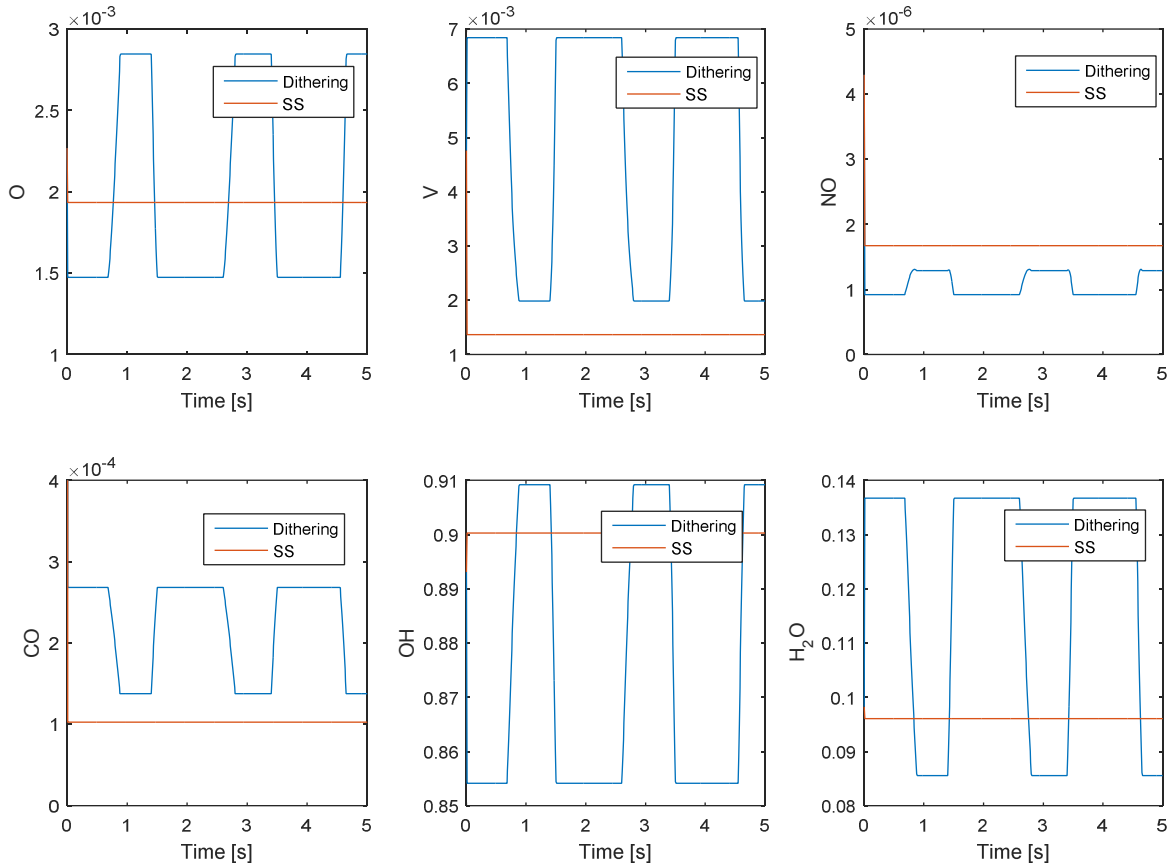

Figure 3-19. Comparison calculated surface coverage on catalyst surface between dithering and steady state conditions at AFR 17.2.

To further understand why the NO consumption rate differs in dithering and steady state conditions, Figure 3-19 compares the surface coverages for both conditions at AFR 17.2. In the steady state, the CO surface coverage is lower than that in the dithering conditions while the O, OH and H_2O surface coverage is in between. NO surface coverage is higher in the steady state. However, the most important difference that causes higher conversion of NO under dithering conditions is the concentration of vacancies: the coverage of vacant sites (V) is much higher in the dithering condition than the steady state. This explains why the NO conversion is higher in the dithering condition since more vacant sites will promote the adsorption of NO and also reaction R108 ($NO_* + * \rightarrow N_* + O_*$) leads to a higher NO consumption rate in dithering as shown in Figure 3-18. It was also noted that the coverage of vacant sites decreased as AFR increased for steady state conditions while it was nearly constant for dithering simulations (not

`

shown). This explains why the results for dithering and steady state simulations of NO conversion are not too different at AFR of 17.0, but diverge as the AFR is increased.

3.5. Conclusion

A detailed and thermodynamically consistent surface reaction mechanism capable of modelling all the key reactions in a three-way catalyst was applied to treat exhaust from a natural-gas engine under dithering conditions. By adjusting five of the 115 reaction steps, the model was able to predict the post catalyst THC, NO, and CO concentration generally well. The simulated surface coverage indicated that OH_* and H_2O_* were the dominant species on the surface because water concentration was large in the exhaust mixture. The CO and THC conversion increased as the O_2 concentration increased, while NO conversion also decreased since NO_* dissociation (R108 $NO_* + * \rightarrow N_* + O_*$) was inhibited by excessive oxygen on the catalyst surface. Simulation of dithering with different frequencies and amplitude indicated that frequency does not have a noticeable impact on the gas conversion while the THC and CO conversion decrease as the dithering amplitude increase since the larger dithering amplitude shifts the AFR to the rich side. The simulation results of both steady state and dithering condition indicated that the NO conversion in the dithering conditions are higher than those in the steady state conditions, in agreement with experimental results. This is due to the higher vacant site coverage present in the dithering conditions.

`

Chapter 4 - Influence of basicity on 1, 3-butadiene formation from catalytic 2, 3-butanediol dehydration over γ-alumina

Abstract

The direct catalytic conversion of 2, 3-butanediol (BDO) to 1, 3-butadiene (BD) was studied over two commercial forms of alumina (denoted as F200 and SCFa) at temperatures between 240 ^{0}C and 450 ^{0}C. Even though these two catalysts are both high surface area forms of γ-alumina, they gave remarkably different results, with SCFa giving higher BD selectivities at all experimental conditions. The difference is attributed to the higher surface area of F200, which means a greater number of acid sites that can convert BDO to methyl ethyl ketone (MEK). NH_3 and CO_2-TPD results supported this conclusion by showing that the two forms of alumina had different acid/base properties. Experimental results also showed that BD selectivity was improved by increasing temperature, residence time and co-feeding water. The residence time study combined with density functional theory (DFT) calculations proved that 3-buten-2-ol (3B2OL) is an important intermediate in the conversion of BDO to BD. BD selectivity decreases over sodium modified alumina SCFa. It is hypothesized that on sodium-modified alumina, 3B2OL is dehydrogenated to form methyl vinyl ketone (MVK) as opposed to dehydration to BD. Basic sites catalyzed the retro-aldol condensation of MVK, which produces acetone and formaldehyde via cleavage of the C=C bond. This is in agreement with DFT calculations showing that the proposed pathway for acetone formation is more energetically favored on Na-modified γ-Al_2O_3 (110) surface compared to the pristine (110) surface.

4.1. Introduction

Nearly 70 years ago, Winfield demonstrated that 2, 3-butanediol (BDO) could be dehydrated over thoria to produce 1, 3-butadiene (BD) for synthetic rubber manufacturing [8]. However, due to the abundance of petroleum resources, BD has been almost exclusively produced from hydrocarbon feeds, such as naphtha [11]. Recently, there has been renewed interest in producing industrial chemicals from biomass resources [71]. In this regard, catalytic BD production from renewable resources is an appealing strategy, which ensures ample supply and reduces price volatility of the final product [9]. Fermentation of biomass-based glucose and

`

xylose by Klebsiella pneumodae yields BDO at high yields [10]. Alternatively, BDO can be produced by nonpathogenic bacteria utilizing industry waste gas [72]. These routes suggest that BDO can be obtained on a large scale economically. This also suggests that the dehydration of BDO to BD may be a plausible route for production of renewable BD.

Dehydration of BDO can readily occur on zeolites [13], and with mineral acids such as sulfuric acid [12]. However, methyl ethyl ketone (MEK), rather than BD, is the dominant product due to the keto-enol tautomerization and pinacol rearrangement. Only a few studies resulting in successful selective production of BD have been reported. Among them, Winfield, who studied the catalytic dehydration of BDO to BD over thoria, reported a single pass conversion of 60% to BD at 500 ^{0}C [8]. Shlechter obtained BD from the esterification of BDO with acetic acid, followed by pyrolysis of the diacetate [15, 16]. BD production started at temperatures above 475 ^{0}C. The optimal condition appeared to be at a temperature of about 585 ^{0}C and contact time of 7.1 seconds, where the BD yield was 84.9 % under such conditions in his study. Recently, BDO dehydration over rare earth metal oxides has been studied and basic sites generated by introducing CaO into ZrO_2 can enhance the 3B2OL selectivity [17-19]. The maximum BD selectivity was 94 % with 100 % BDO conversion on a two-bed catalyst system (Sc_2O_3 +Al_2O_3) [20].

As noted above, the most successful catalysts for BD production have been thoria and scandium oxide, neither of which are commonly used as catalysts. Thoria is a radioactive compound, while scandium oxide is rare and expensive. For this reason, we have been considering catalysts based on alumina to convert BDO to BD. Specifically, we have been studying ways to modify alumina to enhance BD selectivity.

The literature suggests that acid-base properties are important in BDO dehydration. In particular, BD selectivity can be influenced in the presence of alkaline species. For example, cesium doped silica can promote BD selectivity [73]. Kim and Lee reported that BD selectivity increased from 51% to 62% as the Cs_2O/Al_2O_3 mass ratio increased from 11% to 40%. However, other researchers have found that 10 wt% Cs_2O and alkali metal oxides (Na_2O and K_2O) loaded on silica gave 2, 3-epoxybutane as the main product [74]. Díez and coworkers studied the effect of acid/base properties on the product distribution in the dehydration of 1,3-butanediol and concluded that acidic oxides promote 1,3-butanediol dehydration to unsaturated alcohols and basic oxides dehydrogenate-dehydrate the diol to the unsaturated ketone, which further

`

decomposes by retro-aldol condensation, giving C1-C3 alcohols, aldehydes and ketones [75]. All these experiments indicated that the acid/base property of the catalyst had a crucial impact on the product distribution.

Insights on the reaction mechanisms governing the main and side reactions will be valuable to advance BDO dehydration catalysis. To this end, we report a combined experimental/theoretical study on the dehydration of BDO using two commercial forms of alumina. The surface of alumina contains hydroxyl group, Lewis acid sites (aluminum atoms) and basic site (oxygen atoms) [76]. Since both acid and base sites are likely required to produce BD from BDO [77], alumina is attractive as a potential catalyst for BDO dehydration to BD. In this study, BDO dehydration has been carried out over alumina samples where, the acid-base properties are modified by using these two different forms of alumina, by calcining the samples at different temperatures, and by doping alumina with sodium. To complement the experimental studies, DFT calculations were carried out to investigate the energetics and kinetics of key BDO dehydration steps on model **γ**-alumina surfaces, where sodium-doped surface was also introduced for comparison. A consistent experimental/theoretical view was obtained for the main BD formation pathways and relevant competing reactions, and the catalytic routes for considered catalysts were proposed based on the experimental and DFT results.

4.2. Experimental

4.2.1. Catalyst preparation

SCFa and F200 were obtained from Sasol and BASF, respectively. The catalyst pellets were crushed and sieved to >60 mesh before use. The compositions of the alumina samples as supplied by manufacturers are listed in Table 4-1.

Table 4-1. Comparison of compositions of SCFa and F200

Composition and chemical/physical properties	SCFa	F200
Al_2O_3 [%]	98	92.7
Na_2O [%]	0.002	0.3
SiO_2 [%]	0	0.02
Fe_2O_3 [%]	0	0.02
L.O.I (loss on ignition)[%]	2	7

`

Sodium is present in most commercial alumina at approximately 0.3-1.5 wt% Na_2O. F200 is typical of aluminas derived from the Bayer process which are typically low in cost. Water and acid washing steps are sometimes employed to lower the sodium content in aluminas formed via the Bayer process. SCFa is a higher-purity alumina derived from the Ziegler process for the manufacture of linear fatty-alcohols, which uses an alkyl aluminum catalyst. In the Ziegler process, ethylene is oligomerized by the aluminum catalyst followed by oxidation to form an aluminum trialkoxide, which upon hydrolysis gives rise to the fatty-alcohol products and boehmite. After boehmite calcination, very high-purity gamma-alumina is obtained, which have less than 20 ppm sodium content.

To understand the role of sodium in the BDO dehydration, SCFa was impregnated with different amounts of sodium. Samples with different amounts of Na_2O were prepared by dissolving $NaNO_3$ in deionized water and placing SCFa powder in the resulting solution. 0.041 g $NaNO_3$ was loaded onto 3.75 g of SCFa to prepare a sample containing 0.3% Na_2O (mimicking the amount of sodium in F200), while 0.85 g $NaNO_3$ was loaded onto 3.75 g SCFa to determine the impact of high levels of sodium on catalyst performance. The samples were dried at 120 ^{0}C in an oven for 12 hours and finally calcined at 600 ^{0}C for 6 hours.

The impact of calcination catalyst was also studied because calcination will affect both acid/base properties and physical properties of the catalysts. Calcination is particularly of interest for this study since F200 has a much higher surface area than SCFa, so calcination could convert F200 to a form more similar to SCFa in terms of surface area and acid/base site density. SCFa and F200 calcined in the air at 400 ^{0}C, 600 ^{0}C, 1000 ^{0}C and 1100 ^{0}C for 24, 24, 5 and 24 hours, respectively, are denoted as SCFa-X and F200-X, where X is the calcination temperature.

4.2.2. Catalytic reaction

The dehydration of BDO was carried out in a fixed-bed Hastelloy® tube reactor of 0.305” inner diameter. Since Hastelloy is a potential catalyst, blank tests were performed in an empty tube with the same conditions as the actual catalytic activity tests. For all catalyst activity experiments, 0.5 g of catalyst was placed in the reactor between two plugs of quartz wool. Liquid phase BDO (2g/100 mL) aqueous solution was fed at a flowrate of 0.1 mL/min through a micro pump (Eldex) to the top of the reactor through a nebulizer, where it was mixed with 100 mL/min of N_2 (regulated by a Brooks 5850E mass flow controller), which is used as an internal standard

`

for product analysis. The approximate residence time is 0.14 s. The reactor was heated by heating tape. The temperature was measured by a K-type thermocouple, and a controller was used to ensure that temperature was held constant at the desired value.

Product analysis was carried out on-line by a SRI 8610C gas chromatograph using TCD and FID detectors. The gas chromatograph was equipped with molecular sieve (to separate N_2 from organic products) and MXT-1 columns (60 m, ID 0.53 mm). The oven temperature was held at 40 ^{0}C for five minutes, then raised to 230 ^{0}C at a rate of 40 ^{0}C/minute, and the temperature remained constant for 15 minutes. Argon gas was used as the carrier gas. The following compounds were identified using the gas chromatograph: BD, acetone, 2-methylpropanal (MPA), 3-buten-2-ol (3B2OL), MEK and isobutanol. In addition to the above species, heavy products were detected. Their response factor was assumed to be the same as BDO, and their total amount is lumped together as "heavy species". Condensed species were characterized using GC-MS (Shimadzu GCMS-QP2010 SE). Species identified include 2-methyl-2-cyclopenten-1-one, 3,4-dimethyl-2-cyclopenten-1-one, 3,4,4-trimethyl-2-cyclopenten-1-one, 2-methyl-phenol, 3,4-dimethylphenol and 2,4-dimethylphenol.

Each experimental condition was repeated at least three times for each condition. All mass balances closed within 20 %, with most closing within 10%.

The conversion of BDO and selectivity of the main products were calculated as below:

2, 3-butanediol conversion=$\frac{mole_{BDO,in}-mole_{BDO,out}}{mole_{BDO,in}} * 100\%$ (1)

Selectivity=$\frac{mole_{i,out}}{mole_{products}} * 100\%$ (2)

where mole $_{products}$ means the moles of products of reaction, including MEK, MPA, BD and heavy products. The BDO conversion was 100% except where stated.

4.2.3. Catalyst characterization

4.2.3.1. XRD

X-ray diffraction measurements were performed on the catalyst powders with a Rigaku MiniFlex II desktop X-ray diffractometer with Cu Kα radiation (λ=0.15406 nm) in an operation mode of 30 kV and 15 mA. Data were collected from 10^0 to 80^0 with a scanning rate of 1^0/min. Crystallite sizes of γ-alumina were calculated using the Scherrer formula:

$$d=0.9\lambda/\beta \cos\theta \quad (3)$$

`

where λ=0.15406 nm, β is the full width at half-maximum (FWHM) in radians of the γ-alumina peak centered at $2\theta=67^0$, and θ is the Bragg angle.

4.2.3.2. TPD

Temperature programmed desorption of ammonia (NH_3-TPD) was performed on an AMI-200. 200 mg of sample was treated under Helium for 4 hours at 600 ^{0}C. Next, 1% ammonia balanced in Helium was flowed over the catalyst for 2 hours. After saturation with ammonia, the sample was flushed in a He flow at 120 ^{0}C for 1 hour to remove physically adsorbed ammonia. The temperature was then raised to 600 ^{0}C at a heating rate of 5 ^{0}C/min. The amount of ammonia desorption from the sample was measured by a thermal conductivity detector. The peak area was converted to moles of gas by using a calibration file created for the species of interest. CO_2-TPD was performed using the same procedure with 10% CO_2 in Helium as the adsorbate.

4.2.3.3. N_2 adsorption-desorption

N_2 adsorption-desorption analyses were carried out using Quanta Chrome Autosorb-1 instrument. The surface area was calculated by the BET method with P/P_0=0.05-0.3. The total pore volume, average pore radius and pore size distribution were calculated by the BJH method with the desorption branch of nitrogen isotherm. The samples were degassed under vacuum at 573 K for 4 h prior to adsorption analysis.

4.2.3.4. Density Functional Theory (DFT)

All DFT calculations were performed using the Vienna Ab initio Simulation Package (VASP) code [78]. The GGA-PBE functional was used to account for the electron exchange-correlation effects [79]. The projector augmented wave (PAW) method was used to treat the ion-electron interactions [80]. The energy cutoff for the plane wave-based wave function was 380 eV. For the periodically bounded slabs, the first Brillouin zone was sampled using a 2×2×1 k-point mesh based on the Monkhorst-Pack scheme [81]. A higher number of k-points (i.e. 4×4×1) were also used and it was found that the total energy has converged to within 50 meV. The break condition for self-consistent iteration is 1×10^{-6}. Ionic relaxation is stopped when the forces on all atoms are smaller than -0.05 eV/Å. All the initial structures of the molecular models were created using the Materials Studio Visualizer. A vacuum equivalent to 4 layers of the slab was used with the bottom two layers of the slab fixed at its bulk value. Dipole corrections along the

`

direction perpendicular to the surface were used to decouple the electrostatic interaction between periodic images.

The energies and geometries of the gas phase species were calculated by placing the molecule in a box with dimensions of 20 × 20 × 25 Å. A Γ-point k point was used for these calculations. Gaussian smearing was used to assist convergence. All the calculations were non-spin polarized (except for the gas phase species with unpaired electrons).
Transition states (TS) and energy barriers were calculated using the climbing-image Nudged Elastic Band (CI-NEB) method [82], coupled with the dimer method [83]. For the NEB calculations, seven images were used. The dimer method was then used to further refine the preliminary TS structures. Each TS was confirmed to have only one imaginary vibrational mode. Finally, the total energies are also corrected with Grimme's DFT-D3 method for the dispersion interactions between adsorbate molecules and surface [84].

4.3. Results and discussion

4.3.1. Characterization

Figure 4-1-a and Figure 4-1-b shows the XRD patterns of alumina samples SCFa and F200, respectively. As can be seen in this figure, spectra of unmodified SCFa mainly correspond to γ-Al_2O_3 (JCPDS 10-0425) with the dominant peaks detected at 45.65 and 67.14 degrees. For F200, peaks detected at 37.82 and 67.49 degrees were attributed to γ-Al_2O_3. F200 displays fewer peaks and lower peak intensities as compared to SCFa because is it a less crystalline, higher surface area form. SCFa and F200 calcined at lower temperature such as 400 ^{0}C, 600 ^{0}C and 1000 ^{0}C did not have a noticeable phase change, but as the temperature increased to 1100 ^{0}C, SCFa-1100 was converted to the α phase of alumina (JCPDS 42-1468) with peaks detected at 25.49, 35.05, 43.25, 52.43, 57.37, 66.38 and 68.08 degrees. It is easy to see that calcination leads to an increased number of peaks and increasing peak intensity for F200 similar in both peak distribution and intensity to SCFa at 1100 ^{0}C. In Figure 4-1-a, no obvious difference in the XRD pattern is noted after 0.03% Na was loaded onto SCFa. However, as the Na_2O loading increased to 7.6%, diffraction peaks attributed to sodium and support interactions were observed at 2θ=18.28 and 20.28. These can be assigned to sodium aluminum oxide ($Al_2Na_2O_4$) [85]. These two peaks are not observed in the Na_2O XRD pattern, obtained as a reference by calcination of $NaNO_3$ at 600 ^{0}C for 6 hours.

`

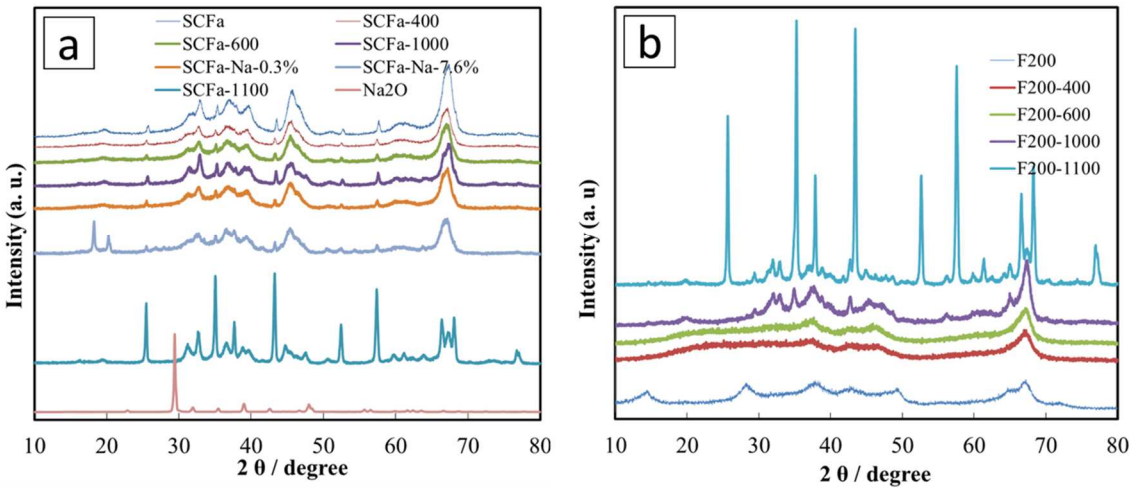

Figure 4-1. XRD patterns of alumina SCFa samples (a); and XRD patterns of alumina F200 samples (b).

To explore the differences in acid-base properties between calcined SCFa samples and calcined F200 samples, NH_3 and CO_2 TPD experiments were performed. Figure 4-2 shows the NH_3-TPD performed on both calcined SCFa and F200 samples while CO_2-TPD is shown in Figure 4-3. The total acidity and basicity in terms of moles of each gas adsorbed are tabulated in Table 4-2.As seen in Figure 4-2, the broad NH_3 desorption peak over SCFa extends from 120 to 500 ^{0}C. For F200, there is a sharp peak at 200 ^{0}C with a broad shoulder extending out to 500 ^{0}C. For both SCFa and F200 samples, the acid site density decreases as the calcination temperature increases. Figure 4-3 shows the CO_2-TPD of the SCFa and F200 samples. In general, all spectra show a primary peak around 200 ^{0}C with a long tail that extends to higher temperatures. At high temperature region, SCFa exhibits a large desorption peak at 400 ^{0}C while this peak disappears in sample SCFa-400 and SCFa-600. SCFa-1000 and SCFa-1100 both exhibit a CO_2 desorption peak at high temperature, but they both shift to lower temperature. Each F200 sample exhibits a small CO_2 desorption peak at high temperature region, while it is hardly seen in sample F200-1100. The CO_2-TPD data indicate that the base site density of both SCFa and F200 decrease as the calcination temperature increases.

`

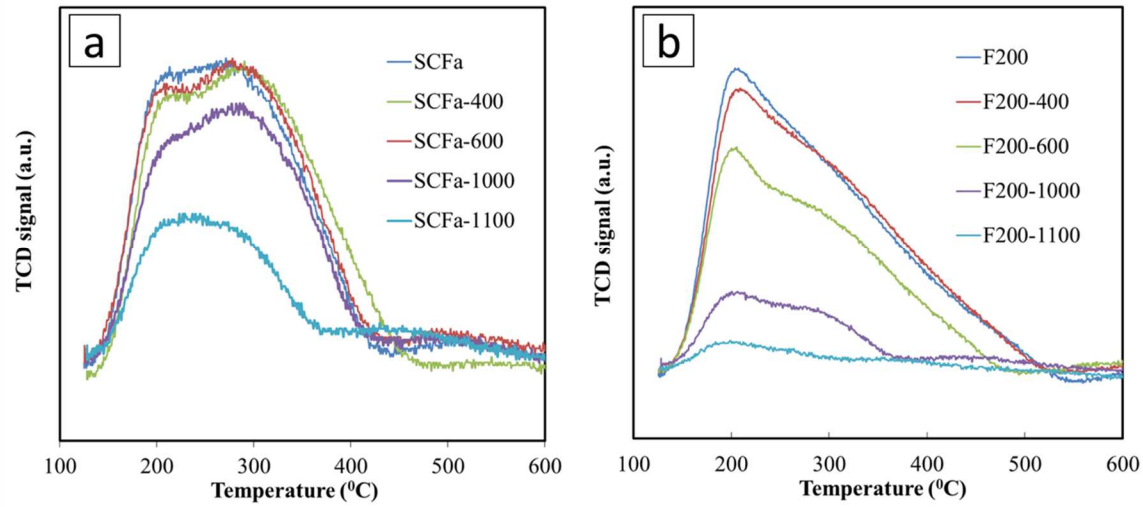

Figure 4-2. NH_3-TPD of SCFa samples (a); and F200 samples (b).

The calculated acid site density (Acidity/BET surface area) of SCFa and F200 are 1.8 and 1.6 μmol/m^2 respectively. For comparison, Flego and coworker [86] reported an alumina acid site density of 1.8 μmol/m^2 by NH_3-TPD while Colorio [87] and Curtin [88] reported acid site densities of 1.6 and 1.9 μmol/m^2 respectively. The calculated base site density (Basicity/BET surface area) of SCFa and F200 are 0.45 and 0.37 μmol/m^2 respectively, this is consistent with the γ-Al_2O_3 base site density 0.48 μmol/m^2 reported by Seki [89]. However, others report much small base site densities of 0.12 μmol/m^2 for γ-Al_2O_3 [90].

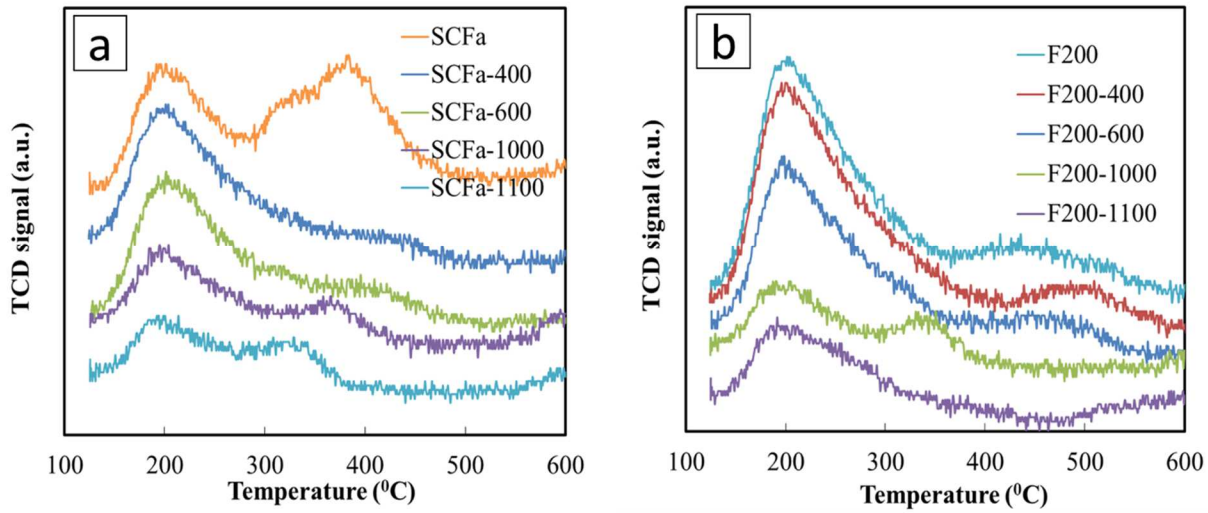

Figure 4-3. CO_2-TPD of SCFa samples (a); and F200 samples (b).

`

To study the effect of sodium on the density of base sites on alumina, CO_2-TPD was performed on SCFa, Na-modified SCFa and F200. The results are shown in Figure 4-4. All four samples exhibit a CO_2 desorption peak at 200 ^{0}C. Only SCFa exhibits a second desorption peak from 300 to 500 ^{0}C. The addition of 0.3% sodium to SCFa only slightly modifies the TPD profile, increasing the low-temperature peak while decreasing the peak area in the middle region. Addition of 7.6% sodium dramatically increases the peak area in the low-temperature region, while there is no discernible peak in the middle region. Clearly, sodium increases the number of weakly basic sites, but appears to lower the number of sites with medium base strengths. To investigate this further, SCFa was calcined at 600 ^{0}C for 6 hours (labeled as "SCFa comparison") as a reference and characterized with CO_2-TPD. The results showed that the high temperature CO_2 desorption peak was also not present in the calcined sample, while basic site densities in other regions were close to SCFa. This suggests that the second CO_2 desorption peak in SCFa was removed by the calcination step when sodium was added, and not from sodium modification.

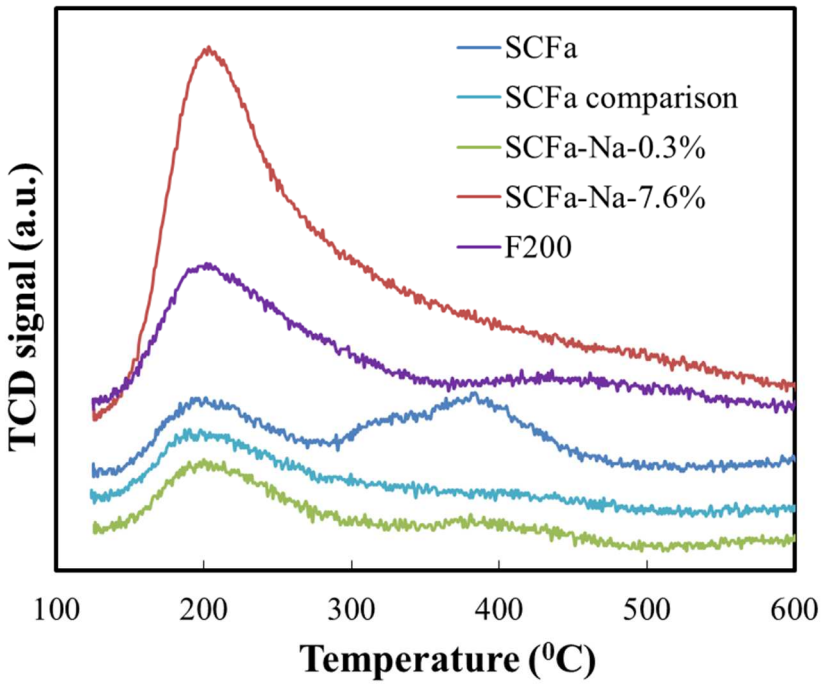

Figure 4-4. CO_2-TPD of sodium contained alumina.

`

The nitrogen adsorption isotherm for calcined SCFa are shown in Figure 4-5-a. All of them exhibit a type IV isotherm (defined by IUPAC) which is characteristic of mesoporous material. SCFa has a H1 hysteresis loop, indicating that SCFa has a cylindrical pore structure. At low pressure, the smooth adsorption indicates that few micropores exist in SCFa. As the calcination temperature increases, the hysteresis moves toward to higher relative pressure due to the agglomeration of alumina particles. Figure 4-6-a shows a type IV isotherm for F200, which relates to a mesoporous structure. The sample also has some micropores, as indicated by adsorption at low relative pressure. F200 has a H2 hysteresis loop which indicates that the ink-bottle pore may be present in the mesoporous alumina [91]. As the calcination temperature increases, the adsorption at low relative pressure disappears and the hysteresis loop moves toward higher relative pressure values, indicating that capillary condensation occurs in larger mesoporous. F200 calcined at 1000 and 1100 ^{0}C exhibits a H3 hysteresis loop, indicating slit-like pores [92].

The pore size distributions shown in Figure 4-5-b and Figure 4-6-b indicate that as the calcination temperature increases, the SCFa and F200 pore size distribution broadens. The pore size of SCFa series are narrowly distributed between 5-17 nm while SCFa calcined at 1000 ^{0}C and 1100 ^{0}C had a broad pore size distribution which ranges from 6-30 nm. F200 alumina has a narrow pore size distribution around 3.84 nm. As the calcination temperature increases, the pore size distribution widens and F200 calcined at 1000 and 1100 ^{0}C exhibits an even wider pore size distribution. This can be explained by noting that mesopores in the alumina will be collapsed during the long duration calcination at high temperature. These results are consistent with the differences in SCFa and F200 isotherms shown in Figure 4-5-a and Figure 4-6-a.

`

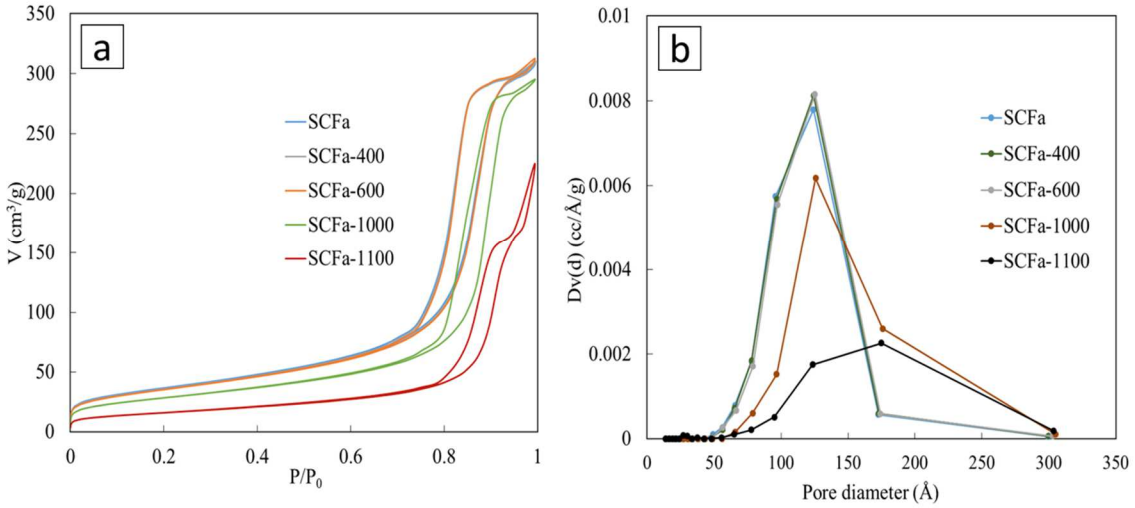

Figure 4-5. N_2 adsorption/desorption isotherms of alumina SCFa and SCFa calcined at 400, 600, 1000 and 1100 ^{0}C (a) and the corresponding pore diameter distribution (b).

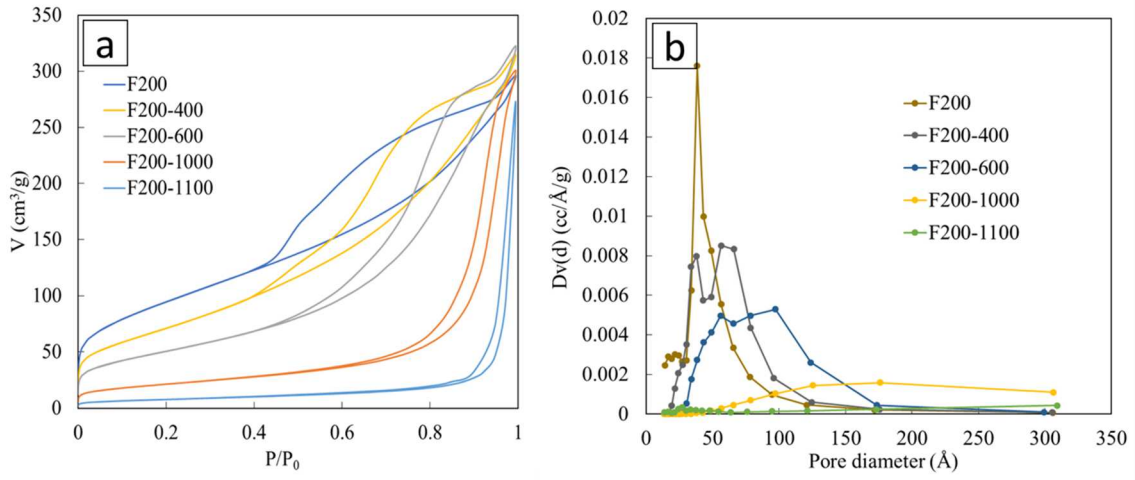

Figure 4-6. N_2 adsorption/desorption isotherms of alumina F200 calcined at 400, 600, 1000 and 1100 ^{0}C (a) and the corresponding pore diameter distribution (b).

Figure 4-7-a shows that as the sodium loading in SCFa increased, the H1 hysteresis also moves toward to higher relative pressure due to particles agglomeration, similar to what happened as the calcination temperature increased. The XRD suggested that Na atoms are intercalated with Al_2O_3 during the calcination process. However, the sodium content in SCFa did not modify the SCFa H1 hysteresis loop to a H3 hysteresis loop as seen for F200. Figure 4-7-b shows that the pore size distribution slightly narrowed as the sodium content increases to 7.6%. Again, sodium did not change the SCFa pore size distribution to a distribution more like F200.

`

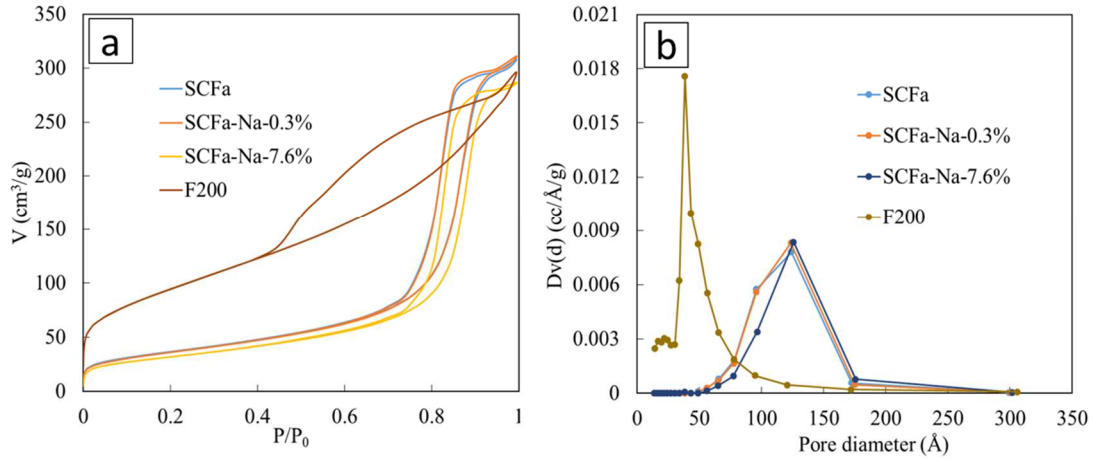

Figure 4-7. N_2 adsorption/desorption isotherms of sodium contained alumina (a) and the corresponding pore diameter distribution (b).

Table 4-2 summarizes the physical properties of alumina SCFa and F200 including the total pore volume, BET surface area and the average pore radius and crystallite size. The specific surface area decreases as the calcination temperature increases due to agglomeration. The increase in average pore size with calcination time can be explained by the growth of crystallites as the calcination time increases, which can be seen in the XRD results. The total pore volume of both SCFa and F200 initially increases as the calcination temperature increases to 600 ^{0}C but further decreases when the calcination increases from 600 to 1100 ^{0}C because larger crystallites occupy more space [93]. For the sodium modified SCFa, the BET surface decreases and the average pore radius increases as the sodium loading increases. The crystallite size of γ-alumina was calculated from Scherrer equation. The crystallite size generally increase as the calcination temperature increase.

Table 4-2. Physical properties and acid/base site density of calcined SCFa and F200.

	Total pore volume (cc/g)	BET surface area (m^2/g)	Average Pore Radius (Å)	Acidity (mmol/g)	Basicity (mmol/g)	Crystallite size (nm)
SCFa	0.461	131.0	70.3	0.24	0.059	5.6
SCFa-400 24h	0.461	128.6	71.8	0.23	0.051	6.2
SCFa-600 24h	0.463	126.8	73.1	0.21	0.038	6.0
SCFa-1000 5h	0.441	101.8	86.6	0.19	0.023	6.3
SCFa-1100 24h	0.262	57.4	91.3	0.10	0.017	10.4

`

F200	0.430	341.0	25.2	0.55	0.127	2.5
F200-400 24h	0.453	264.9	34.2	0.50	0.117	4.0
F200-600 24h	0.459	184.6	49.8	0.37	0.072	4.1
F200-1000 5h	0.409	77.1	106.2	0.09	0.034	7.0
F200-1100 24h	0.125	28.0	89.0	0.04	0.033	9.8

Table 4-3. Physical properties and base site density of sodium contained alumina

	Total pore volume (cc/g)	BET surface area(m^2/g)	Average Pore Radius (Å)	Basicity (mmol/g)
SCFa	0.461	131.0	70.3	0.059
SCFa-Na-0.3%	0.464	129.7	71.5	0.059
SCFa-Na-7.6%	0.434	114.0	76.2	0.322
F200	0.430	341.0	25.2	0.127

4.3.2. BDO dehydration over SCFa and F200

The product distributions from the reaction of BDO over SCFa and F200 are summarized in Table 4-4. It is easy to see that SCFa had a higher activity than F200 comparing the BDO conversion at 240 ^{0}C. Figure 4-8 shows the species distributions for the main product in Table 4-4.

Table 4-4. Dehydration of BDO over different alumina samples at different temperatures.

Sample	T (^{0}C)	Conversion (%)	Selectivity[b] (mol. %)									
			1	2	3	4	5	6	7	8	9	10
	300	0.0	0	0	0	0	0	0	0	0	0	0
Blank test	350	3.5	0	0	0	0	0	18.4	0	81.6	0	0
	400	34.2	6.2	0	0	0	0	19.9	4.4	69.5	0	0
	240	31.7	4.8	0.0	0.0	0.0	0.0	4.0	3.6	83.1	1.2	3.3
	300	100.0	3.4	15.2	0.0	0.0	0.0	7.3	0.0	72.8	1.4	0.0
SCFa	350	100.0	2.3	22.6	0.0	0.0	0.0	9.9	0.0	64.4	0.0	0.8
	400	100.0	0.0	24.7	0.0	0.0	1.9	8.1	0.0	57.7	0.0	7.5
	450	100.0	1.4	28.0	0.0	0.4	1.5	3.3	0.0	56.9	0.0	8.4
	240	3.8	0.0	0.0	0.0	0.0	0.0	5.4	5.1	80.5	5.1	3.9
	300	100.0	0.0	2.4	0.0	0.0	0.0	3.6	5.7	83.3	3.5	1.4
F200	350	100.0	0.3	14.3	0.2	0.0	1.0	7.7	0.0	75.4	1.0	0.0
	400	100.0	2.5	19.4	1.2	0.0	3.4	8.2	0.0	65.3	0.0	0.0

`

	450	100.0	1.4	17.8	1.0	0.6	5.0	7.5	0.0	58.8	0.0	7.7
	240	55.2	0.0	0.0	0.0	0.0	0.0	6.3	3.8	90.0	0.0	0.0
	300	100.0	0.0	11.9	0.0	0.0	0.0	7.0	1.3	77.7	2.2	0.0
	350	100.0	0.0	23.8	0.0	0.0	0.0	9.6	0.0	66.6	0.0	0.0
SCFa-Na-0.3%	400	100.0	1.3	24.3	0.8	0.0	3.0	10.5	0.0	60.1	0.0	0.0
	450	100.0	2.2	24.0	1.1	0.0	4.2	8.8	0.0	56.8	0.4	2.4
	240	0.0	0.0	0.0	0.0	0.0	0.0	0.0	0.0	0.0	0.0	0.0
	300	13.9	0.0	0.0	0.0	0.0	0.0	30.4	0.0	69.6	0.0	0.0
SCFa-Na-7.6%	350	28.7	0.0	0.0	0.0	0.0	0.0	21.2	3.1	56.2	0.0	19.6
	400	96.7	1.5	1.9	0.0	0.0	21.2	11.6	6.9	24.5	1.4	30.9
	450	100.0	0.5	7.3	1.8	2.0	24.8	1.7	1.9	46.6	0.0	13.5

[a] 1:C3 (propane and propylene); 2:BD; 3:trans-2-butene; 4:cis-2-butene; 5:acetone; 6:MPA; 7:3B2OL; 8:MEK; 9:isobutanol; 10:heavy species. Species identified include 2-methyl-2-cyclopenten-1-one, 3,4-dimethyl-2-Cyclopenten-1-one, 3,4,4-trimethyl-2-Cyclopenten-1-one, 2-methyl-Phenol, 3,4-dimethylphenol and 2,4-dimethylphenol.

As shown in Table 4-4, dehydration of BDO can occur even in the blank reactor tube. Little reaction occurs below 400 ^{0}C (<4% conversion), but at 400 ^{0}C over 30% of the BDO is converted to a mixture of MEK, MPA, 3B2OL, and C3 hydrocarbons, with MEK comprising almost 70% of the products.

With catalysts loaded in the reactor, both SCFa and F200 produce MEK as the major product. F200 always produces more MEK than SCFa. For both catalysts, BD selectivity increases dramatically with increasing temperature. Also, BD selectivity is always higher on SCFa than on F200. The difference in BD selectivity is most noticeable at 450 ^{0}C, where the BD selectivity on SCFa is 28%, versus less than 18% for F200. SCFa also produces more isobutanol and 3B2OL than F200 (Table 4-4) at low temperatures and acetone at high temperatures.
The catalysts appear to be relatively stable over time, at least on the time scale of hours. After running SCFa for seven hours, for example, the BD selectivity had changed from 24.7% to 22.6%, while conversion was still 100% at a temperature of 400^{o}C.

`

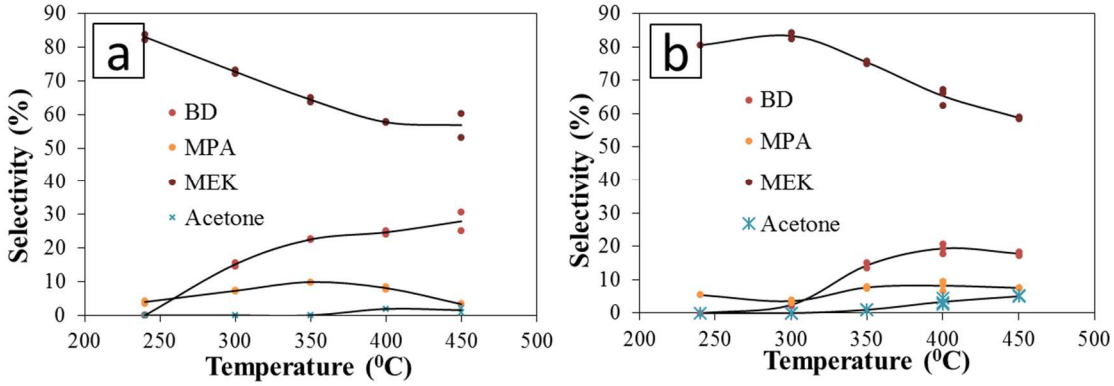

Figure 4-8. Comparisons of BD, MPA, MEK, and acetone selectivities from the reactions of BDO solution (2g/100 mL) over (a) SCFa; and (b) F200. Points are the experimental data and lines are the average value.

MEK is the major product from BDO dehydration even in the blank test. Higher temperature drives the reaction towards the formation of BD, and inhibits the formation of MEK. Two mechanisms are used to explain the formations of ketone structures. The enol structure can quickly form a keto structure via the keto-enol tautomerization as shown in Scheme 1[94].

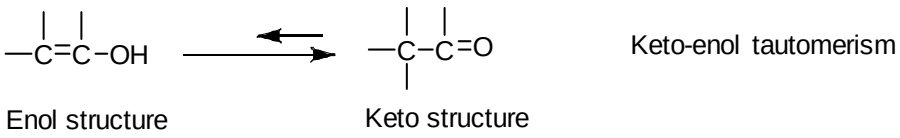

Scheme 1. Keto-enol tautomerism.

Another possible explanation is pinacol rearrangement, which is a typical 1, 2-shift reaction of vicinal diols under acidic condition and commonly believed to be the main pathway for MEK formation [95]. We have proposed a stepwise pinacol rearrangement mechanism for BDO dehydration (Scheme 2). A migration of hydrogen with a pair of electrons is known as a hydride shift, while migration with an alkyl group is known as a alkyl shift. Hydride migration leads to the formation of MPA, whereas methyl group migration produces MEK.

`

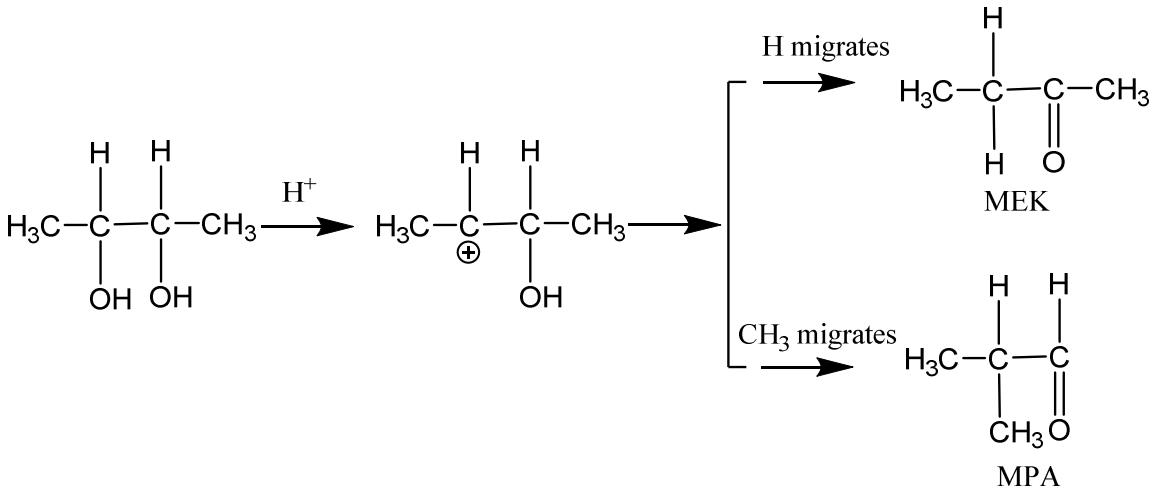

Scheme 2. MEK and MPA formation from pinacol rearrangement of BDO.

4.3.3. BDO dehydration over calcined alumina SCFa and F200

Figure 4-9 shows the BD selectivity for BDO dehydration over calcined SCFa and F200. In Figure 4-9-a, the BD selectivity slightly increases as the calcination temperature increases and then drops dramatically when the calcination temperature is 1100 ^{0}C. In Figure 4-9-b, a similar trend is found for F200. The BD selectivity increases as the calcination temperature increases, reaching a maximum at F200-600.The BD selectivity further decreases as the calcination temperature increases to 1000 and 1100 ^{0}C. As shown in Table 4-2, SCFa surface area dropped only 3% as the calcination temperature increased to 600 ^{0}C. A high surface area was maintained even at 1000 ^{0}C. The small change in surface area in the SCFa, SCFa-400, SCFa-600 and SCFa-1000 samples is likely the main reason behind the constant BD selectivity. For F200, the surface area monotonically decreases as the temperature increases, and the surface area losses are more noticeable than those in SCFa.

As already described, SCFa consistently gives higher BD selectivity than F200, even though both samples are alumina. This is likely due to differences in physical and chemical properties. Table 4-2 and Table 4-3 compare the two catalyst samples, and show that there are significant differences. However, these tables also show that F200 becomes more like SCFa in terms of both surface area and acid and base site densities as it is calcined. The F200 sample calcined at 600 ^{0}C, has a surface area of 184.6 m^2/g, which is close to the SCFa surface area 131 m^2/g. The acid and base site densities of F200-600 are 0.37 and 0.072 mmol/g respectively. When compared to F200 samples calcined at other temperatures, they are close to the SCFa acid

`

and base densities 0.24 and 0.059 mmol/g. It is interesting to note that these two samples gave similar catalytic results in BDO dehydration. We hypothesize that the higher concentration of acid sites present in F200 selectively produce MEK [13]. Another possibility is that well-crystallized forms of alumina are superior to less-crystallized forms for BD production, and that calcining F200 improves BD selectivity because it produces a more well-crystallized surface. As shown in Table 4-2, the crystallite size of F200 increases as it is calcined. Sato and coworkers proposed that calcination could be important in dehydration of diols due to changes in crystallinity [18].

Both SCFa and F200 alumina calcined at 1100 ^{0}C exhibited much lower BD selectivity. This can be explained by the transformation of γ-Al_2O_3 into the thermodynamic stable α-Al_2O_3 which is generally considered as the most inert of all the aluminum oxides [96].

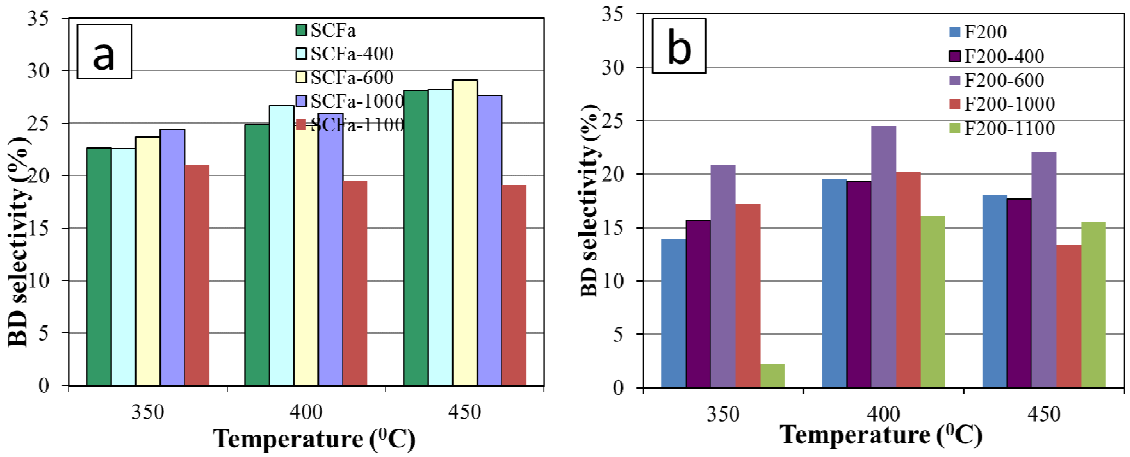

Figure 4-9. BD selectivity over calcined alumina SCFa (a); and F200 (b).

4.3.4. Sodium effect on BD selectivity

Different amounts of sodium were added to SCFa to determine how it affected BD selectivity. The results are shown in Figure 4-10, which shows that as the sodium loading increases, the BD selectivity decreases. As the Na_2O increases by 0.3%, only slight decreases are seen at 300, 400, and 450^{o}C. This suggests that the small amounts of sodium present in F200 are probably not responsible for the differences in BD selectivity between F200 and the higher-purity SCFa. As the sodium content increases to 7.6%, BD selectivity drastically decreases. In

`

addition, SCFa with high levels of sodium gave much lower conversions than unmodified SCFa, and produced large amounts of acetone (21.2% and 24.8%) at 400 and 450 ^{0}C respectively. The formation of acetone on sodium-modified SCFa may be attributed to the enhancement of basic properties of the alumina catalysts resulting from sodium impregnation. It has been reported that the conversion rate of cinnamaldehyde to benzaldehyde and acetaldehyde increased as the basicity increased [97], indicating that the basic sites promote the retro-aldol condensation, which breaks the C=C bond. In contrast, more acidic sites catalyze aldol condensation reactions, where MVK has been found to be the sole product from formaldehyde and acetone [98]. In this study, considering that the acetone selectivity increased as the catalyst basicity was enhanced by sodium (shown in Figure 4-2), we propose a mechanism to explain the acetone formation catalyzed by sodium-modified alumina through the retro-aldol condensation of MVK. Formaldehyde was not directly observed in the products when acetone was detected, however larger amounts of heavy species (shown in Table 4-4) were observed compared to BDO dehydration over SCFa. These heavier species may have been formed from the reaction of formaldehyde with other aldehydes and alcohols. To further validate the proposed mechanism, 3B2OL (2g/100mL) and MVK (2g/100mL) is separately feed into to the reactor with 0.5g SCFa-Na-7.6% catalyst at 400 ^{0}C. Acetone is found in both two experiments and MVK is also found in the reaction of 3B2OL. These results are consistent with the proposed mechanism.

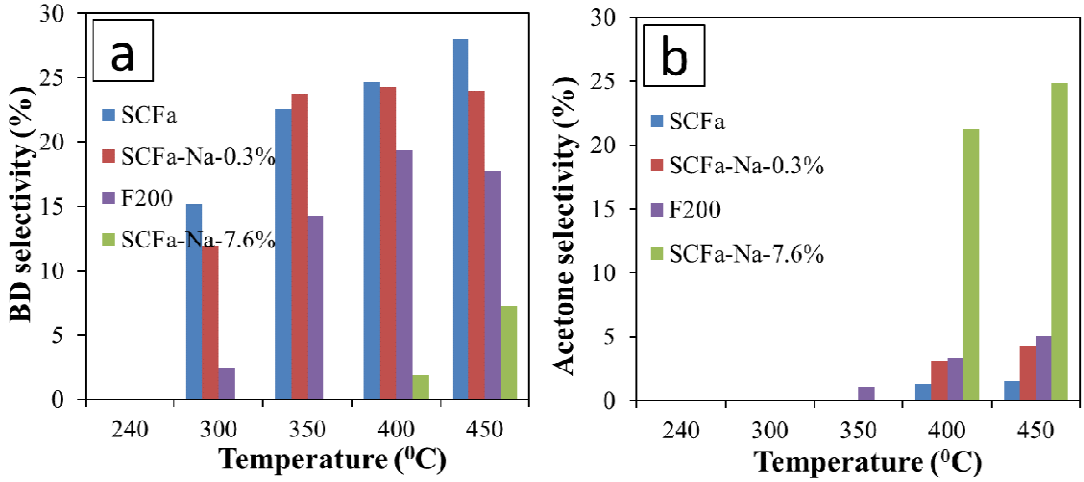

Figure 4-10. Effects of temperature on BD (a); and acetone (b) selectivity over SCFa, SCFa-Na-0.3%, F200, and SCFa-Na-7.6%.

`

4.3.5. Reaction mechanism

Table 4-4 shows that 3B2OL was only observed at low temperatures over SCFa, while at high temperatures it was not observed due to further dehydration to BD or other reactions. However, over SCFa-Na-7.6% catalyst, 3B2OL was observed only at high temperatures, while it was not observed at lower temperatures. This indicated that the strong base sites inhibited the formation of 3B2OL and further dehydration of 3B2OL to BD, which explains why BD selectivity decreased as the sodium loading increased.

Meanwhile, the inhibition of further dehydration of 3B2OL made the other reaction pathways for 3B2OL conversion possible over SCFa-Na-7.6%, such as dehydrogenation to MVK. Furthermore, the retro-aldol condensation was catalyzed by basic sites. In Scheme 3, we propose that the 3B2OL was converted into MVK by dehydrogenation on basic sites, which catalyzed the retro-aldol condensation by cleavage of the C=C bond to form acetone and formaldehyde. The detection of small amounts of hydrogen that accompany acetone formation when using the SCFa-Na-7.6% catalyst supports the hypothesis that dehydrogenation can play a role in the reaction mechanism for the base-modified catalysts.

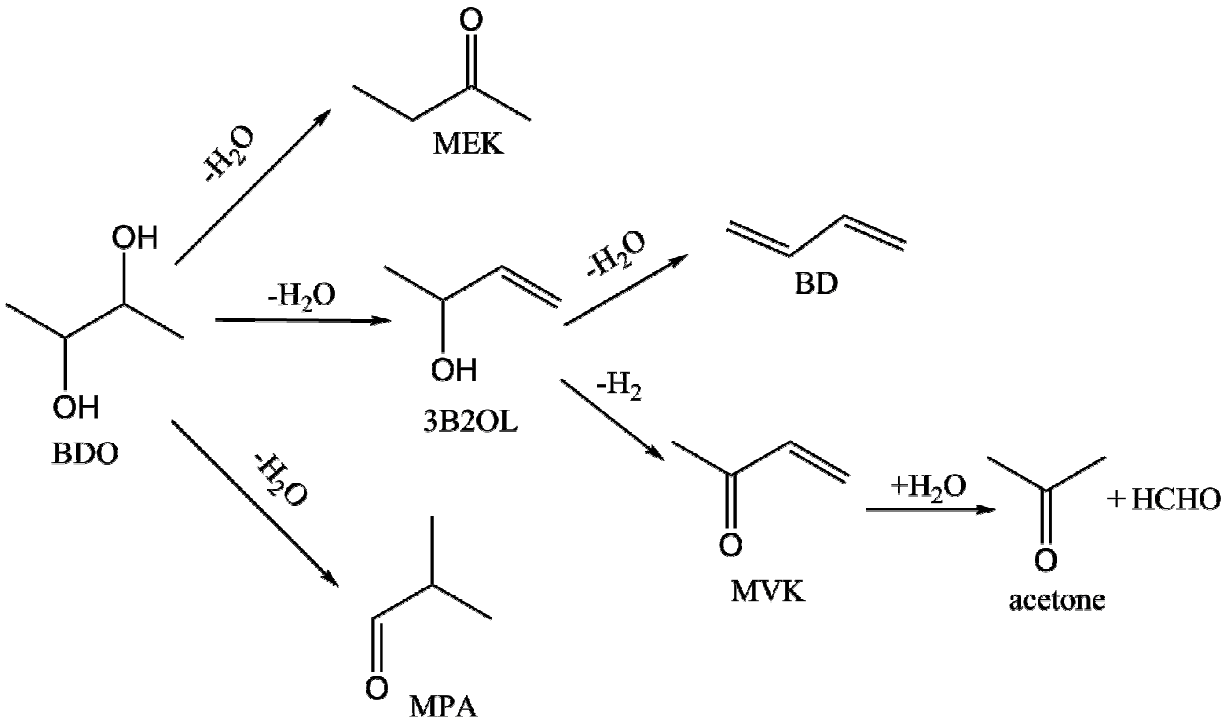

Scheme 3. Proposed reaction pathways of BDO conversion over alumina.

`

4.3.6. Residence time study

Figure 4-11 depicts BD, 3B2OL and BDO composition as functions of residence time in the reaction of BDO over SCFa at 300 ^{0}C in a stainless steel reactor. By adjusting the catalyst weight loading in the reactor and the feed rate of the aqueous BDO solution (2g/100 mL), residence time was varied from 0.00786 s to 0.109 s. Figure 4-11 shows that the 3B2OL composition initially increases to a maximum value at a residence time of 0.0133 s and then drop as the residence time increases, the gap between the data SCFa 0.1g and 0.25 g may due the experimental error. Meanwhile, the BD composition increases and the BDO composition decreases with increasing residence time. The trend for 3B2OL is what would be expected for a reaction intermediate in a series reaction, which indicates that 3B2OL is the intermediate in the route BDO dehydration to BD. At a temperature of 240 ^{0}C (see Table 4-4), BD was not observed over either form of alumina, however 3B2OL was observed instead, which indicates that high temperature is required for complete dehydration of BDO to BD.

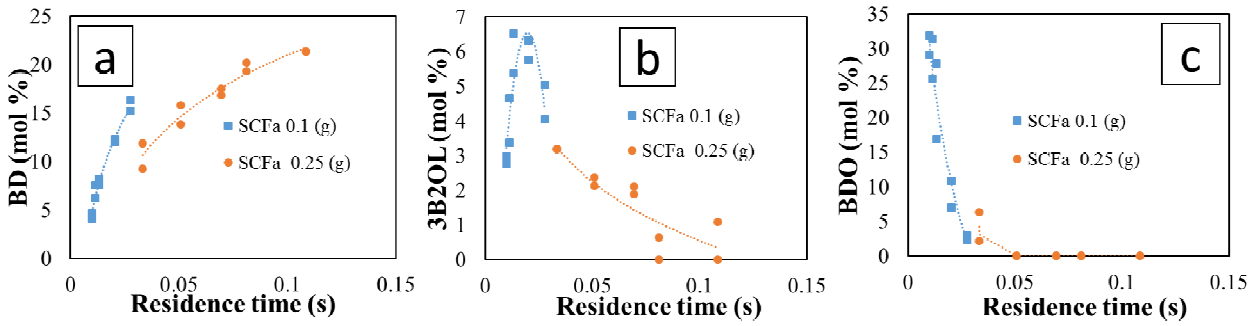

Figure 4-11. BD (a), 3B2OL (b) and BDO (c) composition as a function of residence time (points are the experimental data and lines are the trend line).

4.3.7. Effect of water vapor on dehydration performance over SCFa

BDO produced by fermentation is typically in a dilute aqueous solution, and the production of pure BDO requires expensive separation. Therefore, it is technologically significant to convert BDO to BD in dilute solutions. For this reason, the impact of water on BDO dehydration was studied in this work. Figure 4-12 shows the effect of water on dehydration of BDO over SCFa using pure BDO comparing with the previous diluted BDO (2g/100 mL). The flow rate for pure BDO was lower than that of diluted BDO (0.01 mL/min for pure BDO and 0.1 mL/min for diluted BDO) because higher flow rates of pure BDO led to problems in

`

reactor operation. It can be seen that acetone and MPA selectivities were not affected by the presence of water. Since the pure BDO flowrate is lower than diluted BDO, it had a longer residence time (0.397 s for pure BDO and 0.139 s for diluted BDO) and it should give a higher BD selectivity according to Figure 4-11, however the BD selectivity is higher in the presence of water vapor. The main reason for this is that heavy species are formed during the dehydration process due to BD polymerization and aldol condensation; including water in the reaction medium inhibits the formation of these heavy compounds. The diluted and pure BDO conversion in this figure is 100% for all the temperatures.

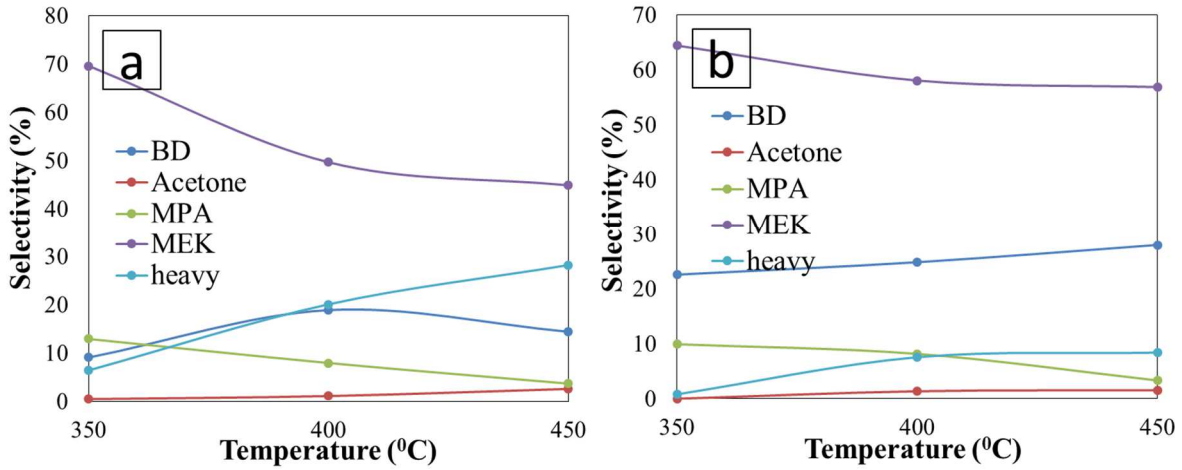

Figure 4-12. Product distributions from pure BDO (a); and BDO solution (2g/100 mL) (b) dehydration over SCFa.

4.3.8. DFT calculations for BDO dehydration

The products from experimental BDO dehydration (shown in Figure 4-8 and Table 4-4) indicate that the selectivity to MEK formation is substantially higher than BD on both SCFa and F200. It is also shown that calcination and sodium affect BD selectivity, and at much higher sodium content (SCFa-Na-7.6%), acetone formation becomes substantial. In order to gain further insights on these experimental observations by elucidating the proposed reaction pathways (Scheme 3), periodic DFT calculations were performed to understand the selectivity of BDO dehydration producing MEK and 3B2OL; and also to explore the relevant pathways for acetone formation.

Periodically bounded γ-Al_2O_3 slabs with the (110) facet, which is the preferentially exposed surface, are shown in Figure 4-13 [99, 100]. The 3-coordinated Al(III) site, which is catalytically active in alcohol dehydration [101, 102] , is highlighted with the gold color. The

`

sodium species were introduced as an adatom (equivalent to a Na mass fraction of 2.7%, as shown in Figure 4-13-b). In this discussion, we will primarily focus on the dry (dehydrated) surface. Calculations on hydroxylated surface were also performed, but the main conclusions are not affected by the hydroxylation.

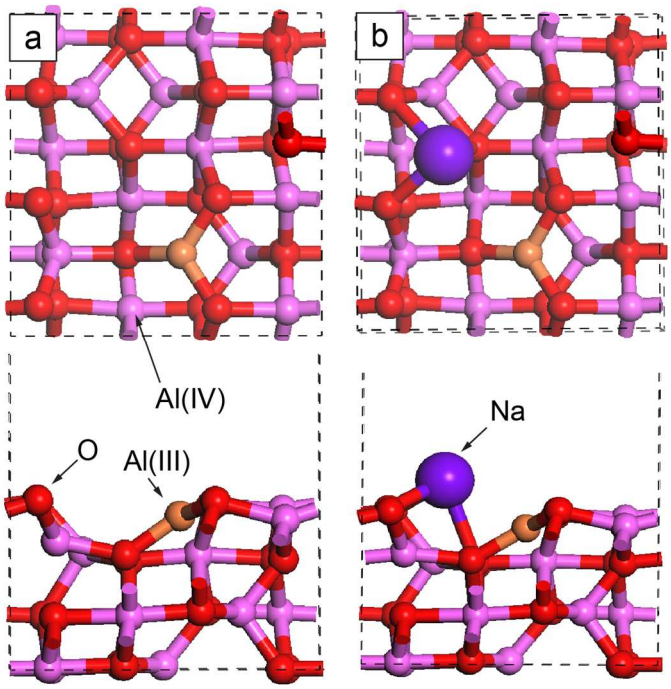

Figure 4-13. Top and side views of relaxed pristine (a) and Na-doped (b) γ-Al_2O_3 (110) surfaces. The Al(III) and Al(IV) sites are represented with gold and pink spheres respectively. Sodium is represented by the purple sphere and is labeled in the figure.

The optimized structures of experimentally relevant reaction species, such as BDO, CH_3-CH-CHOH-CH_3 (INT, according to Scheme 2), 3B2OL, MEK, and BD are shown in Figure 4-14.

`

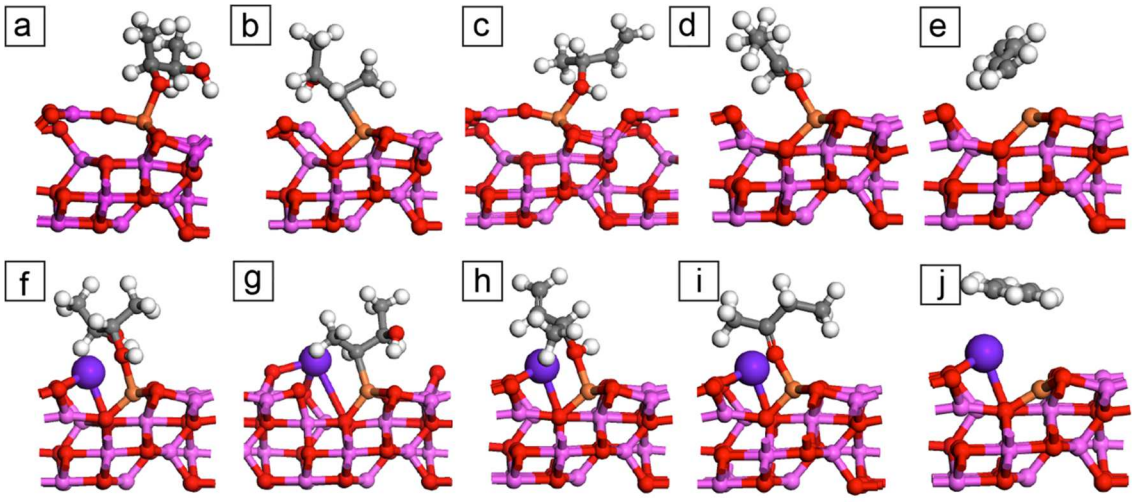

Figure 4-14. (a-e) Optimized structures for BDO, INT, 3B2OL, MEK, and BD on pristine γ-Al_2O_3 (110) surfaces; and (f-j) sodium-modified γ-Al_2O_3 (110) surfaces. White, grey, red, pink, gold, and purple spheres represent the H, C, O, Al (IV), Al(III), and Na atoms, respectively.

Molecular configurations and binding sites were explored to identify the structures (Figure 4-14) at global energy minima; and then were used to construct the potential energy surfaces. Except for BD, all the species prefer to interact with the Al(III) site in both pristine and sodium-modified (110) surface. BDO (a and f) and 3B2OL (c and h) bind via their hydroxyl groups; INT (b and g) binds with its unsaturated C atom; and MEK (d and i) binds with its ketone oxygen (as in C=O) at the Al(III) sites, respectively. Noticeable structural changes at the Al(III) site were observed upon BDO and 3B2OL adsorptions, as shown in Figure 4-14 (a and c), indicating that surface restructuring of the Lewis acid site may occur [103]. For sodium-modified alumina, however, its Al(III) site is found to be stable without significant structural changes.

`

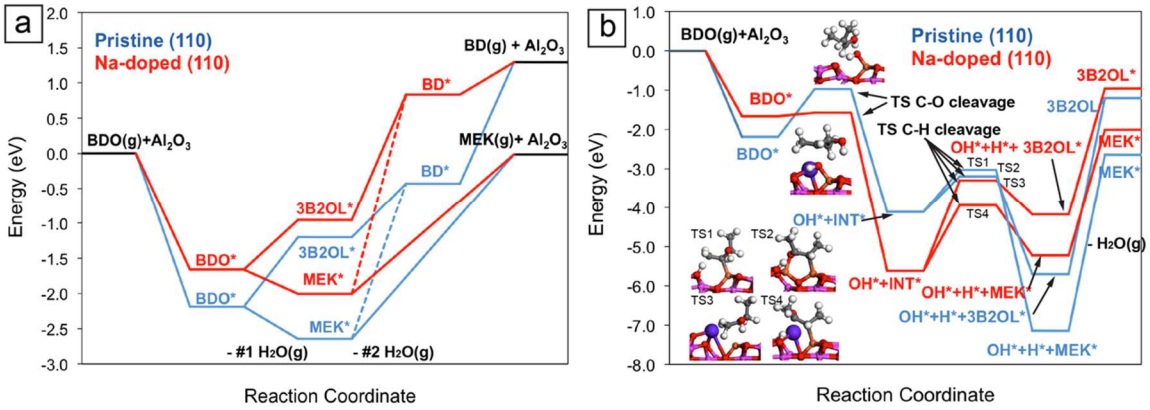

Figure 4-15. (a) Potential energies of the two-step BDO dehydration forming 3B2OL, MEK, and BD on pristine (blue) and sodium-modified (red) γ-Al_2O_3 (110) surfaces. The asterisks represent surface species. (b) Energy barriers for the first step of BDO dehydration on pristine (blue) and sodium-modified (red) γ-Al_2O_3 (110) surfaces. Inset figures are the transition state structures identified from DFT calculations.

Using gas-phase BDO and clean alumina surface as the reference (0 eV potential energy), the potential energy surfaces of the MEK and 3B2OL dehydration routes to BD formation (Scheme 3) are shown in Figure 4-15-a. For each dehydration step, the water from dehydration is treated as a gas phase species. The overall potential energies for BD production is lower on the pristine (110) surfaces. The adsorption energies of BDO on pristine and sodium-modified (110) surfaces (with the inclusion of van der Waals interactions) are 2.19 eV and 1.66 eV, respectively. The MEK route is much more energetically favorable than the 3B2OL route on both surfaces, due to stronger binding of MEK; and is consistent evidence supporting the observed higher MEK selectivity. The MEK desorption energies of MEK from the pristine and sodium-modified (110) surfaces are quite endothermic, at 2.63 eV and 1.99 eV, respectively.

BD is produced from a second dehydration, which is an endothermic step. As shown in Figure 4-15-a, BD formation from the 3B2OL route will be much more thermodynamically favorable compared to the parallel route from MEK, due to the steep potential well for MEK. Figure 4-15-a also shows that the production of BD should be more favorable on the pristine (110) surface than the sodium-modified (110) surface, which is also consistent with the trend derived from experimental product distribution corresponding to catalyst samples with lower sodium contents. The BDO dehydration pathways are also tested on hydroxylated alumina

`

surface (both pristine and sodium-dope), where the Al(III) site remains open and the rest of the surface is saturated with dissociated water molecules (Figure A-1). It can be seen that the free three-coordinate Al(III) sites remain catalytically active as the preferred binding site (Figure A-2). The overall reaction pathways shift to higher potential energies, and the dehydration energetics becomes more endothermic. Compared to the dry pristine surface, the MEK route is still energetically favorable, but to a lesser extent, indicating that hydroxylation could indeed influence BD selectivity. This behavior is manifested by the catalyst samples calcined at higher temperatures, corresponding to a less hydroxylated surface (Figure 4-9). The optimized surface and reaction species structures (Figure A-1– A-2), and the dehydration potential energies (Figure A-3and Figure A-4) are shown in the Supporting Information.

The kinetics of the first dehydration step in the MEK and 3B2OL routes is shown in Figure 4-15b. It is assumed that the first dehydration step proceeds via direct C-O bond activation, producing INT (as shown in Scheme 2) and one hydroxyl group. The first dehydration is completed with a dehydrogenation step via the C-H bond cleavage. The C-O activation energy barriers are 1.79 eV and 0.1 eV on respective pristine and sodium-modified alumina. The much lower energy barrier can be understood as Na being able to stabilize the transition state structure. The formations of 3B2OL and MEK result from INT dehydrogenation (via C-H bond cleavage). The transition state structures are shown as inset figures in Figure 4-15b. On pristine (110), these energy barriers are 1.08 eV (TS1) and 0.91 eV (TS2), respectively. On sodium-modified (110), the respective C-H bond cleavage barriers increase to 2.32 eV (TS3) and 1.68 eV (TS4). In particular, the barrier for TS4, which is responsible for MEK formation, is much lower (by approximately 0.64 eV) than the barrier for 3B2OL formation on the sodium-doped (110) surface. Since 3B2OL is the main intermediate forming BD, the higher energy barrier corresponding to the 3B2OL pathway could explain the lower BD selectivity observed experimentally.

`

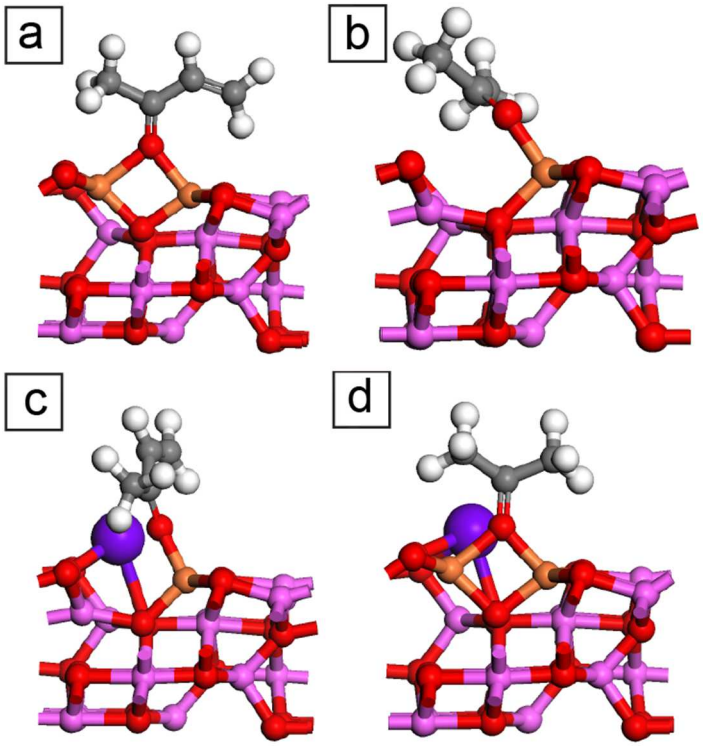

Figure 4-16. Optimized structures for MVK (a and c) and acetone (b and d) on respective pristine and sodium-modified γ-Al_2O_3 (110) surfaces. White, grey, red, pink, gold, and purple spheres represent the H, C, O, Al (IV), Al(III), and Na atoms, respectively.

DFT calculations were also performed to explore possible reaction pathways for acetone production observed experimentally for catalysts with high sodium content (e.g. SCFa-Na-7.6% in Figure 4-10). The proposed mechanism for acetone formation via retro-aldol condensation [104], involving MVK from 3B2OL dehydrogenation, was investigated. The optimized structures of MVK and acetone are shown in Figure 4-16. Like MEK, both molecules bind via their ketone group at the Al(III) sites of the pristine and sodium-modified (110) surfaces. The adsorption energies of acetone on pristine and sodium-modified surfaces are 2.69 eV and 2.27 eV, respectively.

`

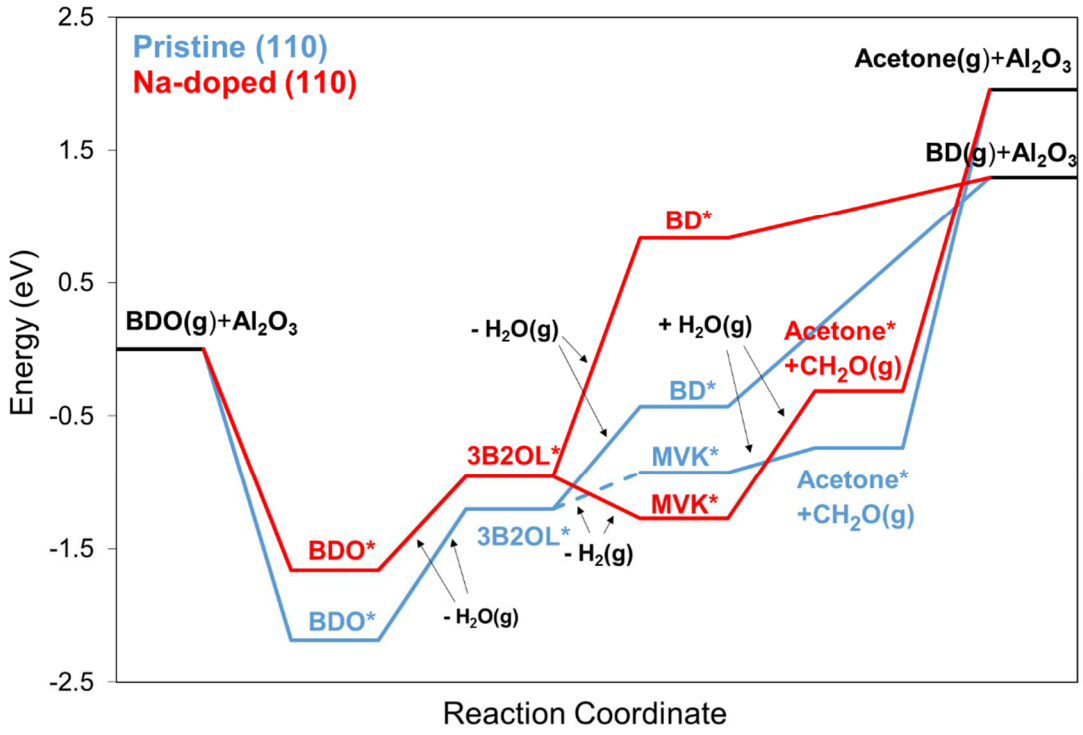

Figure 4-17. Potential energies for proposed reaction pathways responsible for acetone formation on pristine and sodium-modified γ-Al_2O_3 (110) surfaces.

The potential energies for the proposed 3B2OL→MVK→acetone pathways on two surfaces are shown in Figure 4-17. On the sodium-modified (110) surface, it is more energetically favorable for 3B2OL to form MVK via dehydrogenation (-0.32 eV exothermic, forming H_2 gas), versus dehydration forming BD (1.79 eV, endothermic). The retro-aldol condensation enables MVK to break the C=C bond, producing acetone and formaldehyde. This step is 0.96 eV endothermic on sodium-modified (110). DFT calculations suggest that the MVK pathway competes strongly with BD formation given sufficiently high sodium contents (i.e. 7.6% Na_2O), and hence is able to explain the observed acetone formation (Table 4-4). On the pristine (110) surface, both MVK and BD pathways are endothermic, with reaction energies of 0.28 eV and 0.77 eV respectively. Higher selectivity for BD production, based on experimental analysis, suggests that kinetics (with potential high C-H bond cleavage barriers) might favor the BD pathway on the more acidic pristine (110) surface. As shown in Figure A-5, similar trend can be noted regarding the selectivity for the acetone formation pathway, except that energetic

`

favorability for MVK more pronounced. On the hydroxylated pristine surface, the MVK and BD formation pathways remain competitive. Both trends are consistent with the calculations on the non-hydroxylated surfaces.

4.4. Conclusion

Dehydration of BDO was investigated over alumina catalysts at temperatures between 240 ^{0}C and 450 ^{0}C. Two different forms of alumina gave different product selectivities, with the higher purity form (SCFa) producing BD selectivities up to 10% higher than the lower purity form (F200). BD selectivity was enhanced by increasing reaction temperature and using longer residence times. CO_2-TPD revealed that enhancing the basic site of SCFa decreased the BD selectivity. Diluting BDO with water inhibited the formation of heavy species and increase BD selectivity. DFT calculations indicated that MEK were the most thermodynamically stable product on alumina surface which explains why MEK was the dominant product of BDO dehydration over alumina. The difference between the two forms of alumina was due to either the larger number of acid sites or lower crystallinity in F200 that gave a lower BD selectivity. It is hypothesized that sodium addition inhibits dehydration of 3B2OL to BD while enhancing dehydrogenation of 3B2OL to MVK. Retro-aldol condensation of MVK could then occur, leading to significant amounts of acetone produced on sodium-doped alumina catalysts. DFT calculation proved that retro-aldol condensation of MVK is more favored on Na-Al_2O_3 than on pure Al_2O_3.

`

Chapter 5 - 2, 3-butanediol dehydration over trimethylamine modified alumina

Abstract

The direct catalytic conversion of 2, 3-butanediol (BDO) to 1, 3-butadiene (BD) was studied over two commercial forms of alumina (denoted as F200 and SCFa) modified with triethylamine (TEA). The alumina surface acid/base properties were modified by TEA prior to reaction (ex-situ modification) and while reaction was occurring (in-situ modification). The results indicated that ex-situ modification of F200 via TEA slightly inhibited the BD selectivity, while the BD selectivity increased on SCFa with the same treatment. However, in-situ modification of F200 and SCFa by co-feeding TEA with BDO increased BD selectivity for both catalysts: the BD selectivity over F200 increased from 19.5% to 29.1% and the BD selectivity over SCFa increased from 24.8% to 35.2% at 400 ^{0}C. It is hypothesized that TEA acts to block strong acid sites that produce the undesired side-product, methyl ethyl ketone.

5.1. Introduction

1,3-butadiene (BD) is an important intermediate in the polymer industry, particularly for the production of synthetic rubber. Currently, it is exclusively produced from petroleum [11]; however, there has been extensive recent interest in producing BD from renewable resources to ensure an ample supply and reduce price volatility [9]. One potential route to renewable BD is to utilize 2,3-butanediol (BDO), which can be produced at a large scale from biomass via fermentation [105].

Early research by Winfield demonstrated that BDO could be dehydrated over thoria to produce BD [8], substantiating that BD can be produced from BDO if a suitable catalyst can be found. Dehydration of BDO can readily occur on zeolites [13] and sulfuric acid [12]. However, methyl ethyl ketone (MEK), rather than BD, is the dominant product due to the keto-enol tautomerization and pinacol rearrangement. Recently, Sato and coworkers have studied a variety of metal oxides for this reaction, and have reported that Sc_2O_3 gives remarkably high BD selectivity, especially when Al_2O_3 is added as a second catalyst bed. The BD selectivity was 94%

`

with 100 % BDO conversion [20]. While Sato's work is impressive, it relies on expensive rare earth metal oxides to achieve high BD selectivity. For this reason, we have been studying more conventional metal oxides for conversion of BDO to BD. In our previous work, the direct catalytic conversion of BDO to BD was studied over two forms γ-alumina at temperatures between 240 ^{0}C and 450 ^{0}C [106]. These two materials gave remarkably different results, with SCFa giving higher BD selectivity at all experimental conditions. We found that the alumina acid/base properties affect the product distribution of BDO dehydration. When F200 was calcined, the number of acid sites decreased and selectivity to BD increased until it was similar to that achieved on SCFa. We hypothesize that too much acidity leads to formation of MEK rather than BD, so the key to achieving high selectivity to BD is using a catalyst with the appropriate acid/base properties.

Recent published results also indicate that acid/base properties are key to converting BDO to BD. Kim and coworker studied the BDO dehydration over silica-supported Na/P catalysts and found that product distribution depended on the Na/P ratio. This ratio was important to provide a balance of acid and base sites. The optimal ratio for BD production was found to be 1.8-1.9 [107]. A patent granted to Hale reported on BDO dehydration over tungsten/Al_2O_3 with co-feeding MEK and triethylamine (TEA), and the author claimed that 48% BDO was converted into BD with no MEK or other impurities formed [108]. However, few details were provided about the experimental procedures.

The Hale patent suggests that treating catalysts with amines could improve BD selectivity in BDO dehydration. Other have explored using amines to modify the basicity of metal oxides. For example, amine-modified SBA-12 silica [109] and MCM-48 [110] have been synthesize, and it was shown that the grafting amine can increase the base strength of the surface. Shylec and coworkers demonstrated that supporting amines on a silica surface promoted aldol condensation by formation of acid-base pairs [111]. Bass and coworkers demonstrated that acid-base pair activity was greatly reduced when silanol groups were passivated [112]. These studies indicate that amine addition can impact acid/base properties when amine is chemically grafted to the surface, but don't necessarily explain Hale's results when amine is continuously flowing over a catalyst.

`

In this study, we are seeking a method to use TEA to modify the acid/base properties of alumina to improve the catalytic dehydration of BDO to BD. BDO dehydration has been carried out over TEA modified alumina samples prepared via both ex-situ and in-situ modification methods.

5.2. Experimental

5.2.1. Catalyst preparation

SCFa and F200 were obtained from Sasol and BASF, respectively. The catalyst pellets were crushed and sieved to >60 mesh before use. The compositions of the alumina samples as supplied by manufacturers are listed in Table 5-1.

Table 5-1. Comparison of compositions of SCFa and F200

Composition and chemical/physical properties	SCFa	F200
Al_2O_3 [%]	98	92.7
Na_2O [%]	0.002	0.3
SiO_2 [%]	0	0.02
Fe_2O_3 [%]	0	0.02
L.O.I (loss on ignition)[%]	2	7
Surface area [m^2/g]	131	341

To test the impact of adding amines to alumina, two types of catalysts were prepared: ex-situ and in-situ modified catalysts. Ex-situ modification means that TEA and alumina were mixed with water and sonicated for 30 min before drying in a vacuum oven (pressure -100kpa Temperature ~30 ^{0}C for 24 hours). In-situ modification means that TEA was co-fed with the BDO (2g BDO and 1g TEA in 100 mL aqueous solution) as the inlet.

5.2.2. Catalytic reaction

The dehydration of BDO was carried out in a fixed-bed Hastelloy® tube reactor of 0.305” inner diameter. Since Hastelloy is a potential catalyst, blank tests were performed in an empty tube with the same conditions as the actual catalytic activity tests. The blank results were reported in our previous work which showed that the blank tube led to little conversion with

`

nearly complete selectivity to MEK [106]. For all catalyst activity experiments, 0.5 g of catalyst was placed in the reactor between two plugs of quartz wool. Liquid phase BDO aqueous solution (2g/100 mL) was fed at a flowrate of 0.1 mL/min through a micro pump (Eldex) to the top of the reactor through a nebulizer, where it was mixed with 100 mL/min of N_2 (regulated by a Brooks 5850E mass flow controller), which is used as an internal standard for product analysis. The approximate residence time is 0.14 s. The reactor was heated by heating tape. The temperature was measured by a K-type thermocouple, and a controller was used to ensure that temperature was held constant at the desired value.

Product analysis was carried out on-line by a SRI 8610C gas chromatograph using TCD and FID detectors. The gas chromatograph was equipped with molecular sieve (to separate N_2 from organic products) and MXT-1 columns (60 m, ID 0.53 mm). The oven temperature was held at 40 ^{0}C for five minutes, then raised to 230 ^{0}C at a rate of 40 ^{0}C/minute, and the temperature remained constant for 15 minutes. Argon gas was used as the carrier gas. The following compounds were identified using the gas chromatograph: BD, acetone, 2-methylpropanal (MPA), 3-buten-2-ol (3B2OL), MEK and isobutanol. In addition to the above species, heavy products were detected. Their response factor was assumed to be the same as BDO, and their total amount is lumped together as “heavy species”. Condensed species were characterized using GC-MS (Shimadzu GCMS-QP2010 SE). Species identified include 2-methyl-2-cyclopenten-1-one, 3, 4-dimethyl-2-cyclopenten-1-one, 3,4,4-trimethyl-2-cyclopenten-1-one, 2-methyl-phenol, 3,4-dimethylphenol and 2,4-dimethylphenol.

Each experimental condition was repeated at least three times for each condition. All mass balances closed within 20 %, with most closing within 10%.

The conversion of BDO and selectivity of the main products were calculated as below:

$$\text{2, 3-butanediol conversion}=\frac{mole_{BDO,in}-mole_{BDO,out}}{mole_{BDO,in}}*100\% \quad (1)$$

$$\text{Selectivity}=\frac{mole_{i,out}}{mole_{products}}*100\% \quad (2)$$

where mole $_{\text{products}}$ means the moles of products of reaction, including MEK, MPA, BD and heavy products.

`

5.2.3. Catalyst characterization

Temperature programmed desorption of TEA was performed on an AMI-200. 100 mg of pelletized sample was used. The TEA was fed into the sample through a gas saturator and the adsorption was carried out at 240 ^{0}C, 300 ^{0}C, 350 ^{0}C and 400 ^{0}C respectively for 2 hours. After saturation, the sample was flushed in a He flow for 1 hour to remove physically adsorbed TEA. The temperature was then raised to 750 ^{0}C at a heating rate of 5 ^{0}C/min. The amount of TEA desorption from the sample was measured by a TCD and calculated by integrated the area under the curve linked to the calibration file that is specific to the active gas.

5.3. Results and discussion

5.3.1. Characterization

In order to study the impact of the TEA treatment on alumina, the TEA-treated ex-situ alumina and untreated alumina were heated to 800 ^{0}C at a heat rate of 5 ^{0}C/min, to qualitatively measure pre-adsorbed TEA on the alumina surface. The desorbed gas concentration signal were recorded by the TCD. Figure 5-1-a shows that for as-received SCFa, only one desorption peak was observed at 160 ^{0}C which is due to desorption of physically adsorbed water, while for the TEA treated alumina, two desorption peaks appear at 160 ^{0}C and 566 ^{0}C. The desorption peak at high temperature is assigned to the TEA desorption peak. Since SCFa#2 was treated with more TEA than SCFa#1, the TEA desorption peak area is larger than that in SCFa#1. Figure 5-1-b shows the pre-adsorbed TEA desorption on alumina F200. The water desorption peak is not obvious in Figure 5-1-b; however, the TEA desorption peak is consistently shown around 570 ^{0}C and desorption peak area increase as the TEA loading increase. The results indicate that TEA strongly adsorbed on the alumina surface.

`

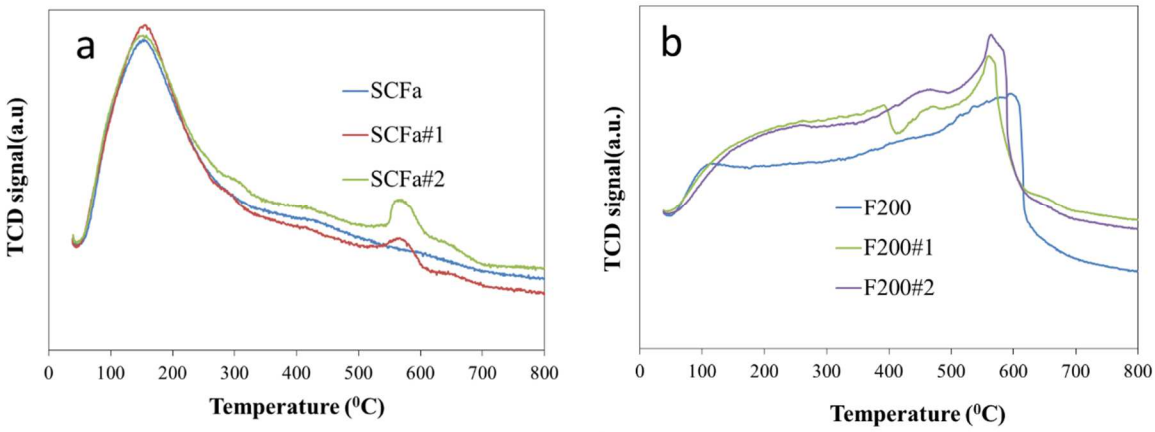

Figure 5-1. TPD of ex-situ TEA modified alumina SCFa (a) and F200 (b) with untreated alumina samples as comparison.

Table 5-2. Ex-situ modification of SCFa and F200.

Sample	Treatment
SCFa	No treatment
SCFa#1	2g SCFa+0.1 mL TEA + 6mL DI water
SCFa#2	2g SCFa+4 mL TEA + 6mL DI water
F200	No treatment
F200#1	2g F200+0.1 mL TEA + 6mL DI water
F200#2	2g F200+4 mL TEA + 6mL DI water

`

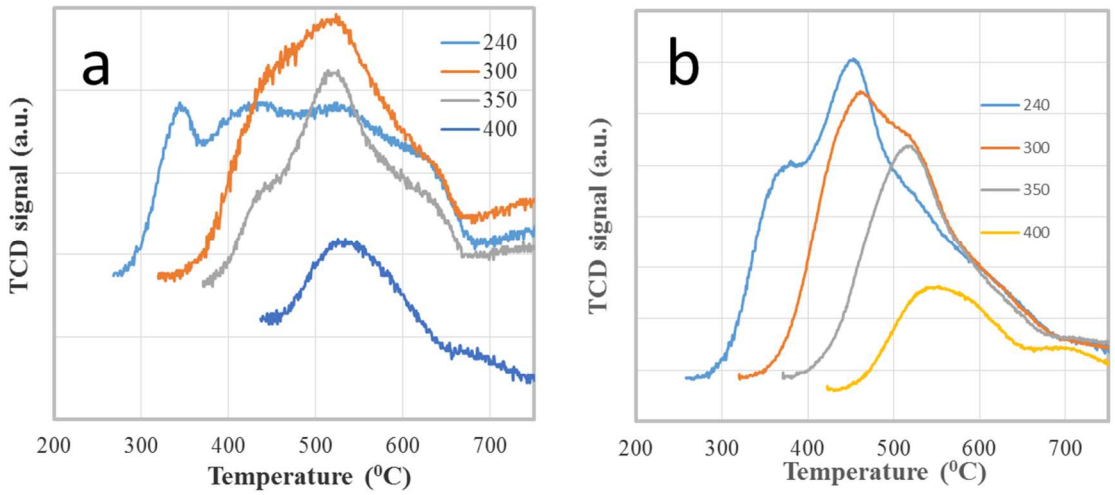

Figure 5-2. TEA-TPD of SCFa (a) and F200 (b) starting at various temperatures.

To further investigate the role of TEA in BDO dehydration, TPD experiments were run immediately after flowing TEA over SCFa and F200 at different temperatures to approximate what might be happening with TEA for in-situ modification. Figure 5-2 shows the results of these experiments. For both catalysts, similar overall trends can be seen. For the lowest temperature, multiple peaks can be seen. For SCFa, this manifests itself as a peak around 346 ºC followed by a broad feature at higher temperatures. For F200, there is a clear peak at 450 ºC superimposed on a broader feature starting at 280 ºC. As the adsorption temperature increases, so, too, do the desorption temperatures for both catalysts. This likely indicates that more stable adsorbed species are being formed as temperature increases, potentially by conversion of TEA to diethyl or monoethyl amine [113].

Table 5-3 compares the amount of TEA (or TEA decomposition products) released for the two different catalysts for in-situ and ex-situ modification. This table shows that there are some notable differences between the two types of alumina. The main difference is that F200 can adsorb approximately four times the amount of TEA as SCFa in the in-situ modification. This is consistent with the higher surface area of F200. The table also shows that the in-situ TEA modified alumina have much more amine adsorbed on the surface compared to that ex-situ TEA modification, thus the acid-base properties are greatly changed.

`

Table 5-3. TEA-TPD of SCFa and F200 in the in-situ and ex-situ modification

Samples	TEA release mmol/g sample
In-situ-F200-240	0.78
In-situ-F200-300	0.63
In-situ-F200-350	0.39
In-situ-F200-400	0.13
In-situ-SCFa-240	0.19
In-situ-SCFa-300	0.17
In-situ-SCFa-350	0.12
In-situ-SCFa-400	0.05
Ex-situ-F200#1	0.09
Ex-situ-F200#2	0.11
Ex-situ-SCFa#1	0.02
Ex-situ-SCFa#2	0.05

5.3.2. Ex-situ and in-situ modification impact on BDO dehydration

Figure 5-3 shows selectivity to BD in BDO dehydration as a function of temperature over the TEA-modified alumina SCFa and F200. For all experiments, complete conversion of BDO was achieved. A few notable trends can be observed. As the temperature increase, the BD selectivity increases for all catalysts. For F200, ex-situ modified samples have slightly lower BD selectivities at most temperatures, while the BD selectivity is slightly increased over the ex-situ modified SCFa samples. Furthermore, as the TEA loading increase on SCFa, the BD correspondingly increases. The in-situ modification of both SCFa and F200 were also studied and much more dramatic changes were seen. BD selectivity increased on both SCFa and F200 by up to 10% and 15 %, respectively.

`

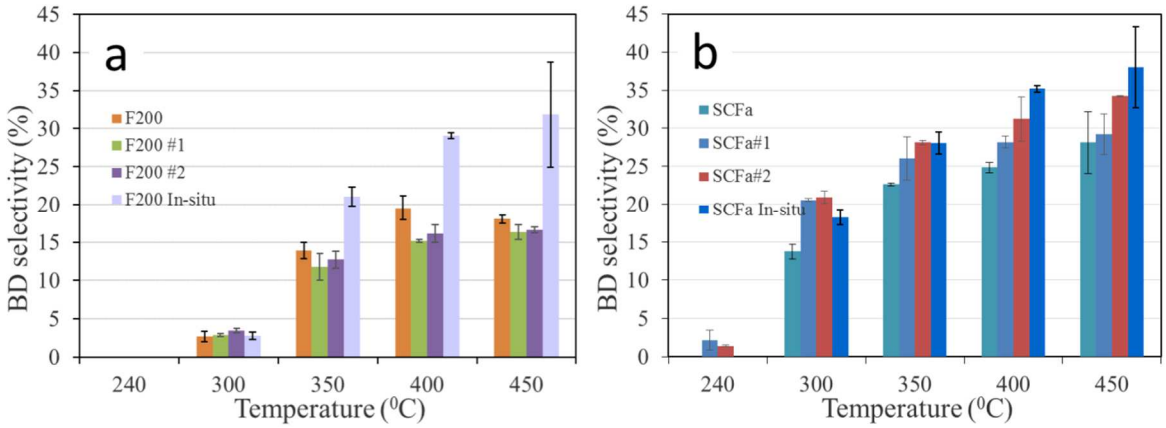

Figure 5-3. BD selectivity of BDO dehydration over TEA modified F200 (a) and SCFa (b).

Table 5-4 expands on the results shown in Figure 5-3 by tabulating the product distribution for BDO dehydration over the TEA-modified alumina SCFa and F200 at one representative temperature: 350 ^{0}C. BD, 2-methylpropanal (MPA) and MEK are the main products. The other products include 3B2OL and 2-methyl-1-propanol and heavy species. Higher amount of heavy species are seen at higher temperatures.

The results in Figure 5-3 confirm the trend suggested by Hale that TEA addition to the reactants can improve BD selectivity, though not to the level he reported [108]. On the other hand, attempts to modify acid-base properties by incorporating TEA prior to reaction did not substantially change the catalyst's basic properties (as seen in Table 5-3 and Figure 5-1) or its catalytic performance (Figure 5-3). It appears that the amount of TEA incorporated by ex-situ modification is too little to make much of a difference.

It is difficult to hypothesize exactly how in-situ modification is affecting the catalyst, but insights can be gained by looking at the results in Figure 5-3 and comparing the results in this paper with our previous results on the two forms of alumina. Figure 5-3 shows that some amine adsorbs on the catalyst surface for the entire temperature range studied. This means that when TEA is co-fed with BDO, TEA (or its decomposition products) will adsorb on catalyst sites and impact BDO chemistry. We hypothesize that TEA is absorbed on the strong Lewis acid sites on the alumina surface (aluminum atoms). This inhibits MEK formation which is favored on acid catalysts, resulting in higher selectivity to BD. This hypothesis is consistent with our previous work where calcining F200 lowered its surface area and acid site density, increasing BD selectivity. Figure 5-3 shows that in-situ catalyst modification by adding TEA to the feed

`

impacts the BD selectivity more for F200 than for SCFa. This can be explained by Figure 5-2 and Table 5-3, which show much higher amounts of adsorbed amine for F200 than SCFa: the higher surface area of F200 adsorbs more TEA, so its catalytic performance is impacted to a greater degree than SCFa.

Table 5-4. Dehydration of BDO over TEA modified alumina SCFa and F200 at 350 ^{0}C.

Selectivity (mol %)	Catalyst							
	F200	F200 #1	F200 #2	F200 In-situ	SCFa	SCFa#1	SCFa#2	SCFa In-situ
BD	14.30	11.76	12.70	21.05	22.60	26.56	27.79	28.05
MPA	7.70	8.06	7.95	9.13	9.90	11.28	11.96	10.06
MEK	75.40	78.06	74.89	69.82	64.40	61.75	59.37	61.13
Others[a]	2.60	2.12	4.46	0.00	3.10	0.41	0.87	0.77

[a] Others include: 3-buten-2-ol, 2-methyl-1-propanol and heavy species.

5.4. Conclusion

Dehydration of BDO was investigated over TEA modified alumina between 240 ^{0}C and 450 ^{0}C. TPD of TEA ex-situ modified alumina indicated that the TEA is strongly adsorbed on the alumina surface. The ex-situ modified F200 slightly decreased the BD selectivity, while the phenomenon is reversed over TEA modified SCFa: as the TEA loading increased, the BD selectivity correspondingly increased. In-situ modification significantly increased BD selectivity for both catalysts. We hypothesize that the TEA is adsorbed on strong acid sites, inhibiting the MEK formation pathway.

`

Chapter 6 - Transformation of 2, 3-butanediol in a dual-bed catalyst system

Abstract

The catalytic dehydration of 2, 3-butanediol (BDO) was investigated over two-bed catalysts, Sc_2O_3+Al_2O_3, Sc_2O_3+silica-alumina and Sc_2O_3+zirconia (dopant are calcium and ceria), at temperatures between 300 ^oC and 400 ^oC. Both Sc_2O_3+alumina and Sc_2O_3+silica alumina gave 1, 3-butadiene (BD) selectivity of about 61%, while Sc_2O_3+zirconia gave BD selectivity much less than 61%. Sc_2O_3+zirconia produced 2,5-dimethylphenol with selectivity reaching 12% at a maximum. The BDO dehydration over a single bed of zirconia catalyst was studied at various residence time. 2,5-dimethylphenol concentration increased as the residence time increased. Possible intermediate to form 2,5-dimethylphenol from BDO are methyl vinyl ketone (MVK), 3B2OL and acetoin. Sc_2O_3 can converter the BDO to 3-buten-2-ol (3B2OL) as the first bed, while the second bed catalyst greatly affected the product distribution. Acidic oxides such as alumina oxide and silica alumina are better catalyst to convert 3B2OL to BD, while catalysts with stronger basic sites catalyze condensation reactions that ultimate lead to phenols like 2,5-dimethyl phenol.

6.1. Introduction

The catalytic conversion of biomass to chemicals has received extensive attention recently because it offers a means for sustainable chemical production. Recently, 2,3-butanediol (BDO) has been identified as a promising intermediate in the conversion of biomass to industrial chemicals, both because it can be produced at a high yield via fermentation of glucose and xylose [10] and it can be converted to a variety of chemicals including 1,3-butadiene (BD) [20], methyl ethyl ketone (MEK) [114], 3-buten-2-ol (3B2OL) [18]. Strong acid catalysts, such as zeolites, yield MEK via Pinacol rearrangement with nearly 100% selectivity [114]. BD is the product following two dehydration steps, but most metal oxides catalysts favor production of MEK [106]. However, ThO_2 and Sc_2O_3 have been found to give high yield to BD [8, 20]. These studies show the utility of BDO for production of chemicals and also point to the complexity of BDO chemistry.

`

One possible extension of the work on catalytic chemistry of BDO is to employ multiple catalyst beds in order to direct BDO chemistry towards a desired product. This was recently demonstrated by Duan and coworkers who employed a two-bed catalytic system consisting of Sc_2O_3 as the first bed and Al_2O_3 as the second bed [20]. This system took advantage of the selectivity of Sc_2O_3 towards 3B2OL, the key intermediate in production of BD [106] , and the acidic nature of Al_2O_3 to dehydrate 3B2OL to BD. This research proposes that a two-bed system can be used to produce a variety of hydrocarbons and oxygenates from BDO by taking advantage of the wide variety of types of chemicals that can be produced from BDO (ketones, aldehydes, unsaturated alcohols, unsaturated hydrocarbons) and the ability to tune the catalytic properties of the two catalyst beds.

In this work, Sc_2O_3 was selected as the first catalyst bed because of its ability to selectively convert BDO to 3B2OL. The composition of the second bed was modified to determine the extent to which the catalytic properties of the second bed could direct the product selectivity in different directions. Two distinct types of catalytic materials were selected for the second bed. The first are typical acid catalysts (Al_2O_3 and SiO_2- Al_2O_3) that would be expected to favor dehydration pathways to convert 3B2OL to BD. The second are a series of CaO and CeO2-modified zirconia catalysts. Ceria modified zirconia has been shown to have activity for Hoffman elimination of secondary alcohols to alkenes [115], suggesting possible activity for converting 3B2OL into BD, but also have strong base sites that could promote other reactions such as aldol condensation [116]. It is shown in this work that the catalytic properties of the second bed have a significant influence on the ultimate produce selectivity, and that unexpected products can arise when a two-bed system is used.

6.2. Experimental

6.2.1. Catalyst preparation

Sc_2O_3 was purchased from Sigma-Aldrich and calcined in air at 800 ^oC for 3 hours before use. Silica alumina SiAl3111 (SiAl) were obtained from DAVICAT (SiO_2, 85.7%; Al_2O_3, 11.3%, Density, 0.35 g/cc; Pore Volume, 1.15 cc/g; BET Surface Area, 424 m^2/g). Alumina SCFa were obtained from Sasol and the catalyst pellets were crushed and sieved to >60 mesh before use. Zirconia catalyst were obtained from Daiichi Kigenso Kagaku Kogyo and used as

`

received. The compositions of the zirconia samples as supplied by manufacturer are listed in Table 6-1.

6.2.2. Catalytic reaction

The dehydration of BDO was carried out in a fixed-bed Hastelloy® tube reactor of 0.305" inner diameter. The catalyst was placed in the reactor between two plugs of quartz wool. Pure liquid BDO was fed at a flowrate of 0.018 mL/min through a micro pump (Eldex) to the top of the reactor through a nebulizer, where it was mixed with H_2 (regulated by a Brooks 5850E mass flow controller), which is used as an internal standard for product analysis. The reactor was heated by heating tape. The temperature was measured by a K-type thermocouple, and a controller was used to ensure that temperature was held constant at the desired value. Product analysis was carried out on-line by a SRI 8610C gas chromatograph using thermal conductivity detector (TCD) and flame ionization detector (FID) detectors. The gas chromatograph was equipped with molecular sieve (to separate H_2 from organic products) and MXT-1 columns (60 m, ID 0.53 mm). The oven temperature was held at 40 ^oC for five minutes, then raised to 230 ^oC at a rate of 40 ^oC/minute, and the temperature remained constant for 15 minutes. Argon gas was used as the carrier gas. The following compounds were identified using the gas chromatograph: BD, acetone, 2-methylpropanal (MPA), 3-buten-2-ol (3B2OL), MEK and isobutanol (MPO). Condensed species were characterized using GC-MS (Shimadzu GCMS-QP2010 SE). Species identified include 2-methyl-2-cyclopenten-1-one, 3,4-dimethyl-2-cyclopenten-1-one, 3,4,4-trimethyl-2-cyclopenten-1-one, 2-methyl-phenol, 3,4-dimethylphenol and 2,5-dimethylphenol. All mass balances closed within 20 %, with most closing within 10%.

The conversion of BDO and selectivity of the main products were calculated as below:

$$\text{2, 3-butanediol conversion}=\frac{mole_{BDO,in}-mole_{BDO,out}}{mole_{BDO,in}}*100\% \quad (1)$$

$$\text{Selectivity}=\frac{mole_{i,}}{\sum mole_{i,}}*100\% \quad (2)$$

where M_i means the mole number of product times the carbon number in the product.

`

6.2.3. Catalyst characterization

6.2.3.1. XRD

X-ray diffraction measurements were performed on the catalyst powders with a Rigaku MiniFlex II desktop X-ray diffractometer with Cu Kα radiation (λ=0.15406 nm) in an operation mode of 30 kV and 15 mA. Data were collected from 10^0 to 80^0 with a scanning rate of 1^0/min.

6.2.3.2. TPD

Temperature programmed desorption of ammonia (NH_3-TPD) was performed on an AMI-200. 200 mg of sample was treated under Helium for 4 hours at 600 ^{o}C. Next, 1% ammonia balanced in Helium was flowed over the catalyst for 2 hours. After saturation with ammonia, the sample was flushed in a He flow at 120 ^{o}C for 1 hour to remove physically adsorbed ammonia. The temperature was then raised to 600 ^{o}C at a heating rate of 5 ^{o}C /min. The amount of ammonia desorption from the sample was measured by a TCD. The peak area was converted to moles of gas by using a calibration file created for the species of interest. CO_2-TPD was performed using the same procedure with 10% CO_2 in Helium as the adsorbate.

6.2.3.3. TPR

Temperature-programmed reduction (TPR) studies were conducted with an Altamira AMI-200. 100 mg samples were treated in He at 550 ^{o}C for 1 h before TPR was performed. TPR was carried out in a flow of 10% H2/Ar at a heating rate of 10 ^{o}C /min. H2 consumption was recorded by a TCD.

6.2.3.4. Raman

Raman spectra of the films were recorded using a 0.55 m spectrometer (iHR550, Horiba-Jobin Yvon) that was coupled to an upright microscope (BX41, Olympus) and a light source of 633 nm HeNe laser.

6.2.3.5. XPS

X-ray photoelectron spectroscopy (XPS) data were recorded using a PerkinElmer PHI 5400 electron spectrometer with an achromatic Al Ka X-ray source (1486.6 eV) operating at 300 W (15 KV and 20 mA).

`

6.3. Results and discussion

6.3.1. Characterization

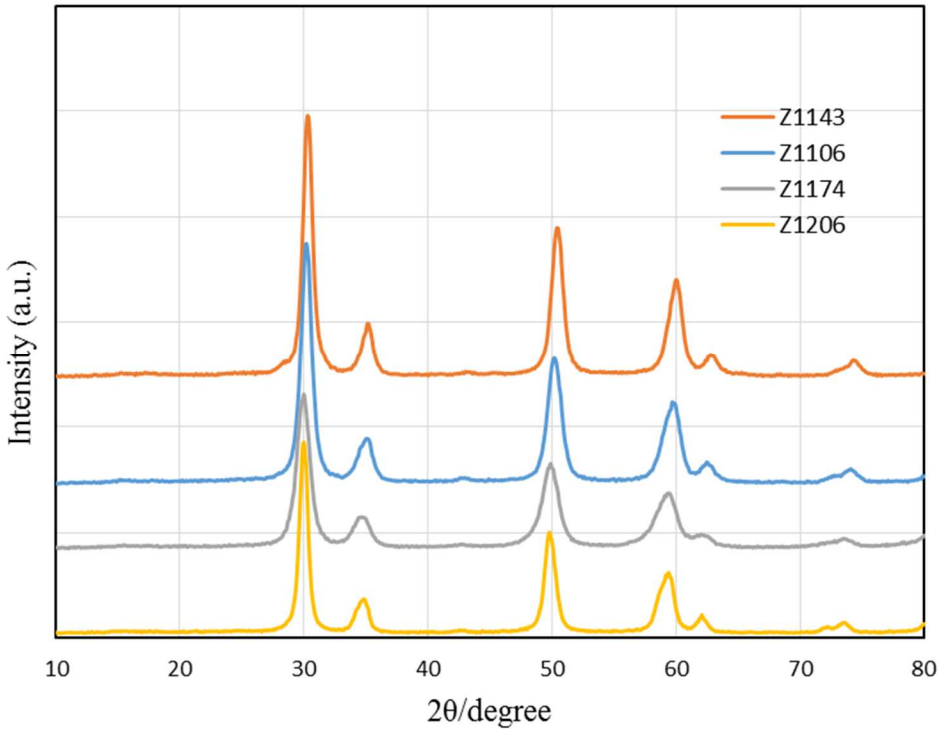

Figure 6-1. XRD patterns of zirconia oxides Z1143= $Ca_{0.04}Zr$, Z1106= $Ce_{0.1}Zr$, Z1174= $Ce_{0.2}Zr$, and Z1206= $Ce_{0.19}Zr$.

Figure 6-1 shows the XRD patterns of the zirconia samples. The diffraction peak distribution are consistent quite well among the zirconia samples. The tetragonal ZrO_2 phase characteristic peak are at 2θ ~ 30.2, 34.8 and 35.2° [117] and cubic ZrO_2 phase peaks are at 2θ ~ 30 and 34.8° [118]. Four zirconia samples all show diffraction peaks are 2θ~ 30.2 and 35°. The diffraction peaks at 2θ ~ 30° for $Ca_{0.04}Zr$ shifts to lower 2θ degree as the ceria content in ZrO_2 increase. This is due to larger ionic radius of Ce^{4+} compared to that of Zr^{4+} [115]. Since the free phase of CaO and CeO_2 are not observed, the CaO, CeO_2 and ZrO_2 mixed oxides form a solid solution. Since tetragonal and cubic phase are almost identical and the weak and broad diffraction peaks obtained in the sample make it difficult to differentiate the cubic or tetragonal phase in the zirconia samples. The identification of the phase is confirmed in the Raman spectra

`

shown in Figure 6-2. The Raman spectra of the four zirconia samples are relatively close to each other, with six feature peaks at 137, 244, 311, 457, 599, 630 cm^{-1} that are typical of a tetragonal ZrO_2 phase [119] Cubic zirconia would show a single Raman peak around 465 cm^{-1} [120].

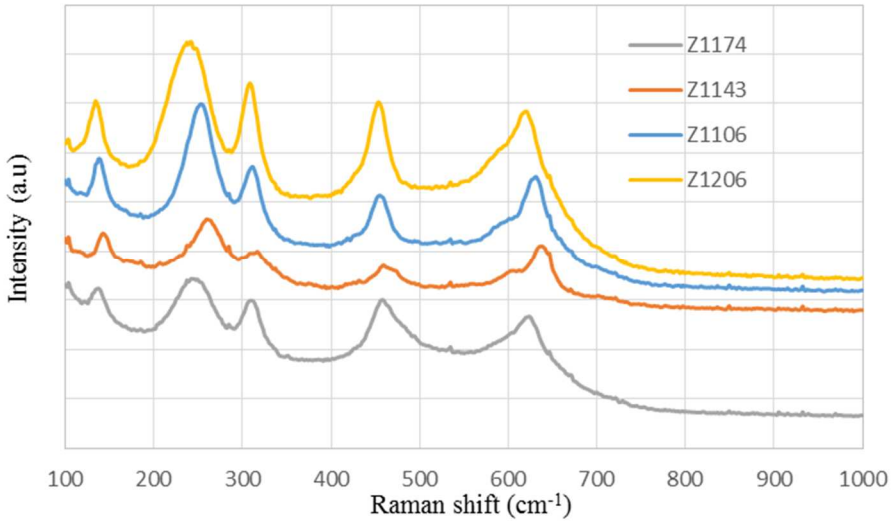

Figure 6-2. Raman spectra of zirconia samples Z1143= $Ca_{0.04}Zr$, Z1106= $Ce_{0.1}Zr$, Z1174= $Ce_{0.2}Zr$, and Z1206= $Ce_{0.19}Zr$.

Figure 6-3 shows the NH_3-TPD and CO_2-TPD of zirconia samples. A broad NH_3 desorption peak extends from 120 to 500 ^oC. The CO_2 desertion peak also extends over a wide temperature range, showing two desorption peaks for all samples except $Ce_{0.19}Zr$. The acid and base site densities are shown in Table 6-1. It is easy to see that the even though sample $Ce_{0.19}Zr$ has similar a compositions $Ce_{0.2}Zr$, it has much fewer acid and base sites. Comparing samples $Ce_{0.1}Zr$ and $Ce_{0.2}Zr$, as the ceria content increases, the acidity decreases while the basicity increases because ceria possess a large number of basic sites [121]. $Ca_{0.04}Zr$ has 4% CaO which can possibly explain its higher basicity. Lafaye and coworker compared the various Ceria sample and found that $CeZrO_2$ with Ce/Zr molar ratio 3:1 had acid and base site densities of 283 and 171 µmol/g respectively [122]. These results are close to the zirconia samples results reported here. The acid/base sites density of alumina SCFa and silica-alumina SiAl3111 are 0.24/0.059 and 0.289/0.157 mmol/g respectively, indicating that SCFa and SiAl3111 are relatively acidic catalysts compares to the other four zirconia catalysts.

`

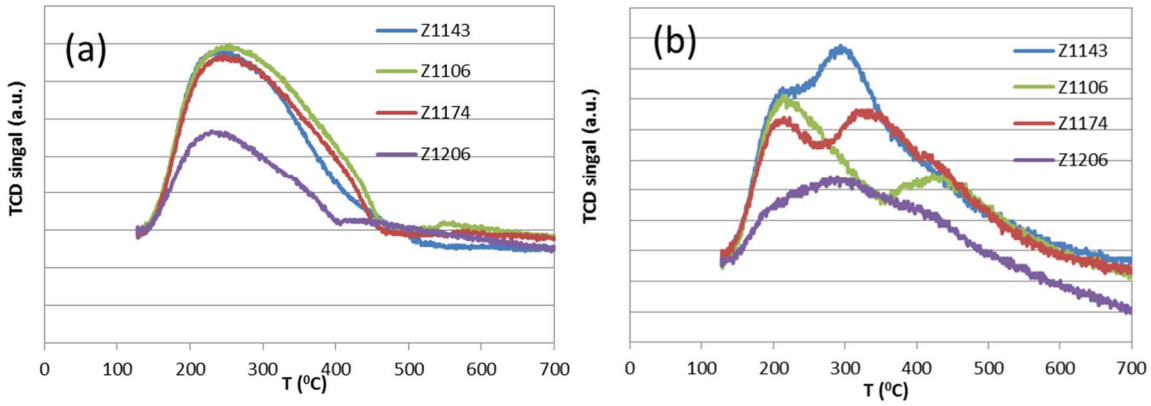

Figure 6-3. NH_3-TPD (a) and CO_2-TPD (b) of zirconia samples Z1143= $Ca_{0.04}Zr$, Z1106= $Ce_{0.1}Zr$, Z1174= $Ce_{0.2}Zr$, and Z1206= $Ce_{0.19}Zr$.

Table 6-1. Comparison of zirconia catalyst composition.

Name	Substance	Formula	Short name	[a]Ce/Zr theor	[b]Ce/Zr exp	Acidity (mmol/g)	Basicity (mmol/g)
Z1143	calcium doped zirconia	$(CaO)_{0.04}(ZrO_2)_{0.96}$	$Ca_{0.04}Zr$	0	0	0.322	0.305
Z1106	ceria doped zirconia	$(CeO_2)_{0.1}(ZrO_2)_{0.9}$	$Ce_{0.1}Zr$	0.11	0.15	0.333	0.254
Z1174	ceria doped zirconia	$(CeO_2)_{0.2}(ZrO_2)_{0.8}$	$Ce_{0.2}Zr$	0.25	0.40	0.310	0.278
Z1206	cerium stabilized zirconia	$(CeO_2)_{0.193}(ZrO_2)_{0.807}$	$Ce_{0.19}Zr$	0.24	0.41	0.150	0.187

[a] The Ce/Zr is calculated based on formula composition.

[b] The Ce/Zr is measured by XPS.

`

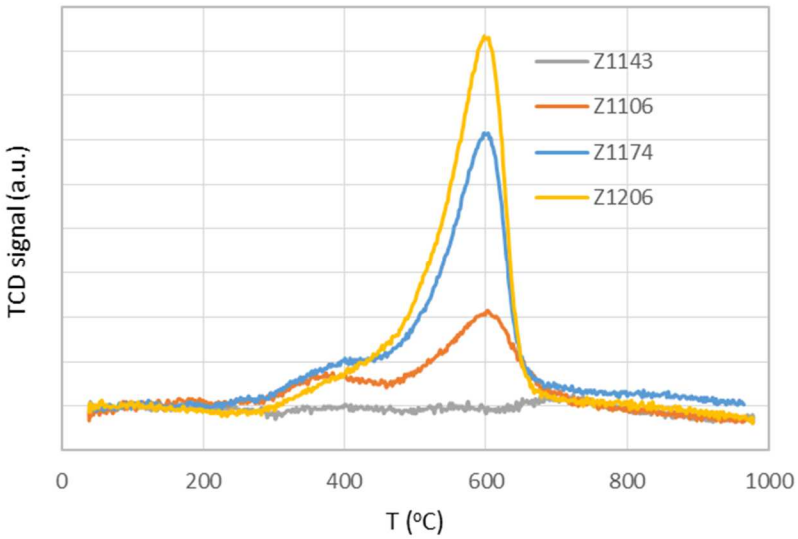

Figure 6-4. H_2-TPR profiles of CeO_2-ZrO_2 mixed oxides Z1143= $Ca_{0.04}Zr$, Z1106= $Ce_{0.1}Zr$, Z1174= $Ce_{0.2}Zr$, and Z1206= $Ce_{0.19}Zr$.

Figure 6-4 shows the TPR results of the CeO_2-ZrO_2 mixed oxides. It is easy to see $Ca_{0.04}Zr$ which has 96 % zirconia consumes a small amount of H_2. As the ceria content increase ($Ce_{0.19}Zr$ has more ceria on the surface), the consumption of H_2 greatly increase which means the reducibility of zirconia greatly increases by the incorporation of ceria. Li and cowokers attributed the enhancement of the H_2 consumption to the increase of the lattice oxygen mobility in CeO_2-ZrO_2, since the incorporated ceria can distort the zirconia structure and make the lattice oxygen more active to react with H_2 [123]. Two peaks are observed at 380 and 600 ºC in $Ce_{0.1}Zr$ and $Ce_{0.2}Zr$, which possibly correspond with the reduction of surface oxygen and bulk oxygen respectively [25]. Table 6-1 also shows the surface atomic ratio of Ce/Zr for four samples, which are consistently higher than those of the theoretical values. This suggests that the ceria concentration is higher on the surface. Similar results were also found by Martínez-Arias and their explanation was that the differences in the charge-to-radius ratio between Ce^{3+} and Zr^{4+} would favor precipitation of Zr first, leading to Ce precipitation later that forms the external parts of the agglomerates, causing the cerium enrichment on the surface [115, 124].

6.3.2. Catalytic Results

The primary hypothesis of this research is that BDO can be converted to a variety of chemicals by selecting multiple catalytic functionalities that favor specific reaction pathways in

`

the complex reaction mechanism for BDO catalytic chemistry. Sc_2O_3 offers the unique ability to dehydrate BDO to 3B2OL, rather than MEK [18]. Because of this capability, this work considered Sc_2O_3 as the first catalyst bed, where a second bed could then be selected to convert 3B2OL to BD and other products.

Figure 6-5 shows BDO dehydration over a single catalyst bed comprised of 1g Sc_2O_3. High temperature increases the BDO conversion. 3B2OL selectivity decreases with the temperature from 90% at 325 ^oC to 34% at 411^oC, while the BD and MEK selectivities both increase with temperature. Duan and coworker studied the BDO dehydration over ZrO_2, and their results also showed that the 3B2OL selectivity decreases as the temperature increases while the BD and MEK selectivities both increase with temperature [17]. Our previous results also showed that 3B2OL was produced at low temperatures while it disappeared when temperature was increased [106] .

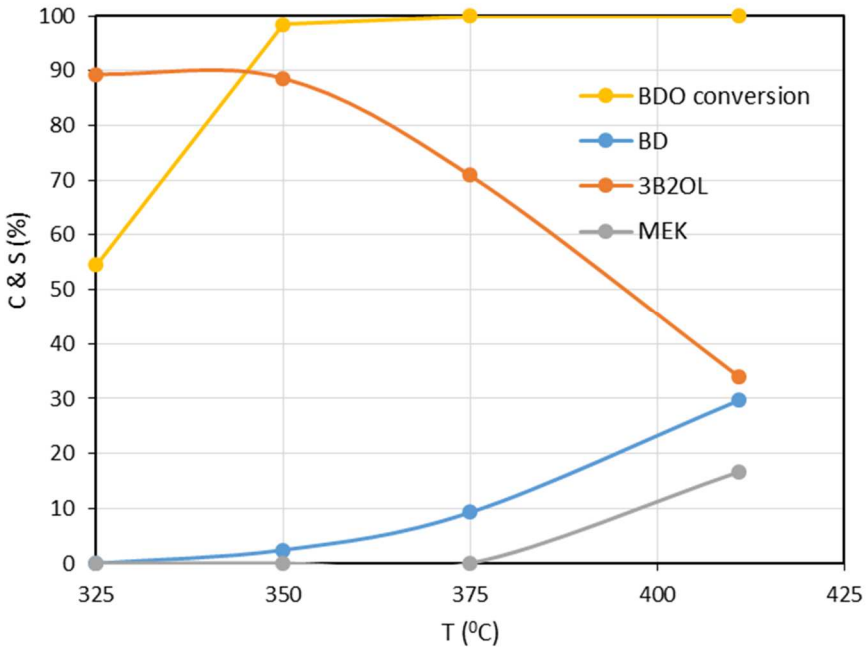

Figure 6-5. BDO dehydration over 1g Sc_2O_3, carrier gas H_2 is 46 mL/min, BDO feed rate is 0.018 mL/min.

Figure 6-6 shows the BDO dehydration over a double-bed catalyst system of Sc_2O_3 +Al_2O_3 at different temperatures. Note that both catalysts were physically in the same reactor tube, so their temperatures were essentially the same. The measured BDO conversions were 100% for all the conditions. Figure 6-5 shows that the two main products at all temperatures are

`

BD and MEK and that temperature impacts the relative amounts of both. There is an optimal reaction temperature for BD selectivity. At 318 °C, the BD selectivity is lower than MEK. This can be explained by comparing the results for the single and dual catalyst beds. As seen in Figure 6-5, there is incomplete conversion of BDO over Sc_2O_3 at temperatures below 350 °C. For this reason, when the dual catalyst bed system is used at low temperatures, unreacted BDO is mostly converted to MEK by Al_2O_3 [106], leading to higher MEK selectivity at 318 °C. At 350 °C, the single Sc_2O_3 bed achieves complete BDO conversion with 90% selectivity to 3B2OL. Therefore, the primary role of the Al_2O_3 bed is to convert 3B2OL to BD, resulting in high selectivity to BD. As the temperature further increased to 375 °C and 400 °C, BD selectivity slightly decreased as more heavy species such as 2,5-dimethylphenol are formed due to high temperatures that increase the potential of side reactions.

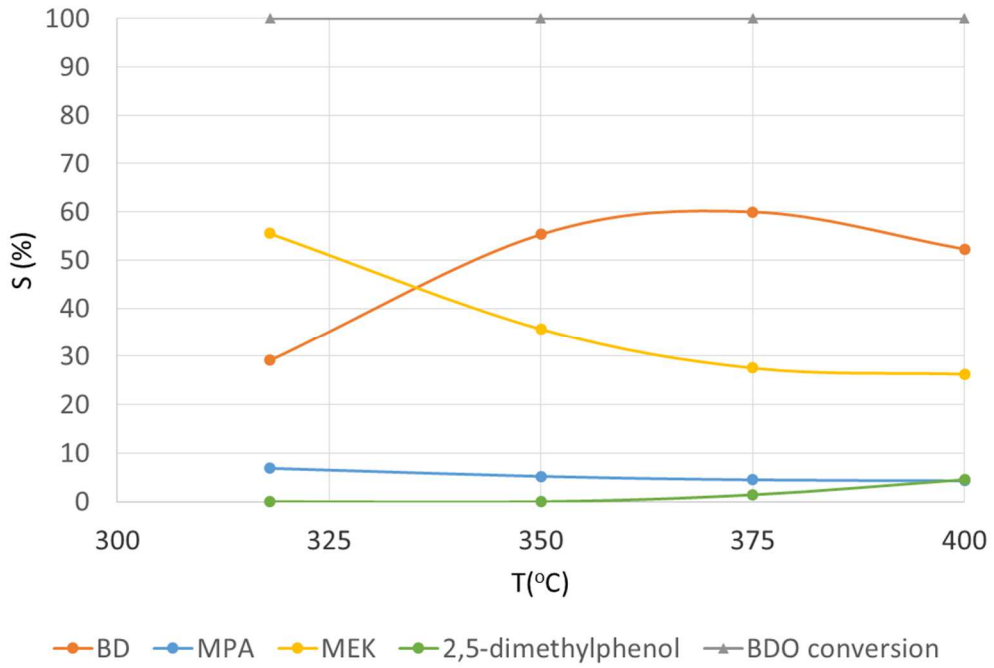

Figure 6-6. BDO dehydration over Sc_2O_3 + Al_2O_3 as a function of reaction temperature, carrier gas H_2 is 80 mL/min, BDO feed rate is 0.018 mL/min.

The BDO dehydration results over a double-bed Sc_2O_3+SiAl system at 318, 350, 375 and 400 °C are shown in Figure 6-7. This figure shows there is an optimal reaction temperature for BD selectivity. At 318 °C, the BD selectivity is lower than MEK, for the same reason as

`

described above: the acidic catalyst in the second bed converts unreacted BDO from the first bed mostly into MEK instead of BD. As the temperature increased to 350 °C, BD selectivity continuously increased to 60% with the maximum value 61.9%. As the reaction temperature further increased to 375 and 400 °C, the BD selectivity slightly decreased as other products (notably 2,5-dimethylphenol and MEK) are formed. Comparing the results to BDO dehydration over Sc_2O_3 + Al_2O_3, similar trends can be found on Sc_2O_3+SiAl. The highest BD selectivity is about 60% which is also found at 350 °C and the BD selectivity slightly dropped as the temperature further increased to 375 and 400 °C. The BDO conversion is 100% for all the conditions.

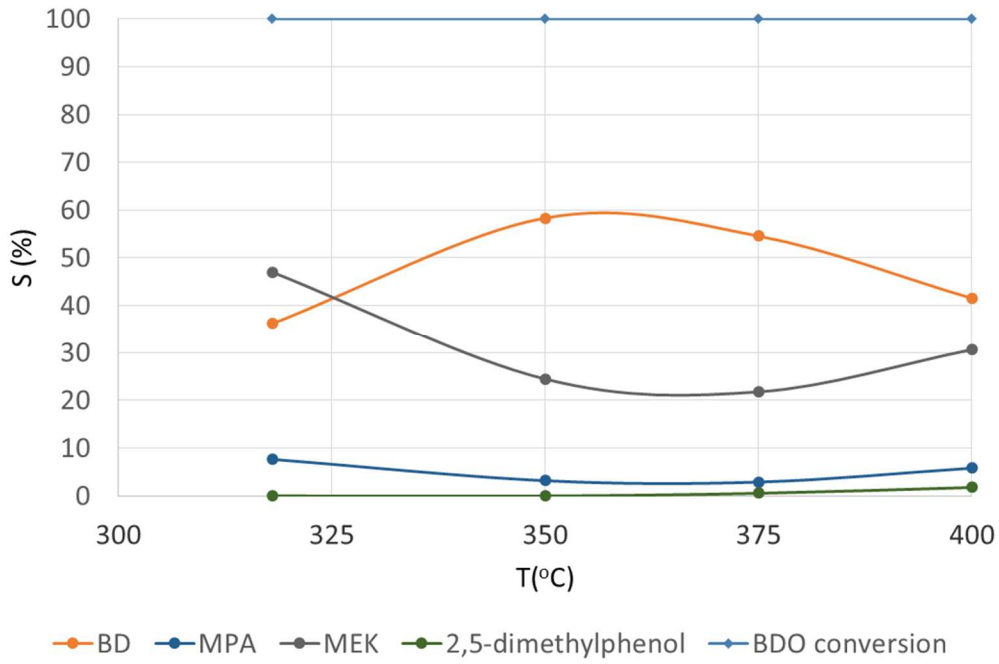

Figure 6-7. BDO dehydration over Sc_2O_3+SiAl as a function of reaction temperature, carrier gas H_2 is 80 mL/min, BDO feed rate is 0.018 mL/min.

Figure 6-8 shows the results for BDO dehydration over the Sc_2O_3 + $Ca_{0.04}Zr$ at 318, 350, 375 and 400 °C. The BD selectivity is zero at 318 °C while the BD selectivity increases as the reaction temperature increases. The highest average BD selectivity is about 43% at 400 °C. It is interesting to notice that the dehydrogenation product acetoin is formed with a selectivity of around 17% at 318 °C, while its selectivity is zero at higher temperatures. The 3B2OL selectivity is about 40% at 318 and 350 °C, however the selectivity decrease as the temperature increases to

`

375 °C and 400 °C. For 2,5-dimethylphenol, the selectivity is initially about 6% at 318 C and the selectivity increases to 12% at 350 °C, then as the temperature increases further, the selectivity decreases, falling to zero at 400 °C.

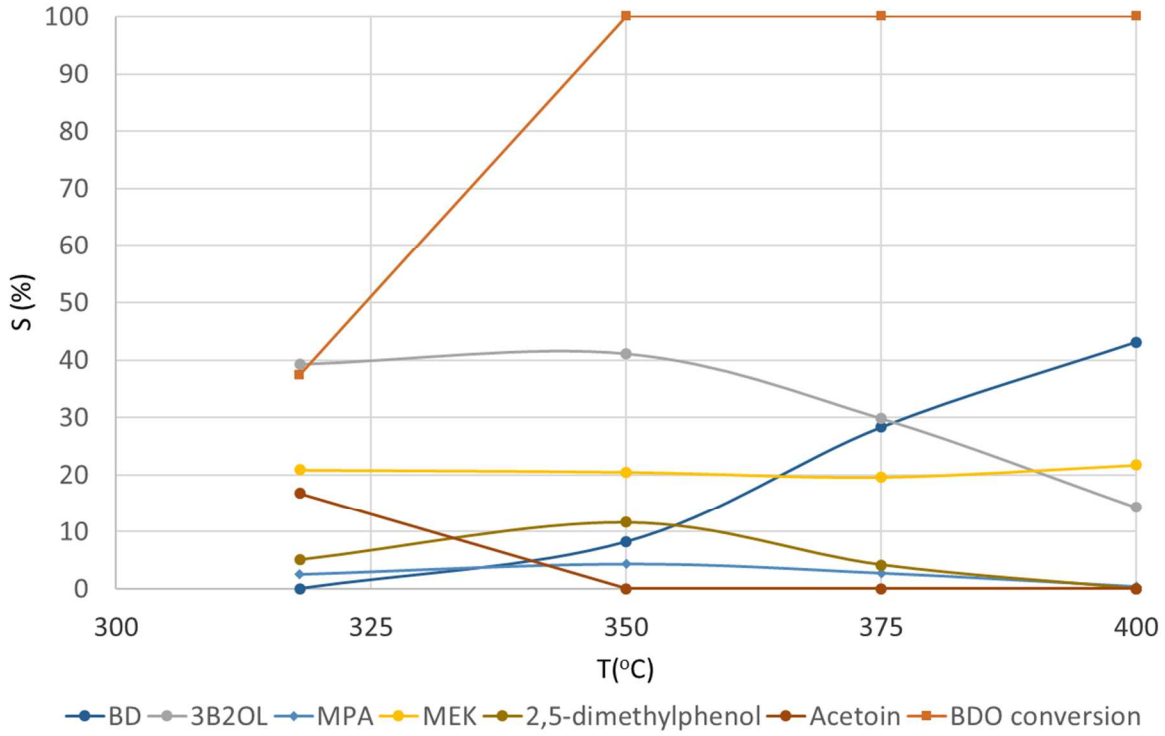

Figure 6-8. BDO dehydration over Sc_2O_3+$Ca_{0.04}Zr$ as a function of reaction temperature, carrier gas H_2 is 80 mL/min, BDO feed rate is 0.018 mL/min.

Figure 6-9 shows that the BDO dehydration over Sc_2O_3+$Ce_{0.1}Zr$ at 318, 350, 375 and 400 °C. The 3B2OL selectivity is about 28% at 318 and 350 °C, but as the temperature increases, the selectivity decreases significantly. BD selectivity is at its highest of ~18% at 375 °C. The 2,5-dimethylphenol selectivity is highest at ~7% at 318 °C and as the temperature increases, the selectivity gradually decreases.

`

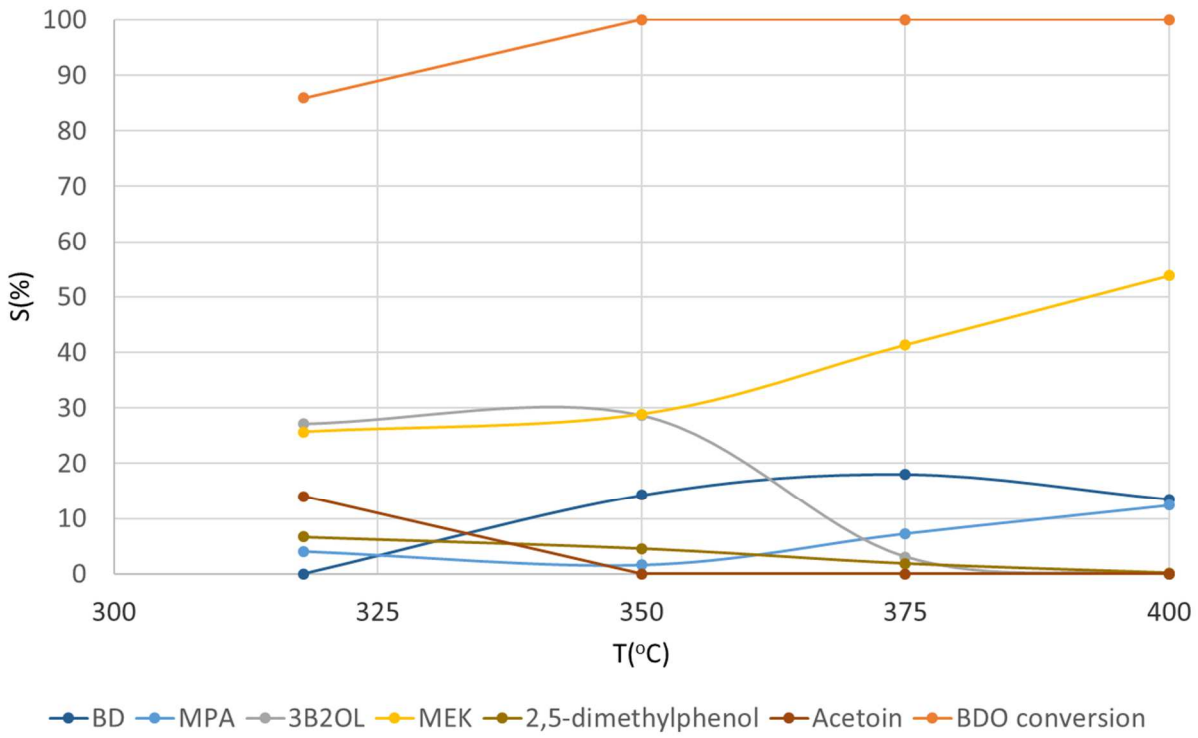

Figure 6-9. BDO dehydration over Sc_2O_3+$Ce_{0.1}Zr$ as a function of reaction temperature, carrier gas H_2 is 80 mL/min, BDO feed rate is 0.018 mL/min.

Figure 6-10 shows the BDO dehydration over Sc_2O_3+$Ce_{0.2}Zr$. The 3B2OL selectivity at 318 ^oC and 350 ^oC are 30% and 17% at respectively. At higher temperatures, 3B2OL is not observed. The BD selectivity is highest ~21% at 375 ^oC. The 2,5-dimethylphenol has the highest selectivity of 9% at 318 ^oC and the selectivity decreases as the temperature further increases.

`

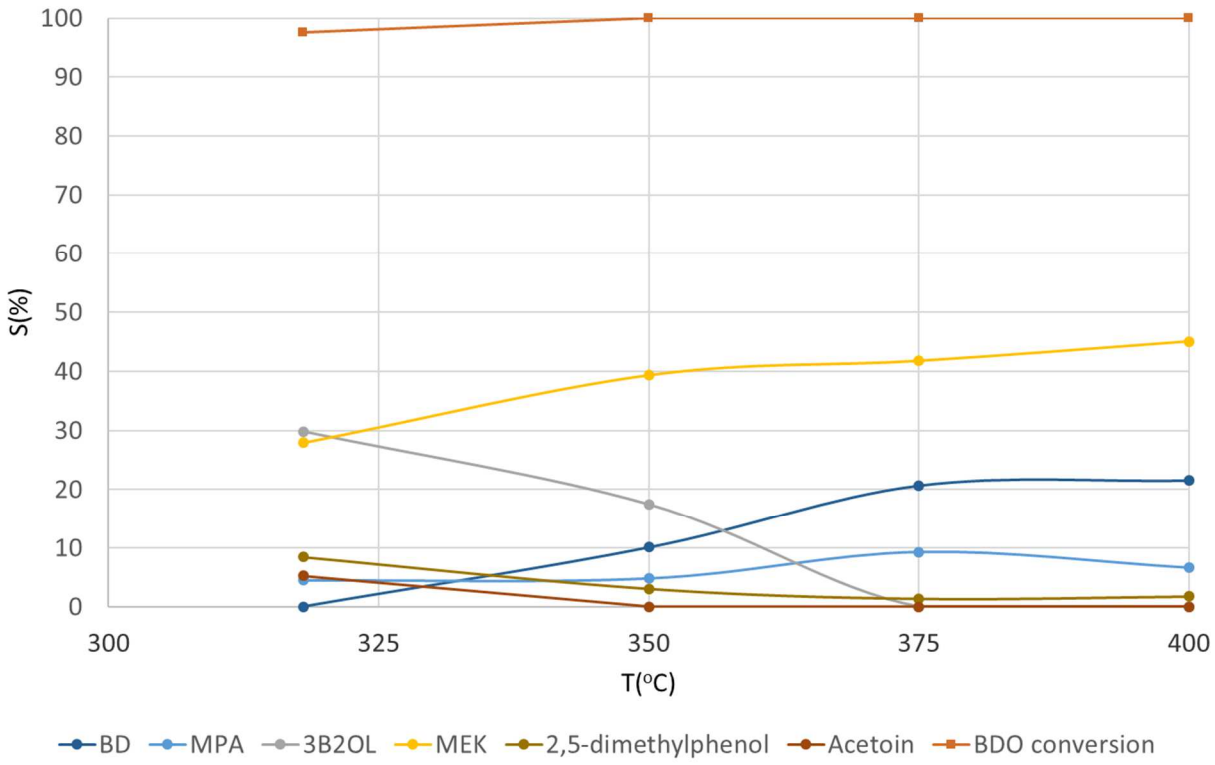

Figure 6-10. BDO dehydration over Sc_2O_3+$Ce_{0.2}Zr$ as a function of reaction temperature, carrier gas H_2 is 80 mL/min, BDO feed rate is 0.018 mL/min.

Figure 6-11 shows the BDO dehydration over the Sc_2O_3+$Ce_{0.19}Zr$ at 318, 350, 375 and 400 °C. The 2,5-dimethylphenol selectivity is zero at 318 °C but it increases to 4% at 350 °C. As temperature increase further, the 2,5-dimethylphenol selectivity decreases. The highest BD selectivity is about 23% at 400 °C. 3B2OL selectivity is greatly reduced as the temperature increases, while the MEK and BD selectivities increase as the temperature increase. These results are consistent with the results of BDO dehydration over a single-bed Sc_2O_3 shown in Figure 6-5 where temperature had a huge impact on the product distribution.

`

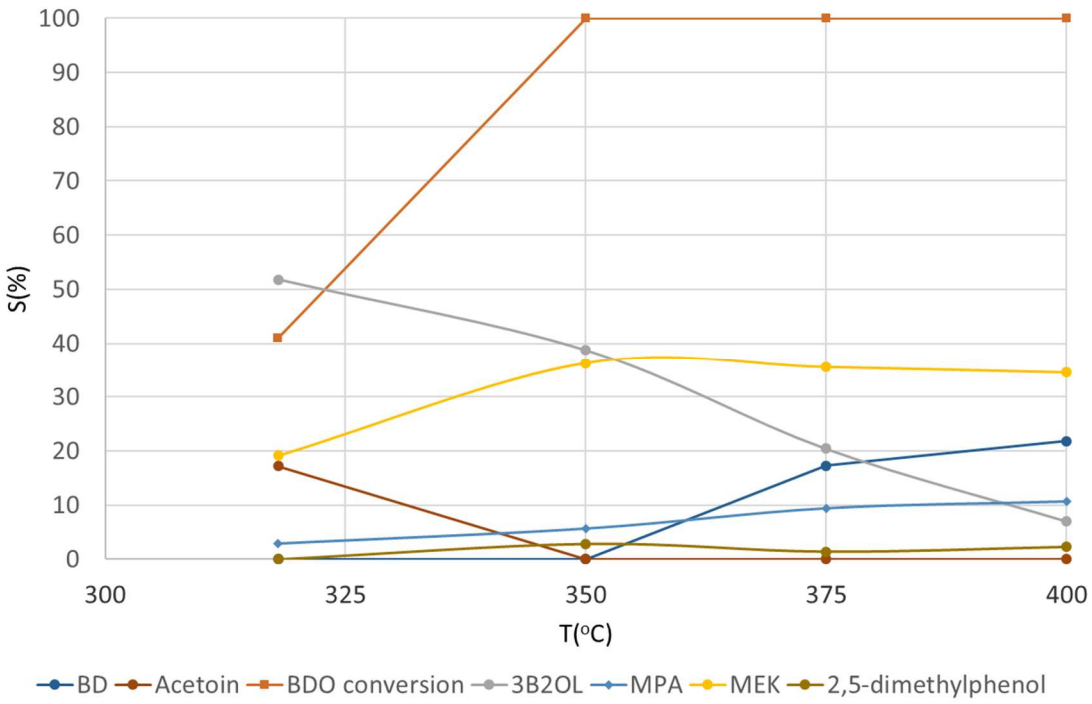

Figure 6-11. BDO dehydration over Sc_2O_3+$Ce_{0.19}Zr$ as a function of reaction temperature, carrier gas H_2 is 80 mL/min, BDO feed rate is 0.018 mL/min.

6.3.3. Comparison of Catalysts

Figure 6-12 compares the selectivity of all two-bed systems to the main products. It is easy to see that zirconia is not an optimal catalyst to convert the 3B2OL to BD when compared to acid catalyst Al_2O_3 or SiAl. Interestingly, 2,5-dimethylphenol is formed in significant amounts when the zirconia catalysts was used as the second bed catalyst. Notably, when $Ca_{0.04}Zr$ was used as the catalyst for the second bed, the highest selectivity to 2,5-dimethylphenol (12%) was achieved at 350 °C. The 2,5-dimethylphenol selectivities are higher over $Ca_{0.04}Zr$ and $Ce_{0.2}Zr$. This is likely because they possess strong basic sites compare to the other two zirconia samples as shown in Figure 6-3-b. The zirconia catalysts produce a significant amount of other species (shown as “Others” in Figure 6-12), that includes acetone, butene, MPA, MPO, 2-buten-1-ol and heavy species.

`

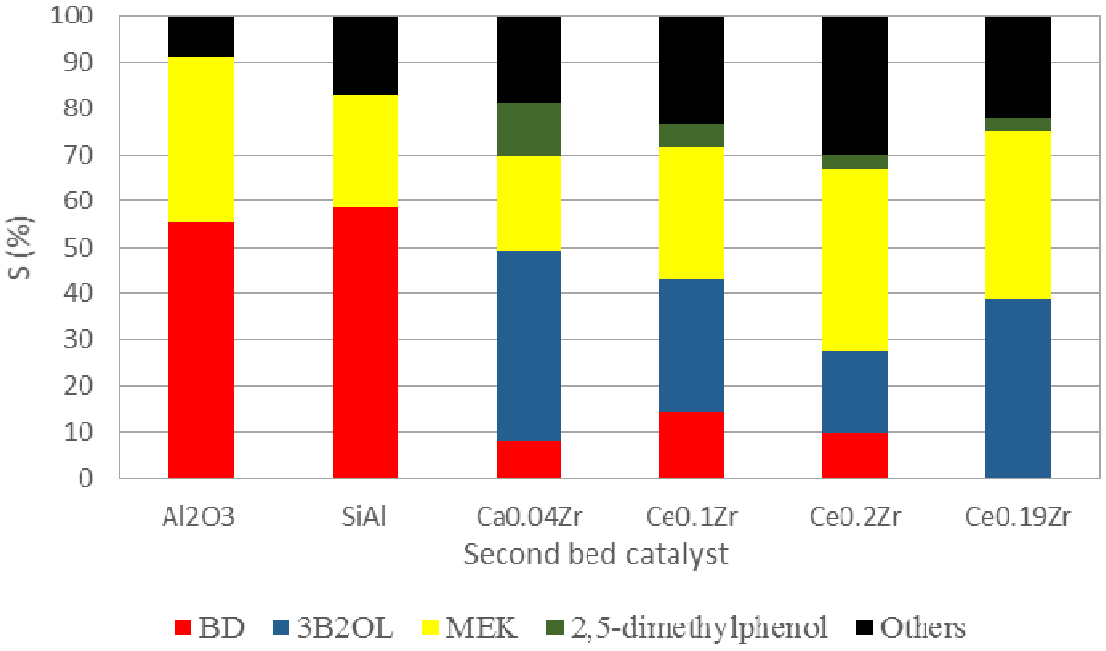

Figure 6-12. Selectivity of all two-bed systems in the conversion of BDO at 350 ºC.

Our results indicate that 2,5-dimethylphenol is not directly produced from BDO. The maximum 2,5-dimethylphenol selectivities for the two-bed catalytic systems were produced at 350 ºC. At this temperature, the first catalytic bed (Sc_2O_3) has converted all BDO to other products (Figure 6-5). For this reason, an intermediate species formed from BDO must be responsible for 2,5-dimethylphenol production.

To further investigate the reaction pathways to 2,5-dimethylphenol, experiments were conducted where BDO was reacted on all four zirconia catalysts for a range of residence times (2.4-2.81 seconds). Differences in results for different residence times can provide information on possible intermediates. Figure 6-13 shows the results of these experiments, conducted at 318ºC. The analysis of the product distributions as functions of temperature (Figure 6-8-11) indicates that 3B2OL is a possible intermediate for 2,5-dimethylphenol formation. The 3B2OL concentration only shows a maximum on $Ce_{0.2}Zr$ while the concentration monotonically increases or decreases on the other three zirconia samples. For $Ca_{0.04}Zr$ and $Ce_{0.2}Zr$, acetoin concentration increases to the maxmium then drop as the residence time increase. Meanwhile, BDO concentration decreases and the 2,5-dimethylphenol selectivity continuously increases as the residence time increases. This implies that acetoin is a likely intermediate to produce 2,5-

`

dimethylphenol on these catalysts. Figure 6-13-c shows BDO dehydration over $Ce_{0.1}Zr$. The 2,5-dimethylphenol concentration still increases with residence time, while the 3B2OL and acetoin concertation continuously decrease with residence time. Figure 6-13-d shows the BDO dehydration over $Ce_{0.19}Zr$. The BDO concentration still decrease with residence time. However, it is interesting to notice that the 2,5-dimethylphenol concentration is zero at all the residence time. This is consistent with Figure 6-11 that shows that the 2,5-dimethylphenol concentration is zero over the two-bed catalyst Sc_2O_3+ $Ce_{0.19}Zr$. In addition, the acetoin selectivity continously increases with residence time which is different from the other zirconia catalyst. A possible explanation is that this catalyst may not be active for converting acetoin to 2,5-dimethylphenol. Generally, 2,5-dimethylphenol selectivity was maximized at lower temperatures. As the temperature further increased, the 2,5-dimethylphenol decreased.

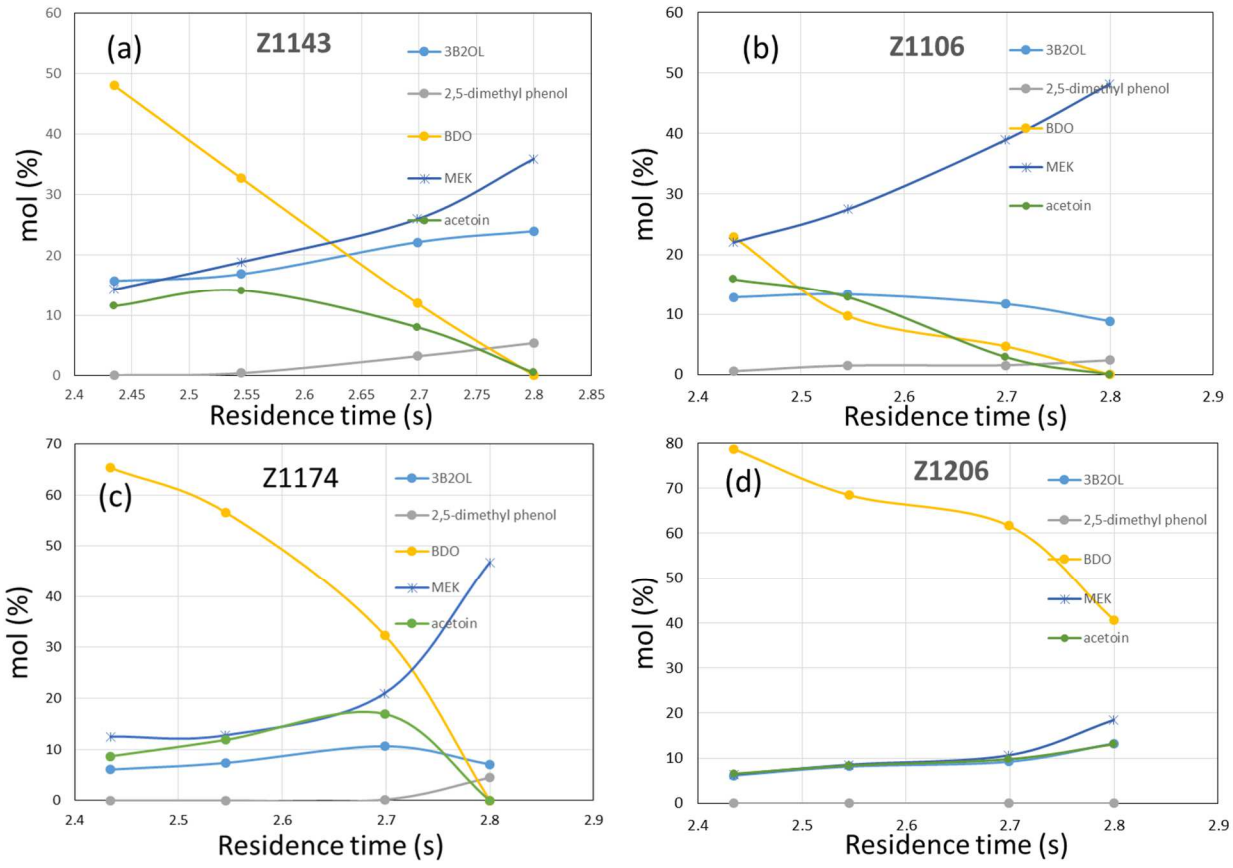

Figure 6-13. BDO dehydration over a 1g single-bed Z1143= $Ca_{0.04}Zr$ (a), Z1174= $Ce_{0.2}Zr$ (b), Z1106= $Ce_{0.1}Zr$ (c) and Z1206= $Ce_{0.19}Zr$ (d) at 318 ºC.

`

To further investigate which species is the intermediate in the production of 2,5-dimethyl phenol, experiments were conducted where different potential intermediates were reacted over two of the zirconia catalysts. Table 6-2 shows the 2,5-dimethylphenol selectivity of MVK, 3B2OL and acetoin react over catalyst $Ca_{0.04}Zr$ and $Ce_{0.2}Zr$. This results show that acetoin can be converted to 2,5-dimethylphenol, but also shows that MVK and 3B2OL can also be converted to 2,5-dimethylphenol. It is important to note that the three intermediates can be converted from one to the other. For example, acetoin can be dehydrated to form MVK. For the experiment reported in Table 6-2 for acetoin, $Ca_{0.04}Zr$ produced almost 15% MVK and $Ce_{0.2}Zr$ produced nearly 39%. While MVK production from 3B2OL is not observed. These results indicate that more than one of the C4 oxygenates can be converted to 2,5-dimethylphoneol. It is also interesting to note that the 2,5-dimethylphenol selectivity over $Ca_{0.04}Zr$ is higher than that over $Ce_{0.2}Zr$, which is consistent with the results that the maximum 2,5-dimethylphenol selectivity of BDO as reactant is on catalyst $Ca_{0.04}Zr$.

Table 6-2. 2,5-dimethylphenol selectivity of MVK, 3B2OL and acetoin react over $Ca_{0.04}Zr$ and $Ce_{0.2}Zr$.

2,5-dimethylphenol Selectivity (%)	Catalyst	
Reactant	$Ca_{0.04}Zr$	$Ce_{0.2}Zr$
MVK	18.94	11.10
3B2OL	15.67	6.46
Acetoin	27.92	16.71

6.3.4. Reaction Mechanism

The mechanism for BDO conversion to different products has been discussed in a few different papers [20, 106]; however, previous papers have not reported the formation of aromatic phenols, as is shown in this work. Figure 6-14 shows the main reaction pathways of BDO in this paper. BDO dehydration readily occurs on acid catalysts to form MEK. Some catalysts, notably Sc_2O_3, can dehydrate BDO to 3B2OL, which can then be further dehydrated to form BD [106]. Alternatively, BDO can be dehydrogenated to form acetoin, which can further be dehydrated to

`

MVK. If sufficiently strong basic sites are present, MVK can further be converted to acetone and formaldehyde via the retro-aldol condensation reaction [106].

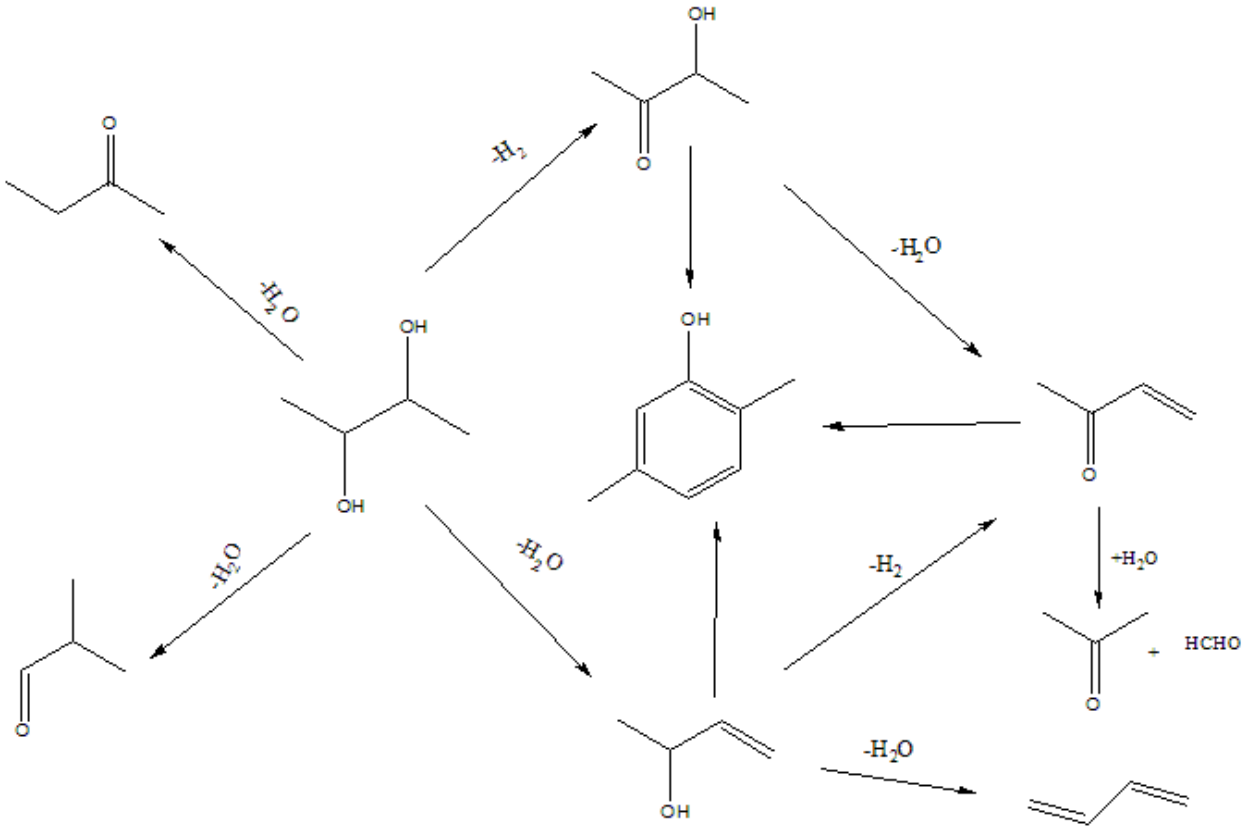

Figure 6-14. Proposed reaction pathways of BDO conversion and 2,5-dimethylphenol formation.

The mechanism of 2,5-dimethylphenol formation currently not clear. One possible explanation is the Diels-Alder reaction between BD and an unsaturated C4 such as MVK or 3B2OL to form C8. However, in the reaction of MVK and acetoin over $Ca_{0.04}Zr$ and $Ce_{0.2}Zr$, BD is not observed, while the 2,5-dimethylphenol is stilled produced. This indicates that the Diels-Alder reaction is not the best explanation for 2,5-dimethylphenol formation. Another more likely explanation are condensation reactions between C4 oxygenates. Figure 6-15 illustrates one such route, where acetoin and 3B2OL are coupled over a basic catalyst. A key step in this scheme is the nucleophilic attack that leads to condensation of the two molecules to form a C8 molecule. Once a C8 molecule has been produced, an intramolecular Michael addition can then produce a ring structure. Dehydration and dehydrogenation steps result in the aromatic product, then via methyl group migration, 2,5-dimehtylphenol can be formed. Figure 6-15 is meant to represent one possible way the substituted phenol can be produced. Another possibility is the reaction of a

`

C4 oxygenate with MVK. Unsaturated ketones like MVK can be attacked by a nucleophile in the Michael addition reaction [125], so this pathway would be expected to occur readily over basic catalysts.

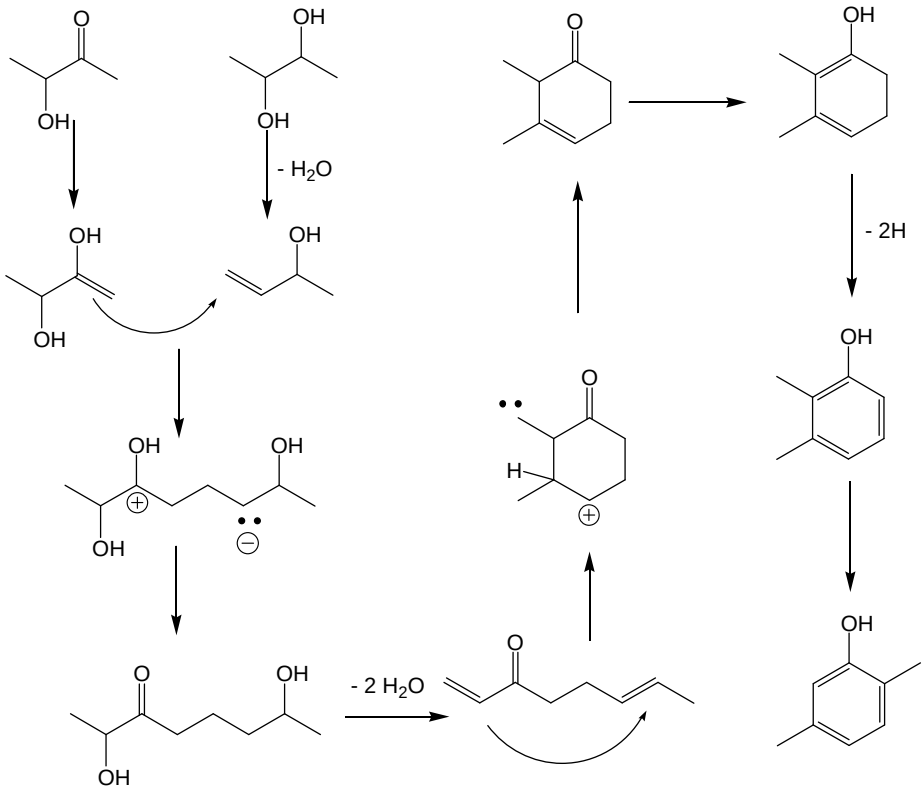

Figure 6-15. 2,5-dimethylphenol formation mechanism.

Implicit in the discussion of how 2,5-dimethylphenol is formed is the importance of the nature of the catalyst. As shown in Figure 6-12, the acidic metal oxides did not form 2,5-dimethylphenol, instead favoring dehydration of 3B2OL to BD. Only when Ca- and Ce-modified zirconia were used was the substituted phenol produced. These materials have sufficient basicity to favor Michael addition reactions. In addition, materials with more basic sites ($Ca_{0.04}Zr$ and $Ce_{0.2}Zr$) produce more 2,5-dimethylphenol, supporting the hypothesis that strong base sites are needed for the condensation reactions responsible for 2,5-dimethylphenol production.

6.4. Conclusion

Dehydration of BDO was investigated over two-bed catalyst systems, Sc_2O_3+Al_2O_3, Sc_2O_3+silica-alumina and Sc_2O_3+zirconia, at temperatures between 300 ^oC and 400 ^oC. The product selectivities were greatly impacted by acid/base properties of the second bed catalyst.

`

BD selectivity was enhanced by using acidic alumina and silica-alumina as the second bed catalyst which favor the dehydration. When the zirconia used as the second bed catalyst, the BD selectivity decreased, while the 2,5-dimethylphenol was formed which is due to the strong basic site favors condensation reactions over dehydration. This study also indicated that MVK, 3B2OL and acetoin are the possible intermediates for the BDO conversion into 2,5-dimethylphenol.

`

Chapter 7 - Future work

For the future work, it includes two parts:

1: Modeling of Three-way Catalytic Converter

a. The 115-step microkinetic mechanism can be reduced using the sensitivity analysis method, a more compacted mechanism including important reaction steps can be proposed. This will greatly reduce the computation time.
b. External mass transfer limitation should be considered both in the PFR model and tanks-in-series model.
c. Energy balance will be considered to include the temperature effect on the TWC performance.

2: BDO conversion

a. Triethylamine in-situ modification process can be replaced by ethylamine, diethylamine and other common acid or base gas such as CO_2 and NH_3 to further prove the triethylamine change the alumina acid/base properties during the in-situ modification process.
b. 2,5-dimethylphenol formation mechanism is still not clear, MVK, 3B2OL and acetoin are the possible intermediates. More intermediates study is need to find out the reaction pathway step by step.
c. Zirconia with strong basic sites seems to promote the 2,5-dimethylphenol formation, zirconia doped with basic oxide such as CeO_2 and MgO can increase the basic site strength [121] which is possible to further improve the 2,5-dimethylphenol selectivity.

`

References

[1] Recognizing the Best in Innovation: Breakthrough Catalyst, R&D Magazine (September 2005) p. 20.

[2] ExxonMobile, http://corporate.exxonmobil.com/en/energy/energy-outlook, (2015) .

[3] M.A. Toema, Physics-based characterization of lambda sensor output to control emissions from natural gas fueled engines PhD diss. Kansas State University (2010) .

[4] Bosch Oxygen Sensor Catalog.

[5] M. Defoort, D. Olsen, B. Willson, Int. J. Eng. Res. 5 (2004) 115.

[6] X. Shi, R. Seiser, J. Chen, R. Dibble, R. Cattolica, SAE International Journal of Engines 8 (2015) 1246.

[7] IARC Working Group, IARC monographs on the evaluation of carcinogenic risks to humans 100F (2012) 309.

[8] M. Winfield, J. Counc. Sci. Ind. Res. 18 (1945) 412.

[9] M.M. Bomgardner, Chem. Eng. News 89 (2011) 18.

[10] N.B. Jansen, G.T. Tsao, Adv. Biochem. Eng. Biotechnol. 27 (1983) 85.

[11] W. White, Chem. Biol. Interact. 166 (2007) 10.

[12] R.R. Emerson, M.C. Flickinger, G.T. Tsao, Ind. Eng. Chem. Prod. Res. Dev. 21 (1982) 473.

[13] W. Zhang, D. Yu, X. Ji, H. Huang, Green Chem. 14 (2012) 3441.

[14] A. Bourns, R. Nicholls, Can. J. Res. 25 (1947) 80.

[15] N. Shlechter, D. Othmer, S. Marshak, Ind. Eng. Chem. 37 (1945) 900.

[16] N. Shlechter, D. Othmer, R. Brand, Ind. Eng. Chem. 37 (1945) 905.

[17] H. Duan, D. Sun, Y. Yamada, S. Sato, Catal. Commun. 48 (2014) 1.

[18] H. Duan, Y. Yamada, S. Sato, Chem. Lett. 43 (2014) 1773.

`

[19] H. Duan, Y. Yamada, S. Sato, Appl. Catal. A 487 (2014) 226.

[20] H. Duan, Y. Yamada, S. Sato, Appl. Catal. A 491 (2015) 163.

[21] G.C. Koltsakis, A.M. Stamatelos, Prog. Energy Combust. Sci. 23 (1997) 1.

[22] J. Koop, O. Deutschmann, Appl. Catal. B 91 (2009) 47.

[23] D. Chatterjee, O. Deutschmann, J. Warnatz, Faraday Discuss. 119 (2002) 371.

[24] M. Shelef, R.W. McCabe, Catal. Today 62 (2000) 35.

[25] A. Trovarelli, Catal. Rev. 38 (1996) 439.

[26] P. Kumar, I. Makki, J. Kerns, K. Grigoriadis, M. Franchek, V. Balakotaiah, Chem. Eng. Sci. 73 (2012) 373.

[27] G.C. Koltsakis, A.M. Stamatelos, Chem. Eng. Sci. 54 (1999) 4567.

[28] R. Burch, D. Crittle, M. Hayes, Catal. Today 47 (1999) 229.

[29] P. Gélin, M. Primet, Appl. Catal. B 39 (2002) 1.

[30] G. Groppi, C. Cristiani, L. Lietti, P. Forzatti, Stud. Surf. Sci. Catal. 130 (2000) 3801.

[31] J.B. Miller, M. Malatpure, Appl. Catal. A 495 (2015) 54.

[32] A. Trinchero, A. Hellman, H. Grönbeck, Surf. Sci. 616 (2013) 206.

[33] M.M. Souza, M. Schmal, Appl. Catal. A 281 (2005) 19.

[34] P. Torniainen, X. Chu, L. Schmidt, J. Catal. 146 (1994) 1.

[35] I. Wierzba, A. Depiak, Int. J. Hydrog. Energy 29 (2004) 1303.

[36] R. Burch, P. Loader, Appl. Catal. B 5 (1994) 149.

[37] M. Lyubovsky, L.L. Smith, M. Castaldi, H. Karim, B. Nentwick, S. Etemad, R. LaPierre, W.C. Pfefferle, Catal. Today 83 (2003) 71.

[38] O. Buyevskaya, D. Wolf, M. Baerns, Catal. Lett. 29 (1994) 249.

[39] D. Hickman, L.D. Schmidt, AIChE J. 39 (1993) 1164.

`

[40] O. Deutschmann, R. Schwiedemoch, L.I. Maier, D. Chatterjee, Stud. Surf. Sci. Catal. 136 (2001) 251.

[41] R. Schwiedernoch, S. Tischer, C. Correa, O. Deutschmann, Chem. Eng. Sci. 58 (2003) 633.

[42] A. Mhadeshwar, D. Vlachos, Ind. Eng. Chem. Res. 46 (2007) 5310.

[43] R. Burch, P. Millington, Catal. Today 26 (1995) 185.

[44] S. Poulston, R.R. Rajaram, Catal. Today 81 (2003) 603.

[45] H. Abdulhamid, E. Fridell, M. Skoglundh, Appl. Catal. B 62 (2006) 319.

[46] I. Nova, L. Lietti, L. Castoldi, E. Tronconi, P. Forzatti, J. Catal. 239 (2006) 244.

[47] I. Nova, L. Lietti, P. Forzatti, Catal. Today 136 (2008) 128.

[48] T. Szailer, J.H. Kwak, D.H. Kim, J.C. Hanson, C.H. Peden, J. Szanyi, J. Catal. 239 (2006) 51.

[49] R. Burch, J. Breen, F. Meunier, Appl. Catal. B 39 (2002) 283.

[50] S.Y. Joshi, M.P. Harold, V. Balakotaiah, Chem. Eng. Sci. 65 (2010) 1729.

[51] E.N. Fuller, P.D. Schettler, J.C. Giddings, Ind. Eng. Chem. 58 (1966) 18.

[52] S.Y. Joshi, Y. Ren, M.P. Harold, V. Balakotaiah, Appl. Catal. B 102 (2011) 484.

[53] L. Mukadi, R. Hayes, Comput. Chem. Eng. 26 (2002) 439.

[54] H. Yao, Y.Y. Yao, J. Catal. 86 (1984) 254.

[55] J. Xu, R. Clayton, V. Balakotaiah, M.P. Harold, Appl. Catal. B 77 (2008) 395.

[56] J. Vajo, W. Tsai, W. Weinberg, J. Phys. Chem. 89 (1985) 3243.

[57] P. Aghalayam, Y.K. Park, N. Fernandes, V. Papavassiliou, A. Mhadeshwar, D.G. Vlachos, J. Cata. 213 (2003) 23.

[58] M. Maestri, D.G. Vlachos, A. Beretta, G. Groppi, E. Tronconi, AIChE J. 55 (2009) 993.

`

[59] N.V. Heeb, A. Forss, S. Brühlmann, R. Lüscher, C.J. Saxer, P. Hug, Atmos. Environ. 40 (2006) 5986.

[60] A.B. Mhadeshwar, H. Wang, D.G. Vlachos, J. Phys. Chem. B 107 (2003) 12721.

[61] M. Salciccioli, M. Stamatakis, S. Caratzoulas, D.G. Vlachos, Chem. Eng. Sci. 66 (2011) 4319.

[62] P. Gokulakrishnan, P. McLellan, A. Lawrence, E. Grandmaison, Chem. Eng. Sci. 60 (2005) 3683.

[63] S. Vajda, P. Valko, T. Turanyi, Int. J. Chem. Kinet. 17 (1985) 55.

[64] C. In, S. Kim, C. Kim, W. Cho, SAE Technical Paper (1997) 207.

[65] M. Ishii, S. Ishizawa, E. Inada, R. Idoguchi, T. Sekiba, SAE Technical Paper 942005 (1994) 125.

[66] S.J. Curran, R.M. Wagner, R.L. Graves, M. Keller, J.B. Green, Energy 75 (2014) 194.

[67] B.K. Cho, Ind. Eng. Chem. Res. 27 (1988) 30.

[68] F. Zeng, K.L. Hohn, Appl. Catal. B 182 (2016) 570.

[69] H.S. Fogler, Elements of chemical reaction engineering, 3rd Edition, Prentice-Hall, 1999.

[70] M. Balenovic, Modelling and Model-based Control of a Three-way Catalytic Converter PhD diss. Technische Universiteit Eindhoven (2002) .

[71] A. Demirbaş, Energy Convers. Manag. 42 (2001) 1357.

[72] M. Kopke, C. Mihalcea, F. Liew, J.H. Tizard, M.S. Ali, J.J. Conolly, B. Al-Sinawi, S.D. Simpson, Appl. Environ. Microbiol. 77 (2011) 5467.

[73] U. Kim, H. Lee, Patent 10-2012-0099818 (2012) .

[74] T.Y. Kim, J. Baek, C.K. Song, Y.S. Yun, D.S. Park, W. Kim, J.W. Han, J. Yi, J. Catal. 323 (2015) 85.

`

[75] V. Díez, P. Torresi, P. Luggren, C. Ferretti, J. Di Cosimo, Catal. Today 213 (2013) 18.

[76] X. Liu, R.E. Truitt, J. Am. Chem. Soc. 119 (1997) 9856.

[77] Y. Ono, H. Hattori, Solid base catalysis, Springer Heidelberg and Tokyo Inst. Tech., London, NY, 2011, p. 48.

[78] G. Kresse, J. Furthmüller, Phys. Rev. B 54 (1996) 11169.

[79] J.P. Perdew, K. Burke, M. Ernzerhof, Phys. Rev. Lett. 77 (1996) 3865.

[80] P.E. Blöchl, Phys. Rev. B 50 (1994) 17953.

[81] H.J. Monkhorst, J.D. Pack, Phys. Rev. B 13 (1976) 5188.

[82] G. Henkelman, B.P. Uberuaga, H. Jónsson, J. Chem. Phys. 113 (2000) 9901.

[83] G. Henkelman, H. Jónsson, J. Chem. Phys. 111 (1999) 7010.

[84] S. Grimme, J. Antony, S. Ehrlich, H. Krieg, J. Chem. Phys. 132 (2010) 154104.

[85] M. Auta, N.A. Darbis, A.M. Din, B. Hameed, Chem. Eng. J. 233 (2013) 80.

[86] C. Flego, W.O. Parker, Appl. Catal. A 185 (1999) 137.

[87] G. Colorio, J. Védrine, A. Auroux, B. Bonnetot, Appl. Catal. A 137 (1996) 55.

[88] T. Curtin, J. McMonagle, B. Hodnett, Appl. Catal. A 93 (1992) 91.

[89] T. Seki, M. Onaka, J. Mol. Catal. A 263 (2007) 115.

[90] X. Zhao, Y. Yue, Y. Zhang, W. Hua, Z. Gao, Catal. Lett. 89 (2003) 41.

[91] E.A. El-Katatny, S.A. Halawy, M.A. Mohamed, M.I. Zaki, Powder Technol 132 (2003) 137.

[92] G. Leofanti, M. Padovan, G. Tozzola, B. Venturelli, Catal. Today 41 (1998) 207.

[93] J. Sanchez-Valente, X. Bokhimi, F. Hernández, Langmuir 19 (2003) 3583.

[94] R.T. Morrison, R.N. Boyd, Organic Chemistry, 1963, p. 174.

[95] K. Nakamura, Y. Osamura, J. Am. Chem. Soc. 115 (1993) 9112.

`

[96] B.C. Lippens, J.J. Steggerda, in: B.G. Linsen (Ed.), Physical and Chemical Aspects of Adsorbents and Catalysts, Academic Press, London, New York, 1970, p. 189.

[97] H. Chen, H. Ji, AIChE J. 56 (2010) 466.

[98] M. Ai, J. Catal. 106 (1987) 273.

[99] P. Nortier, P. Fourre, A.M. Saad, O. Saur, J. Lavalley, Appl. Catal. 61 (1990) 141.

[100] J. Beaufils, Y. Barbaux, J. Chim. Phys. Phys. -Chim. Biol. 78 (1981) 347.

[101] S. Roy, G. Mpourmpakis, D. Hong, D.G. Vlachos, A. Bhan, R. Gorte, ACS Catal. 2 (2012) 1846.

[102] J.F. DeWilde, H. Chiang, D.A. Hickman, C.R. Ho, A. Bhan, ACS Catal. 3 (2013) 798.

[103] J. Joubert, A. Salameh, V. Krakoviack, F. Delbecq, P. Sautet, C. Copéret, J.M. Basset, J. Phys. Chem. B 110 (2006) 23944.

[104] S. Sato, F. Sato, H. Gotoh, Y. Yamada, ACS Catal. 3 (2013) 721.

[105] X. Ji, H. Huang, P. Ouyang, Biotechnol. Adv. 29 (2011) 351.

[106] Fan Zeng, William J. Tenn III, Sudhir N. V. K. Aki, Jiayi Xu, Bin Liu, and Keith L. Hohn, submit to Journal of Catalysis .

[107] W. Kim, W. Shin, K.J. Lee, H. Song, H.S. Kim, D. Seung, I.N. Filimonov, Appl. Catal. A 511 (2016) 156.

[108] W.J. Hale, Patent US Patent 2,400,409 (1946) .

[109] V. Zelenak, D. Halamova, L. Gaberova, E. Bloch, P. Llewellyn, Microporous Mesoporous Mater. 116 (2008) 358.

[110] H.Y. Huang, R.T. Yang, D. Chinn, C.L. Munson, Ind Eng Chem Res 42 (2003) 2427.

[111] S. Shylesh, D. Hanna, J. Gomes, S. Krishna, C.G. Canlas, M. Head-Gordon, A.T. Bell, ChemCatChem 6 (2014) 1283.

`

[112] J.D. Bass, A. Solovyov, A.J. Pascall, A. Katz, J. Am. Chem. Soc. 128 (2006) 3737.

[113] P. Hogan, J. Pašek, Collect. Czech. Chem. Commun. 38 (1973) 1513.

[114] A. Multer, N. McGraw, K. Hohn, P. Vadlani, Ind Eng Chem Res 52 (2012) 56.

[115] V. Solinas, E. Rombi, I. Ferino, M. Cutrufello, G. Colón, J. Navıo, J. Mol. Catal. A: Chem. 204 (2003) 629.

[116] E.L. Kunkes, E.I. Gürbüz, J.A. Dumesic, Journal of Catalysis 266 (2009) 236.

[117] U. Martin, H. Boysen, F. Frey, Acta Crystallogr., Sect B: Struct. Sci. 49 (1993) 403.

[118] A. Chatterjee, S. Pradhan, A. Datta, M. De, D. Chakravorty, J. Mater. Res. 9 (1994) 263.

[119] D. Kim, H. Jung, I. Yang, J. Am. Ceram. Soc. 76 (1993) 2106.

[120] A. Trovarelli, F. Zamar, J. Llorca, C. De Leitenburg, G. Dolcetti, J.T. Kiss, J. Catal. 169 (1997) 490.

[121] L. Vivier, D. Duprez, ChemSusChem 3 (2010) 654.

[122] G. Lafaye, J. Barbier, D. Duprez, Catal. Today 253 (2015) 89.

[123] Y. Li, D. He, Q. Zhu, X. Zhang, B. Xu, J. Catal. 221 (2004) 584.

[124] A. Martínez-Arias, M. Fernández-García, V. Ballesteros, L. Salamanca, J. Conesa, C. Otero, J. Soria, Langmuir 15 (1999) 4796.

[125] R.S. Conn, A.V. Lovell, S. Karady, L.M. Weinstock, J. Org. Chem. 51 (1986) 4710.

`

Appendix A - Supporting information

Molecular structures and potential energy surfaces on hydroxylated surfaces are shown in this Supporting Information document.

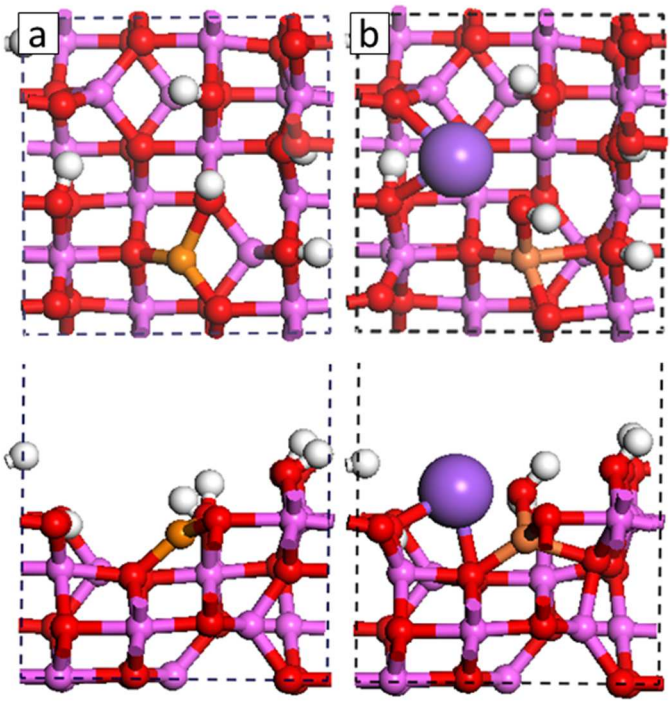

Figure A-1. Top and side views of relaxed hydroxylated pristine (a) and Na-doped (b) γ-Al_2O_3 (110) surfaces. The Al(III) site remains open, and the rest of the surface is hydroxylated with three dissociated water molecules. The Al(III) and Al(IV) sites are represented with gold and pink spheres respectively.

`

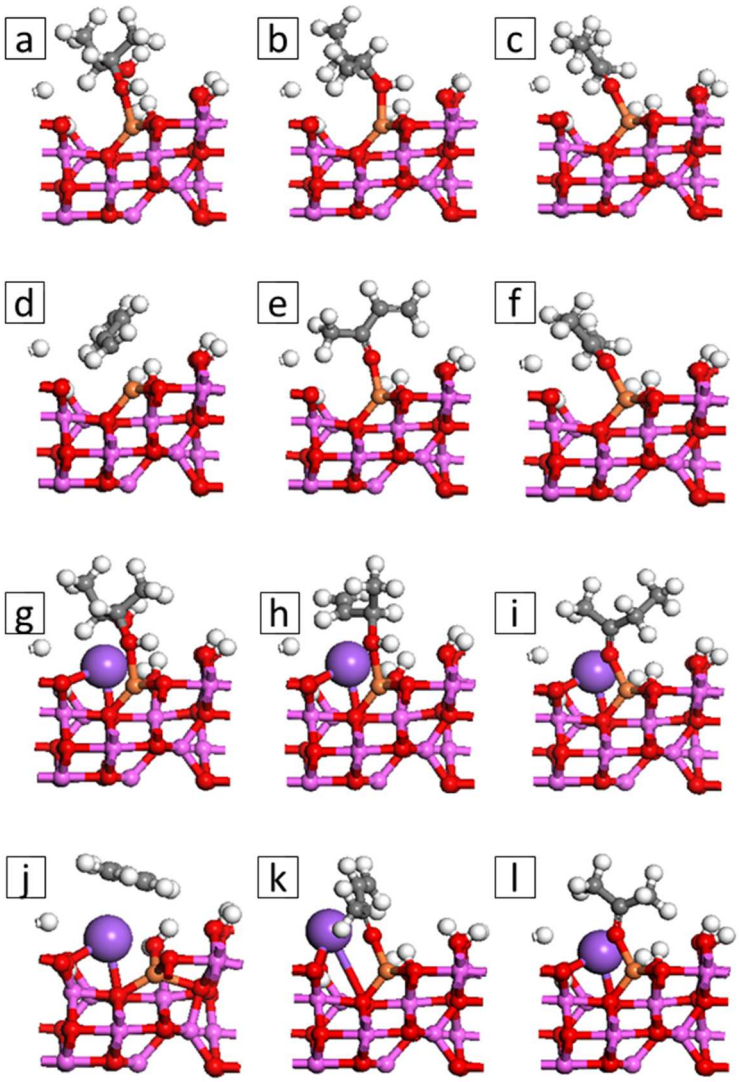

Figure A-2. (a-f) Optimized structures of BDO, 3B2OL, MEK, BD, MVK, and acetone on hydroxylated pristine γ-Al_2O_3 (110) surfaces; (g-l) on Na-modified γ-Al_2O_3 (110) surfaces. White, grey, red, pink, gold, and purple spheres represent the H, C, O, Al (IV), Al(III), and Na atoms, respectively.

`

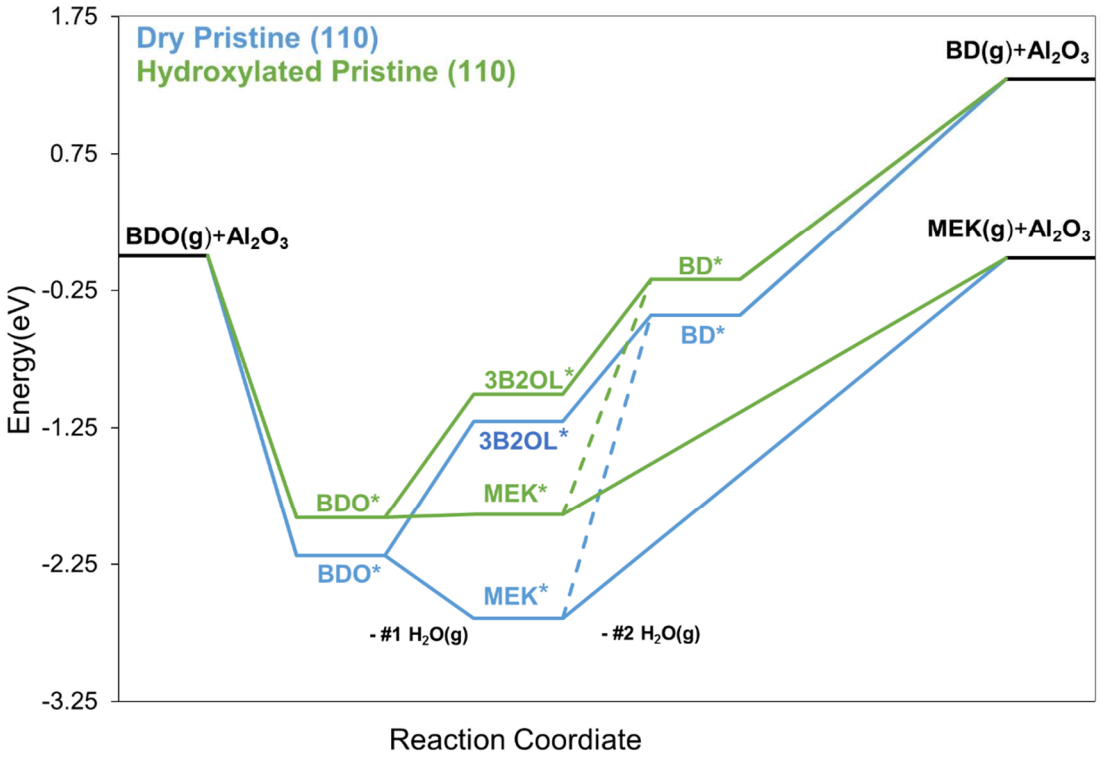

Figure A-3. Potential energies of the two-step BDO dehydration forming 3B2OL, MEK, and BD on dry and hydroxylated pristine γ-Al_2O_3 (110) surfaces. The asterisks represent surface species.

`

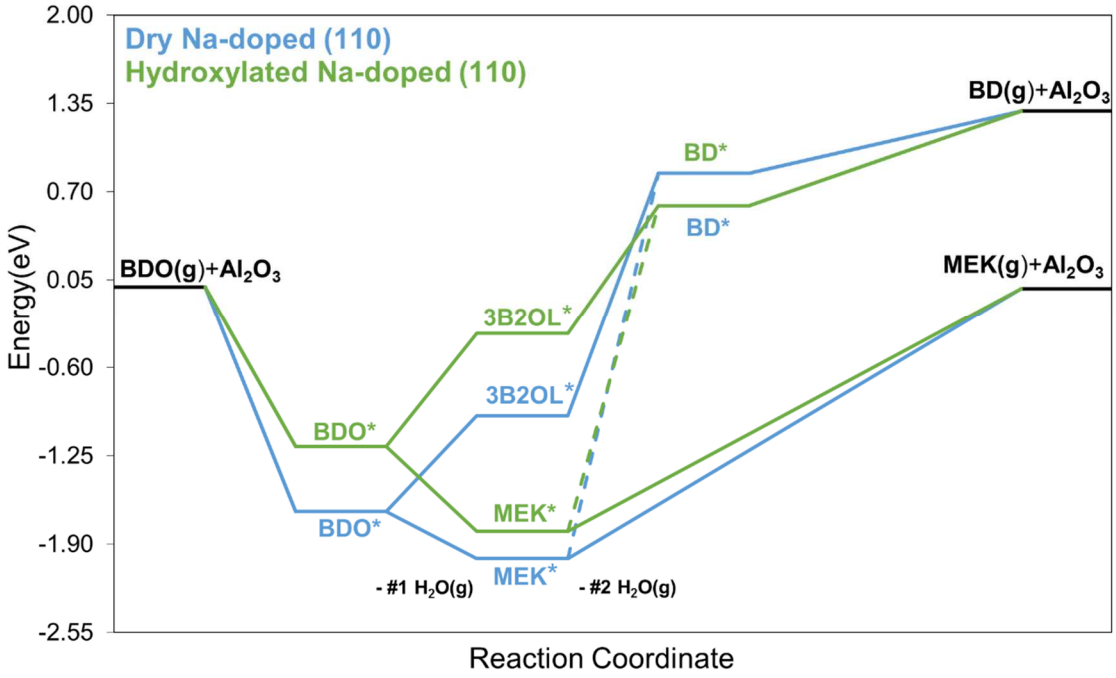

Figure A-4. Potential energies of the two-step BDO dehydration forming 3B2OL, MEK, and BD on dry and hydroxylated Na-modified γ-Al_2O_3 (110) surfaces. The asterisks represent surface species.

`

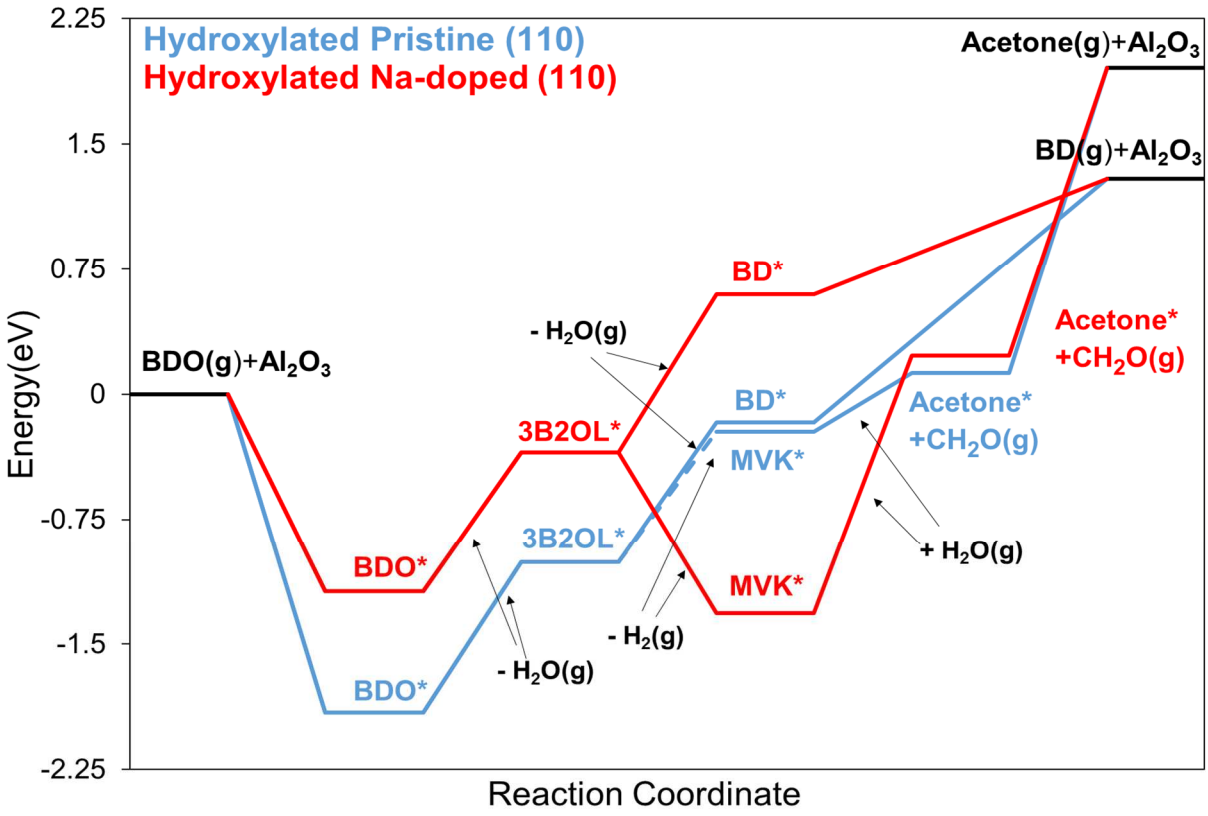

Figure A-5. Potential energies of proposed reaction pathways responsible for acetone formation on hydroxylated pristine and Na-modified γ-Al_2O_3 (110) surfaces.